

Isogeometric continuity constraints for multi-patch shells governed by fourth-order deformation and phase field models

Karsten Paul*, Christopher Zimmermann*, Thang X. Duong*, Roger A. Sauer*^{†1}

*Aachen Institute for Advanced Study in Computational Engineering Science (AICES),
RWTH Aachen University, Templergraben 55, 52062 Aachen, Germany

[†]Department of Mechanical Engineering, Indian Institute of Technology Kanpur, UP 208016, India

Published² in *Comput. Methods Appl. Mech. Eng.*, DOI: [10.1016/j.cma.2020.113219](https://doi.org/10.1016/j.cma.2020.113219)
Submitted on 5. March 2020, Revised on 10. June 2020, Accepted on 14. June 2020

Abstract

This work presents numerical techniques to enforce continuity constraints on multi-patch surfaces for three distinct problem classes. The first involves structural analysis of thin shells that are described by general Kirchhoff-Love kinematics. Their governing equation is a vector-valued, fourth-order, nonlinear, partial differential equation (PDE) that requires at least C^1 -continuity within a displacement-based finite element formulation. The second class are surface phase separations modeled by a phase field. Their governing equation is the Cahn-Hilliard equation – a scalar, fourth-order, nonlinear PDE – that can be coupled to the thin shell PDE. The third class are brittle fracture processes modeled by a phase field approach. In this work, these are described by a scalar, fourth-order, nonlinear PDE that is similar to the Cahn-Hilliard equation and is also coupled to the thin shell PDE. Using a direct finite element discretization, the two phase field equations also require at least a C^1 -continuous formulation. Isogeometric surface discretizations – often composed of multiple patches – thus require constraints that enforce the C^1 -continuity of displacement and phase field. For this, two numerical strategies are presented: A Lagrange multiplier formulation and a penalty method. The curvilinear shell model including the geometrical constraints is taken from [Duong et al. \(2017\)](#) and it is extended to model the coupled phase field problems on thin shells of [Zimmermann et al. \(2019\)](#) and [Paul et al. \(2020\)](#) on multi-patches. Their accuracy and convergence are illustrated by several numerical examples considering deforming shells, phase separations on evolving surfaces, and dynamic brittle fracture of thin shells.

Keywords: Isogeometric analysis, multi-patch discretization, Kirchhoff-Love shells, phase field methods, Cahn-Hilliard equation, brittle fracture

1 Introduction

Thin-walled structures commonly appear in engineering design since they combine the advantages of low weight and high strength. Kirchhoff-Love (KL) theory is a suitable choice to model these, especially if the slenderness ratio is high. This theory contains higher order derivatives, so that the geometric discretization requires higher continuity than standard finite elements. Likewise, diffusion problems are also often described with higher order operators, which necessitates

¹corresponding author, email: sauer@aices.rwth-aachen.de

²This pdf is the personal version of an article whose final publication is available at www.sciencedirect.com.

a higher continuous approximation space for the test and trial functions. The same is true for higher-order fracture models. Isogeometric analysis (IGA) offers the possibility of high smoothness in the geometry and solution. IGA works simplest on a single patch of elements that is discretized with Non-Uniform Rational B-Splines (NURBS). But in real-world problems, single patches are often not sufficient to represent arbitrarily complex shapes or topologies. Instead, multi-patch descriptions are used to discretize these geometries, but the higher continuity is not automatically preserved across the patch interfaces. This work presents a general framework to model coupled problems, in which diffusion and fracture processes take place on deforming thin shells, using multi-patch NURBS discretizations and corresponding patch constraints. The latter enforce the continuity of the surface normal and phase field gradient in order to accurately transfer stresses, moments, mass fluxes and damage gradients at patch interfaces.

In IGA, introduced by [Hughes et al. \(2005\)](#), splines are used to describe the geometry and the solution. This offers the possibility of discretizations with high continuity. Several models have been proposed to describe isogeometric KL shells, starting with [Kiendl et al. \(2009\)](#). KL shell theory only uses displacement degrees-of-freedom (dofs), which distinguishes it from thick shell theories, such as the Reissner-Mindlin shell theory. The pure displacement formulation results in a partial differential equation (PDE) that contains fourth-order derivatives. The required C^1 -continuity in a Galerkin-type finite element formulation is then obtained by means of isogeometric shape functions.

The current work studies two coupled models on deforming thin shells. These models represent two different physical processes but their resulting finite element formulation exhibits many similarities.

The first model is a phase field formulation for phase separations based on the Cahn-Hilliard theory ([Cahn and Hilliard, 1958](#); [Cahn, 1961](#)). The theory of coupling in-plane phase transitions and surface deformations is taken from [Sahu et al. \(2017\)](#). Phase separation in shells occurs in a wide range of applications, including chemical, biological, thermo- and electro-mechanical problems. For instance, lipid membranes may separate into two immiscible phases, often linked to the formation of rafts. The latter are assumed to play a crucial role in the regulation of protein activity, which might affect biological processes such as signaling and trafficking, see [Elson et al. \(2010\)](#) for a review on theoretical and experimental models. Phase transformations in electro-mechanical devices and the resulting change of kinematics and mechanical behavior are for instance investigated by [Tang et al. \(2010\)](#) and [Ebner et al. \(2013\)](#).

The second model investigates brittle fracture based on an adaptive phase field framework. Here, the stored elastic energy can be seen as a driving force for crack evolution³ and material parameters are degraded in regions of fracture. As for the Cahn-Hilliard theory, this model resembles a diffuse interface model in which the transition zone between different phases is smeared out. The foundation for brittle fracture has been established by [Griffith \(1921\)](#), reformulated by [Francfort and Marigo \(1998\)](#) and first implemented within a finite element method by [Bourdin et al. \(2000\)](#). The structural shell formulation for both models is taken from the work of [Duong et al. \(2017\)](#) and the individual coupling is described in detail in [Zimmermann et al. \(2019\)](#) and [Paul et al. \(2020\)](#). Both models lead to a coupled formulation of two nonlinear fourth-order PDEs that are defined on an evolving two-dimensional manifold. Those generally require continuity constraints for multi-patch discretizations. In [Table 1](#), existing techniques for patch coupling in isogeometric analysis are listed together with their main properties and references.⁴

³Note that this viewpoint is questionable, see [Gerasimov and Lorenzis \(2019\)](#).

⁴It is noted that the choice of categories reflects the author's interpretation, which is not unique. Categories can in principle be further subdivided, added or merged.

Table 1: Existing techniques for patch coupling in isogeometric analysis.

Technique	Properties	References
Penalty method	<ul style="list-style-type: none"> + No additional dofs + Easy implementation + Non-conforming meshes – Possible ill-conditioning – Constraint violated – Needs user-specified parameter 	Apostolatos et al. (2014, 2019), Lei et al. (2015), Duong et al. (2017), Horger et al. (2019), Herrema et al. (2019), Leidinger et al. (2019), Bauer et al. (2020)
Bending strip method	<ul style="list-style-type: none"> + Easy implementation – Possible ill-conditioning – Only conforming meshes 	Kiendl et al. (2010), Goyal and Simeon (2017)
Lagrange multiplier method	<ul style="list-style-type: none"> + Non-conforming meshes + No user-specified parameter – Additional dofs – Need to ensure LBB-stability 	Dornisch and Klinkel (2011), Apostolatos et al. (2014, 2019), Bouclier et al. (2016), Duong et al. (2017), Sommerwerk et al. (2017), Mi and Zheng (2018)
Primal mortar method	<ul style="list-style-type: none"> + Non-conforming meshes + Increased robustness due to averaging – Additional dofs – Need to ensure LBB-stability 	Hesch and Betsch (2012), Brivadis et al. (2015), Bouclier et al. (2017), Dittmann et al. (2019, 2020), Hirschler et al. (2019a,b), Horger et al. (2019), Schuß et al. (2019)
Dual mortar method	<ul style="list-style-type: none"> + Non-conforming meshes + Increased robustness due to averaging + No additional dofs – Need to ensure LBB-stability 	Dornisch et al. (2015, 2017), Zou et al. (2018), Wunderlich et al. (2019)
Nitsche’s method	<ul style="list-style-type: none"> + Non-conforming meshes + Variational consistency + Stiffness matrix well conditioned and semi-positive-definite + No additional dofs – Formulation for general problems difficult 	Nguyen et al. (2014), Apostolatos et al. (2014, 2019), Ruess et al. (2014), Du et al. (2015), Guo and Ruess (2015), Bouclier et al. (2017), Nguyen-Thanh et al. (2017), Zhao et al. (2017), Bouclier and Passieux (2018), Gu et al. (2018), Hu et al. (2018), Du et al. (2019), Liu et al. (2019), Yin et al. (2019)
Direct elimination	<ul style="list-style-type: none"> + Fewer dofs – Large implementation effort 	Lei et al. (2015), Coox et al. (2017a,b), Duong et al. (2017)
Continuous multi-patch discretization	<ul style="list-style-type: none"> + Optimal approximation properties – Construction difficult 	Kapl et al. (2015, 2017), Collin et al. (2016), Bracco et al. (2019), Kapl and Vitrih (2020)

Penalty and Lagrange multiplier methods can be derived as special cases of mortar methods. But since they can also be (and have been in the past) derived without introducing the averaging notion of mortar methods, they are listed separately. The dual mortar method constitutes a particularly attractive version that allows to eliminate the unknown Lagrange multipliers through the use of so-called dual mortar shape functions, see also Wohlmuth (2000) and Seitz et al. (2016).

There are also references that lie outside the categories of Table 1. Kiendl et al. (2009) construct G^1 -continuous KL shell parametrizations by coupling the first and second rows of control points

at patch interfaces with each other. This method is restricted to conforming meshes and smooth interfaces. [Beirão da Veiga et al. \(2011\)](#) study the approximation properties of T-splines on non-conforming two-patch geometries. The patches are coupled by inserting knots at the interface and overlapping the underlying T-meshes.

Cahn-Hilliard phase transitions on fixed multi-patch domains have recently been investigated by [Chan et al. \(2018\)](#) and [Dittmann et al. \(2020\)](#). In the present work, this is exceeded by considering deforming multi-patch domains. [Chan et al. \(2018\)](#) also propose a method to overcome C^1 -locking by local degree elevation along patch interfaces. C^1 -locking refers to restricted convergence rates due to overconstraining of the solution space ([Collin et al., 2016](#)). Their work is further advanced to a more efficient two- and three-dimensional coupling of multi-patch domains for general geometries by [Chan et al. \(2019\)](#).

The present work extends the general geometrical constraint formulation of [Duong et al. \(2017\)](#) to coupled problems describing Cahn-Hilliard-type phase transitions on deforming thin shells ([Zimmermann et al., 2019](#)), and phase field based fracture of brittle shells ([Paul et al., 2020](#)). Patch constraints that enforce the required C^1 -continuity of the phase field across patch interfaces are proposed, and their accuracy and convergence behavior are studied. Summarizing, the proposed formulation includes following highlights:

- It proposes a new constraint for C^1 -continuous phase fields on multi-patch NURBS.
- It is fully formulated in a curvilinear coordinate system.
- It uses these constraints to model coupled problems on multi-patch NURBS.
- It exhibits excellent accuracy compared to single patch discretizations.
- It is capable to describe fracture branching across kinked surfaces within a higher-order phase field model.
- The proposed constraints are validated by several nonlinear benchmark problems.

The remainder of this paper is structured as follows: [Sec. 2](#) summarizes the employed thin shell framework. The computational formulation for the Cahn-Hilliard phase separation model is summarized in [Sec. 3](#). In [Sec. 4](#), the computational phase field model of brittle shells is outlined. The proposed formulation for the required patch constraints is discussed in [Sec. 5](#). Numerical examples that highlight the effect of these constraints on the numerical solution are shown in [Sec. 6](#). This paper concludes with a summary and an outlook in [Sec. 7](#).

2 Thin shell theory

This paper is concerned with thin shell theory and its coupling to two phase field models, see [Fig. 1](#). This section summarizes the computational description of thin shells, while binary mixtures and fracture follow in [Secs. 3–4](#). At first, a short introduction to the surface description is given, which is then followed by the discretized weak form and constitutive relations. Further mathematical background and details of thin shell theory can be found for example in [Sauer \(2018\)](#).

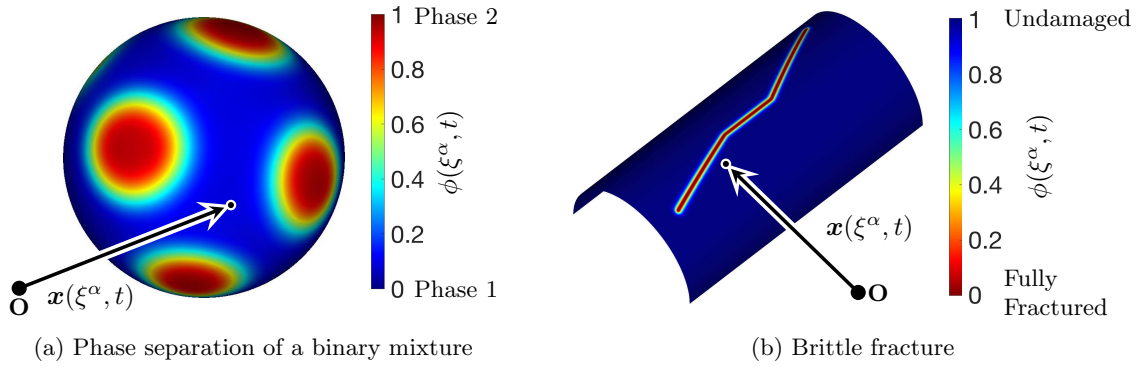


Figure 1: Two cases of phase fields on curved shells. (a) Phase separation of a binary mixture, where ϕ describes the mixture of two phases, and (b) fracture, where ϕ distinguishes between undamaged and fully fractured material.

2.1 Surface description

Following the framework of differential geometry, a curved surface \mathcal{S} is described by a convected coordinate system and the mapping

$$\mathbf{x} = \mathbf{x}(\xi^\alpha, t), \quad (1)$$

between the parameter domain and the physical surface. Here, ξ^α , $\alpha = 1, 2$, denote the convective coordinates and t denotes time.⁵ The phase field is denoted $\phi(\xi^\alpha, t)$ and ranges from 0 to 1, see Fig. 1. The mapping in Eq. (1) then defines a set of surface points $\mathbf{x} \in \mathcal{S}$ to represent the surface. A co-variant basis $\{\mathbf{a}_\alpha, \mathbf{n}\}$ is associated with each of these surface points with co-variant tangent vectors \mathbf{a}_α and surface normal \mathbf{n} defined by

$$\mathbf{a}_\alpha := \frac{\partial \mathbf{x}}{\partial \xi^\alpha}, \quad \text{and} \quad \mathbf{n} := \frac{\mathbf{a}_1 \times \mathbf{a}_2}{\|\mathbf{a}_1 \times \mathbf{a}_2\|}. \quad (2)$$

The co-variant surface metric with components

$$a_{\alpha\beta} := \mathbf{a}_\alpha \cdot \mathbf{a}_\beta \quad (3)$$

then follows. Orthonormality in the basis is achieved by the introduction of a contra-variant basis $\{\mathbf{a}^\alpha, \mathbf{n}\}$, such that $\mathbf{a}_\alpha \cdot \mathbf{a}^\beta = \delta_\alpha^\beta$, with Kronecker delta δ_α^β . The contra-variant tangent vectors are given by

$$\mathbf{a}^\alpha = a^{\alpha\beta} \mathbf{a}_\beta, \quad (4)$$

where the contra-variant surface metric $a^{\alpha\beta}$ follows from the inverse of the co-variant surface metric, i.e. $[a^{\alpha\beta}] = [a_{\alpha\beta}]^{-1}$. The second parametric derivative $\mathbf{a}_{\alpha,\beta} := \partial \mathbf{a}_\alpha / \partial \xi^\beta$ is introduced in order to determine the curvature components and the mean curvature, i.e.

$$b_{\alpha\beta} := \mathbf{a}_{\alpha,\beta} \cdot \mathbf{n}, \quad \text{and} \quad H := a^{\alpha\beta} b_{\alpha\beta} / 2. \quad (5)$$

Based on this geometric representation of surface \mathcal{S} , surface operators can be defined, namely the surface gradient and surface Laplacian of a general scalar ϕ , and the surface divergence of a general vector \mathbf{v} ,

$$\begin{aligned} \text{grad}_s \phi &:= \nabla_s \phi &:= \phi_{;\alpha} \mathbf{a}^\alpha, \\ \text{div}_s \mathbf{v} &:= \nabla_s \cdot \mathbf{v} &:= \mathbf{v}_{;\alpha} \cdot \mathbf{a}^\alpha, \\ \Delta_s \phi &:= \nabla_s \cdot \nabla_s \phi &= \phi_{;\alpha\beta} a^{\alpha\beta}. \end{aligned} \quad (6)$$

⁵All Greek indices run from 1 to 2 and obey Einstein's summation convention.

The subscript ‘;’ is used to denote the co-variant derivative defined by

$$\begin{aligned}\phi_{;\alpha} &= \phi_{,\alpha}, \\ \mathbf{v}_{;\alpha} &= \mathbf{v}_{,\alpha}, \\ \phi_{;\alpha\beta} &= \phi_{,\alpha\beta} - \Gamma_{\alpha\beta}^{\gamma} \phi_{,\gamma},\end{aligned}\tag{7}$$

with $\dots_{,\alpha} := \partial\dots/\partial\xi^{\alpha}$ and the Christoffel symbols of the second kind $\Gamma_{\alpha\beta}^{\gamma} := \mathbf{a}_{\alpha,\beta} \cdot \mathbf{a}^{\gamma}$ on \mathcal{S} .

2.2 Discretization of primary fields

Subsequently, the finite element (FE) approximations of the primary fields, the deformation and phase field, are outlined. The n_e spline basis functions on element Ω^e are numbered with global indices i_1, \dots, i_{n_e} . The FE approximations of \mathbf{x} and its variation $\delta\mathbf{x}$ on element Ω^e can then be written as

$$\mathbf{x} \approx \mathbf{N} \mathbf{x}_e, \quad \text{and} \quad \delta\mathbf{x} \approx \mathbf{N} \delta\mathbf{x}_e,\tag{8}$$

with \mathbf{x}_e and $\delta\mathbf{x}_e$ describing the element-level vectors of nodal values and their variation, respectively. Further, the shape function array in Eq. (8) is given by

$$\mathbf{N} = [N_{i_1} \mathbf{1}, N_{i_2} \mathbf{1}, \dots, N_{i_{n_e}} \mathbf{1}],\tag{9}$$

with $\mathbf{1}$ denoting the (3×3) -identity matrix. The FE approximations of the phase field ϕ and its variation $\delta\phi$ on element Ω^e follow in analogy, i.e.

$$\phi \approx \bar{\mathbf{N}} \phi_e, \quad \text{and} \quad \delta\phi \approx \bar{\mathbf{N}} \delta\phi_e,\tag{10}$$

with shape function array

$$\bar{\mathbf{N}} := [N_{i_1}, N_{i_2}, \dots, N_{i_{n_e}}],\tag{11}$$

and with the element-level vector of the nodal phase values and its variation ϕ_e and $\delta\phi_e$.

2.3 Discretized mechanical weak form

The discretized mechanical weak form can be written as (Duong et al., 2017)

$$\delta\mathbf{x}^T [\mathbf{f}_{\text{in}} + \mathbf{f}_{\text{int}} - \mathbf{f}_{\text{ext}}] = 0, \quad \forall \delta\mathbf{x} \in \mathcal{U}^h,\tag{12}$$

where the global force vectors \mathbf{f}_{in} , \mathbf{f}_{int} and \mathbf{f}_{ext} are assembled from their respective element-level contributions

$$\begin{aligned}\mathbf{f}_{\text{in}}^e &:= \mathbf{m}_e \ddot{\mathbf{x}}_e, \quad \mathbf{m}_e := \int_{\Omega^e} \rho(\phi) \mathbf{N}^T \mathbf{N} \, da, \\ \mathbf{f}_{\text{int}}^e &:= \int_{\Omega^e} \sigma^{\alpha\beta}(\phi) \mathbf{N}_{;\alpha}^T \mathbf{a}_{\beta} \, da + \int_{\Omega^e} M^{\alpha\beta}(\phi) \mathbf{N}_{;\alpha\beta}^T \mathbf{n} \, da, \\ \mathbf{f}_{\text{ext}}^e &:= \int_{\Omega^e} \mathbf{N}^T p(\phi) \mathbf{n} \, da + \int_{\Omega^e} \mathbf{N}^T f^{\alpha}(\phi) \mathbf{a}_{\alpha} \, da,\end{aligned}\tag{13}$$

with shape function array \mathbf{N} from Eq. (9). Here, \mathcal{U}^h denotes the corresponding discrete space, and $\mathbf{N}_{;\alpha\beta}^T$ follows in analogy to Eq. (7.3). The density is $\rho(\phi)$, the prescribed body forces are $\mathbf{f}(\phi) = f^{\alpha}(\phi) \mathbf{a}_{\alpha} + p(\phi) \mathbf{n}$, and the stress and moment components are $\sigma^{\alpha\beta}(\phi)$ and $M^{\alpha\beta}(\phi)$, respectively.⁶ Note that boundary loads acting on $\partial\mathcal{S}$ are assumed to be zero in the above

⁶ $\sigma^{\alpha\beta}$ is a 2D stress (measured as force per length) that is also referred to the stress resultant, i.e. the thickness integral of the 3D stress, e.g. see Simo and Fox (1989) and Simo et al. (1990).

expression of $\mathbf{f}_{\text{ext}}^e$. The corresponding extension to boundary loads is described in [Duong et al. \(2017\)](#). From Eq. (12) follows the equation of motion at the free nodes (where no Dirichlet boundary conditions are prescribed)

$$\mathbf{f}(\mathbf{x}, \phi) = \mathbf{M} \ddot{\mathbf{x}} + \mathbf{f}_{\text{int}}(\mathbf{x}, \phi) - \mathbf{f}_{\text{ext}}(\mathbf{x}, \phi) = \mathbf{0}, \quad (14)$$

where \mathbf{x} and ϕ are the global unknowns, similar to the element-level unknowns \mathbf{x}_e and ϕ_e . The global mass matrix \mathbf{M} follows from the assembly of the matrices \mathbf{m}_e . Eq. (14) can be solved by itself in case ϕ is not an unknown, as in the examples of Sec. 6.1.

2.4 Constitutive relations

The constitutive behavior follows from the Helmholtz free energy function

$$\Psi = \Psi_{\text{el}} + \Psi_{\text{phase}}. \quad (15)$$

The second term is discussed in Secs. 3.2 and 4.2. For the first term, a hyperelastic material behavior with an elastic energy density $\Psi_{\text{el}} = \Psi_{\text{el}}(a_{\alpha\beta}, b_{\alpha\beta}, \phi)$ is assumed. It is composed of membrane and bending contributions, i.e. $\Psi_{\text{el}} = \Psi_{\text{dil}} + \Psi_{\text{dev}} + \Psi_{\text{bend}}$. The first is given by a Neo-Hookean membrane model ([Sauer and Duong, 2017](#))

$$\Psi_{\text{dil}} = \frac{K}{4}(J^2 - 1 - 2 \ln J), \quad \text{and} \quad \Psi_{\text{dev}} = \frac{G}{2}(I_1/J - 2), \quad (16)$$

and the second by the Koiter bending model ([Ciarlet, 1993](#))

$$\Psi_{\text{bend}} = \frac{c}{2}(b_{\alpha\beta} - B_{\alpha\beta})(b_0^{\alpha\beta} - B^{\alpha\beta}), \quad \text{with} \quad b_0^{\alpha\beta} := A^{\alpha\gamma} b_{\gamma\delta} A^{\beta\delta}. \quad (17)$$

Note that quantities defined on the reference surface are either indicated by a capital symbol, or the subscript ‘0’, whereas quantities on the current surface are indicated by lowercase symbols. The two invariants in Eq. (16) are

$$I_1 := A^{\alpha\beta} a_{\alpha\beta}, \quad \text{and} \quad J := \sqrt{\det[A^{\alpha\beta}] \det[a_{\alpha\beta}]}, \quad (18)$$

with contra-variant metric $A^{\alpha\beta}$ in the reference configuration. The 2D bulk, 2D shear, and bending moduli are denoted K , G , and c , respectively, and they are generally a function of the phase variable ϕ . The stress and moment components follow from⁶

$$\begin{aligned} \sigma^{\alpha\beta} &= \frac{2}{J} \frac{\partial \Psi}{\partial a_{\alpha\beta}} - \eta \dot{a}^{\alpha\beta}, \\ M^{\alpha\beta} &= \frac{1}{J} \frac{\partial \Psi}{\partial b_{\alpha\beta}}. \end{aligned} \quad (19)$$

Eq. (19.1) represents a Kelvin model to account for viscous in-plane stresses. In this model, a spring and dashpot act in parallel and thus, their stresses are added.⁷ The dynamic surface viscosity is denoted η . More complex constitutive models require a general strain decomposition, which has been recently formulated for Kirchhoff-Love shells in [Sauer et al. \(2019\)](#). For the above material model, the individual contributions to the stress components are given by

$$\begin{aligned} \sigma_{\text{dil}}^{\alpha\beta} &= \frac{K}{2J}(J^2 - 1) a^{\alpha\beta}, \\ \sigma_{\text{dev}}^{\alpha\beta} &= \frac{G}{2J^2}(2A^{\alpha\beta} - I_1 a^{\alpha\beta}), \\ \sigma_{\text{visc}}^{\alpha\beta} &= -\eta \dot{a}^{\alpha\beta}. \end{aligned} \quad (20)$$

⁷In Eq. (19), $\dot{a}^{\alpha\beta} = -a^{\alpha\gamma} \dot{a}_{\gamma\delta} a^{\delta\beta}$ are the components of the symmetric surface velocity gradient, e.g. see [Sauer \(2018\)](#).

Likewise, the moment components stemming from Eq. (17) are

$$M^{\alpha\beta} = \frac{c}{J}(b_0^{\alpha\beta} - B^{\alpha\beta}). \quad (21)$$

Note that Eqs. (20)–(21) do not contain the stresses and moments coming from the phase field model. These are discussed in Secs. 3.2 and 4.2.

3 Phase transitions on deforming surfaces

This section briefly summarizes the discretized weak form and constitutive relations describing phase transitions on deforming surfaces according to the computational model of Zimmermann et al. (2019). The Cahn-Hilliard model is essentially a temperature dependent diffusion model with an additional term that penalizes phase interfaces. For low temperatures, the phases are driven towards separation (considered here), while for high temperatures, they are driven towards mixture. In the following, the dimensionless concentration field $\phi(\xi^\alpha, t)$ is used to describe the local density fractions of binary mixtures, see Fig. 1a.⁸

3.1 Discretized weak form

The discretized weak form of the surface Cahn-Hilliard equation can be written as

$$\delta\phi^T [\bar{\mathbf{f}}_{\text{in}} + \bar{\mathbf{f}}_{\text{int}} - \bar{\mathbf{f}}_{\text{ext}}] = 0, \quad \forall \delta\phi \in \mathcal{V}^h. \quad (22)$$

The global vectors $\bar{\mathbf{f}}_{\text{in}}$, $\bar{\mathbf{f}}_{\text{int}}$ and $\bar{\mathbf{f}}_{\text{ext}}$ are assembled from their respective element-level contributions

$$\begin{aligned} \bar{\mathbf{f}}_{\text{in}}^e &:= \bar{\mathbf{m}}_e \dot{\phi}_e, \quad \bar{\mathbf{m}}_e := \int_{\Omega^e} \rho \bar{\mathbf{N}}^T \bar{\mathbf{N}} \, da, \\ \bar{\mathbf{f}}_{\text{int}}^e &:= \bar{\mathbf{k}}_e \phi_e - \bar{\mathbf{f}}_{\text{el}}^e, \quad \bar{\mathbf{k}}_e := \int_{\Omega_0^e} \left[\bar{\mathbf{N}}_{,\alpha}^T a^{\alpha\beta} \left(M \mu'_\phi - M'(\mu_i + \mu_{\text{el}}) \right) \bar{\mathbf{N}}_{,\beta} + \Delta_s \bar{\mathbf{N}}^T J \ell^2 M \Delta_s \bar{\mathbf{N}} \right] dA, \\ \bar{\mathbf{f}}_{\text{el}}^e &:= \int_{\Omega_0^e} \Delta_s \bar{\mathbf{N}}^T M \mu_{\text{el}} \, dA, \\ \bar{\mathbf{f}}_{\text{ext}}^e &:= \mathbf{0}. \end{aligned} \quad (23)$$

Here, $(\dots)' := \partial \dots / \partial \phi$, while the corresponding discrete space is denoted \mathcal{V}^h , and $\Delta_s \bar{\mathbf{N}}$ follows in analogy to Eq. (6.3). Further, $M = D \phi(1 - \phi)$, $D = \text{const.}$, denotes the degenerate mobility, ℓ represents the length scale of the phase interface and J is the surface stretch, see Eq. (18.2). The remaining terms in Eq. (23) are described in Sec. 3.2. Note that $\bar{\mathbf{f}}_{\text{ext}}^e$ is assumed to be zero in the above expressions. The extension to non-zero $\bar{\mathbf{f}}_{\text{ext}}^e$ is described in Zimmermann et al. (2019). From Eq. (22) follows the evolution equation for ϕ at the free nodes (after application of Dirichlet boundary conditions)

$$\bar{\mathbf{f}}(\mathbf{x}, \phi) = \bar{\mathbf{M}} \dot{\phi} + \bar{\mathbf{f}}_{\text{int}}(\mathbf{x}, \phi) - \bar{\mathbf{f}}_{\text{ext}}(\mathbf{x}) = \mathbf{0}, \quad (24)$$

with global mass matrix $\bar{\mathbf{M}}$ being assembled from $\bar{\mathbf{m}}_e$. Together, Eqs. (14) and (24) describe a coupled chemo-mechanical problem. It is discretized and integrated in time with an implicit, monolithic and adaptive method (Zimmermann et al., 2019) based on the generalized- α scheme by Chung and Hulbert (1993).

⁸The concentration field ϕ is also referred to as the *order parameter field* or *phase field* in the literature.

3.2 Constitutive relations

The material parameters are assumed to depend on the concentration field ϕ via the following mixture rules

$$\begin{aligned} K(\phi) &= K_1 f(\phi) + K_0 (1 - f(\phi)), & G(\phi) &= G_1 f(\phi) + G_0 (1 - f(\phi)), \\ c(\phi) &= c_1 f(\phi) + c_0 (1 - f(\phi)), & \eta(\phi) &= \eta_1 f(\phi) + \eta_0 (1 - f(\phi)), \end{aligned} \quad (25)$$

with the interpolation function

$$f(\phi) = \frac{1}{2} \left(1 + \tanh(-\rho_{\text{sh}} \pi + 4 \pi \phi) \right). \quad (26)$$

Here, K_i , G_i , c_i and η_i ($i = 0, 1$) are the material parameters of the two components. The parameter $\rho_{\text{sh}} \in \mathbb{R}$ specifies whether a small or a large portion of the phase interface is characterized by material properties at $\phi = 1$. The force vectors in Eq. (23) include the chemical potential μ that has the contributions μ_{b} , μ_{i} , μ_{el} , μ_{ϕ} associated with the bulk, interface, elastic, and mixing energy, given by

$$\begin{aligned} \mu_{\text{b}} &= \mu_{\phi} + \mu_{\text{el}}, & \mu_{\phi} &= N k_{\text{B}} T \ln \frac{\phi}{1 - \phi} + N \omega (1 - 2\phi), \\ \mu_{\text{el}} &= \Psi'_{\text{el}}, & \mu_{\text{i}} &= -J N \omega \ell^2 \Delta_{\text{s}} \phi. \end{aligned} \quad (27)$$

Here, N denotes the number of molecules per reference area, k_{B} is Boltzmann's constant and $\omega = 2 k_{\text{B}} T_{\text{c}}$ is a bulk energy that is related to the critical temperature T_{c} at which phase separation occurs.

The Cahn-Hilliard energy in Eq. (15) is given by

$$\Psi_{\text{phase}} = N \omega \phi (1 - \phi) + T N k_{\text{B}} (\phi \ln \phi + (1 - \phi) \ln(1 - \phi)) + J N \omega \frac{\ell^2}{2} \nabla_{\text{s}} \phi \cdot \nabla_{\text{s}} \phi. \quad (28)$$

The stresses stemming from Ψ_{phase} are known as Korteweg stresses and they are given by

$$\sigma_{\text{CH}}^{\alpha\beta} = N \omega \frac{\ell^2}{2} \left(a^{\alpha\beta} a^{\gamma\delta} - 2 a^{\alpha\gamma} a^{\beta\delta} \right) \phi_{;\gamma} \phi_{;\delta}. \quad (29)$$

Note that there are no bending moments induced by the Cahn-Hilliard energy.

4 Brittle fracture of deforming thin shells

This section summarizes the phase field model for brittle fracture of thin shells by Paul et al. (2020). In phase field methods, cracks are smeared out and described by a field $\phi(\xi^{\alpha}, t) \in [0, 1]$, see Fig. 1b.⁹ It indicates fully fractured ($\phi = 0$) and undamaged ($\phi = 1$) material. A length scale parameter ℓ_0 [m] gives control over the support width of the phase field profile, i.e. $\text{supp}(\phi) \sim \ell_0$.

4.1 Discretized weak form

The phase field evolution equation is determined from the minimization of the Helmholtz free energy that consists of elastic and fracture contributions, see Sec. 4.2. Based on this, the discretized weak form of the phase field evolution equation becomes

$$\delta \phi^{\text{T}} [\bar{\mathbf{f}}_{\text{el}} + \bar{\mathbf{f}}_{\text{frac}}] = 0, \quad \forall \delta \phi \in \mathcal{V}^h, \quad (30)$$

⁹The phase field ϕ is also referred to as the *fracture field* in the literature.

with the corresponding finite-dimensional space \mathcal{V}^h and the element-level contributions

$$\begin{aligned}\bar{\mathbf{f}}_{\text{el}}^e &:= \int_{\Omega_0^e} \bar{\mathbf{N}}^T \frac{2\ell_0}{\mathcal{G}_c} g'(\phi) \mathcal{H} \, dA, \\ \bar{\mathbf{f}}_{\text{frac}}^e &:= \int_{\Omega_0^e} \left[\bar{\mathbf{N}}^T \bar{\mathbf{N}} + \bar{\mathbf{N}}_{,\alpha}^T 2\ell_0^2 A^{\alpha\beta} \bar{\mathbf{N}}_{,\beta} + \Delta_S \bar{\mathbf{N}}^T \ell_0^4 \Delta_S \bar{\mathbf{N}} \right] \phi_e \, dA - \int_{\Omega_0^e} \bar{\mathbf{N}}^T \, dA.\end{aligned}\quad (31)$$

The shape function array for the phase field is denoted $\bar{\mathbf{N}}$, see Eq. (11), and $\Delta_S \bar{\mathbf{N}}$ follows in analogy to Eq. (6.3). Note that here, the surface Laplacian is defined on the reference configuration. \mathcal{G}_c denotes the fracture toughness. The degradation function (Borden et al., 2016)

$$g(\phi) = (3-s)\phi^2 - (2-s)\phi^3, \quad s = 10^{-4}, \quad (32)$$

controls the loss of material stiffness in regions of fracture and \mathcal{H} is the history field that is motivated and discussed in the next section. The degradation function in Eq. (32) couples the elastic energy density in Eq. (15) with the phase field, see Eq. (35). The phase field force vector is coupled to the deformation by the history field \mathcal{H} , see Eq. (31.1). The resulting equations at the free nodes (where no Dirichlet boundary conditions are imposed) simplify to

$$\bar{\mathbf{f}}(\mathbf{x}, \phi) = \bar{\mathbf{f}}_{\text{el}}(\mathbf{x}, \phi) + \bar{\mathbf{f}}_{\text{frac}}(\phi) = \mathbf{0}. \quad (33)$$

To obtain a highly resolved mesh in regions of damage, a local refinement strategy based on LR NURBS is employed (Paul et al., 2020). As for the phase separation process, the temporal discretization is based on the generalized- α scheme by Chung and Hulbert (1993) using adaptive time-stepping.

4.2 Constitutive relations

Crack evolution exhibits anisotropic behavior since it does not occur in compression. Thus, an additive split of the elastic energy density is required,

$$\Psi_{\text{el}} = \Psi_{\text{el}}^+ + \Psi_{\text{el}}^-, \quad (34)$$

that distinguishes between a positive part that contributes to crack evolution, and a negative part, which does not. The elastic part of the Helmholtz free energy in Eq. (15) is thus, changed to

$$\Psi_{\text{el}} = g(\phi) \mathcal{H} + \Psi_{\text{el}}^-, \quad (35)$$

with the history field $\mathcal{H}(\mathbf{x}, t) = \max_{\tau \in [0, t]} \Psi_{\text{el}}^+(\mathbf{x}, \tau)$ that enforces an irreversible fracture process and the degradation function $g(\phi)$ from Eq. (32). The fracture energy is given by (Borden et al., 2014; Paul et al., 2020)

$$\Psi_{\text{phase}} = \frac{\mathcal{G}_c}{4\ell_0} \left[(\phi - 1)^2 + 2\ell_0^2 \nabla_S \phi \cdot \nabla_S \phi + \ell_0^4 (\Delta_S \phi)^2 \right]. \quad (36)$$

The membrane and bending contributions of Ψ_{el} are split separately and the split of Amor et al. (2009) is adopted for the membrane part, i.e.

$$\Psi_{\text{mem}}^+ = \begin{cases} \Psi_{\text{dev}} + \Psi_{\text{dil}}, & J \geq 1 \\ \Psi_{\text{dev}}, & J < 1 \end{cases}, \quad \text{and} \quad \Psi_{\text{mem}}^- = \begin{cases} 0, & J \geq 1 \\ \Psi_{\text{dil}}, & J < 1 \end{cases}, \quad (37)$$

with dilatational and deviatoric energies taken from Eq. (16) and surface stretch J from Eq. (18.2). Now, the total stresses in the system are given by

$$\sigma^{\alpha\beta} = g(\phi) \sigma_+^{\alpha\beta} + \sigma_-^{\alpha\beta}, \quad (38)$$

with

$$\sigma_+^{\alpha\beta} = \begin{cases} \sigma_{\text{dev}}^{\alpha\beta} + \sigma_{\text{dil}}^{\alpha\beta}, & J \geq 1 \\ \sigma_{\text{dev}}^{\alpha\beta}, & J < 1 \end{cases}, \quad \text{and} \quad \sigma_-^{\alpha\beta} = \begin{cases} 0, & J \geq 1 \\ \sigma_{\text{dil}}^{\alpha\beta}, & J < 1 \end{cases}, \quad (39)$$

and contributions from Eqs. (20.1)–(20.2). The degradation function $g(\phi)$ is given in Eq. (32). The brittle fracture model does not presently include viscosity, such that $\eta = 0$, see Eq. (19.1).

The bending part of the elastic energy density Ψ_{bend} is split based on thickness integration (Paul et al., 2020). It is constructed from the three-dimensional Saint Venant-Kirchhoff model (Duong et al., 2017)

$$\tilde{\Psi}_{\text{bend}}(\mathbf{K}, \xi, T) = \xi^2 \frac{12}{T^3} \frac{c}{2} \text{tr}(\mathbf{K}^2), \quad (40)$$

with the relative curvature tensor $\mathbf{K} = (b_{\alpha\beta} - B_{\alpha\beta}) \mathbf{A}^\alpha \otimes \mathbf{A}^\beta$. The energy split is then performed on this three-dimensional constitutive law. Afterwards, it is integrated over the thickness to obtain the energy split in surface energy form, i.e.

$$\Psi_{\text{bend}}^\pm = \int_{-\frac{T}{2}}^{\frac{T}{2}} \tilde{\Psi}_{\text{bend}}^\pm(\xi) \, d\xi. \quad (41)$$

In analogy to Eq. (37), the split of Eq. (40) is based on the surface stretch \tilde{J} of the shell layer at position $\xi \in [-T/2, T/2]$, i.e.

$$\tilde{\Psi}_{\text{bend}}^+(\xi) = \begin{cases} \xi^2 \frac{12}{T^3} \frac{c}{2} \text{tr}(\mathbf{K}^2), & \tilde{J}(\xi) \geq 1 \\ 0, & \tilde{J}(\xi) < 1 \end{cases}, \quad \text{and} \quad \tilde{\Psi}_{\text{bend}}^-(\xi) = \begin{cases} 0, & \tilde{J}(\xi) \geq 1 \\ \xi^2 \frac{12}{T^3} \frac{c}{2} \text{tr}(\mathbf{K}^2), & \tilde{J}(\xi) < 1 \end{cases}. \quad (42)$$

In analogy to Eq. (18.2), the surface stretch \tilde{J} is computed from

$$\tilde{J} = \sqrt{\det[G^{\alpha\beta}] \det[g_{\alpha\beta}]}, \quad (43)$$

where the metrics $G^{\alpha\beta}$ and $g_{\alpha\beta}$ follow from the tangent vectors \mathbf{G}_α and \mathbf{g}_α of the shell layer at points $\mathbf{X} + \xi \mathbf{N}$ and $\mathbf{x} + \xi \mathbf{n}$, respectively (Duong et al., 2017). The resulting moment is given by

$$M^{\alpha\beta} = g(\phi) M_+^{\alpha\beta} + M_-^{\alpha\beta}, \quad (44)$$

with degradation function $g(\phi)$ from Eq. (32) and the contributions

$$M_\pm^{\alpha\beta} = \int_{-\frac{T}{2}}^{\frac{T}{2}} \tilde{M}_\pm^{\alpha\beta}(\xi) \, d\xi. \quad (45)$$

Here, $\tilde{M}_\pm^{\alpha\beta}$ refers to the split of the moment components stemming from the three-dimensional constitutive law. The split is given by

$$\tilde{M}_+^{\alpha\beta} = \begin{cases} \tilde{M}^{\alpha\beta}, & \tilde{J}(\xi) \geq 1 \\ 0, & \tilde{J}(\xi) < 1 \end{cases}, \quad \text{and} \quad \tilde{M}_-^{\alpha\beta} = \begin{cases} 0, & \tilde{J}(\xi) \geq 1 \\ \tilde{M}^{\alpha\beta}, & \tilde{J}(\xi) < 1 \end{cases}, \quad (46)$$

with

$$\tilde{M}^{\alpha\beta} = \xi^2 \frac{12}{T^3} \frac{c}{J} (b_0^{\alpha\beta} - B^{\alpha\beta}), \quad \text{and} \quad b_0^{\alpha\beta} = A^{\alpha\gamma} b_{\gamma\delta} A^{\beta\delta}. \quad (47)$$

5 Continuity constraints for patch interfaces

The force vectors of the discretized weak forms in Eqs. (13), (23) and (31) include second-order operators. This necessitates an at least C^1 -continuous discretization¹⁰. Here, this is obtained by using an isogeometric surface discretization. In general, especially for complex engineering structures, it is not possible to represent the geometry with a single NURBS patch. Instead, multiple patches are required. At the interfaces between these patches, the C^1 -continuity is lost and needs to be recovered. For the mechanical shell equations in the weak form from Eqs. (12)–(13), it is sufficient to impose a geometric G^1 -continuity constraint to transfer bending moments across the patch interfaces. Duong et al. (2017) introduce two methods to enforce this constraint for five different edge rotation conditions: enforcing G^1 -continuity, maintaining surface folds, enforcing symmetry conditions on flat sheets, enforcing symmetry conditions on folded sheets and prescribing boundary rotations. Their formulation is summarized and simplified in Sec. 5.1. For the surface concentration and the fracture field, a new C^1 -continuity constraint is proposed in Sec. 5.2. It is used to obtain continuous surface gradients $\nabla_s \phi$ and $\nabla_S \phi$ across patch interfaces. In the present work, conforming meshes are considered and thus, the G^0 - and C^0 -continuity of \boldsymbol{x} and ϕ are automatically satisfied at the patch interfaces.

Here, the four different types of element-level patch interfaces depicted in Fig. 2 are considered. From left to right, the number of elements from different patches that meet at a point on the surface increases from two to five. The following theory is also valid for other cases, but the examples in Sec. 6 are restricted to the cases depicted in Fig. 2. In the present formulation, a potential that enforces the constraints is added to the total potential of the system, see the subsequent sections. Thus, numerical integration along the patch interfaces is required. In this section, these interfaces are shown by red lines in the figures. The elements meeting at these interfaces are denoted Ω^e , $e = 1, \dots, n_{\text{patch}}$, where n_{patch} denotes the number of patches.

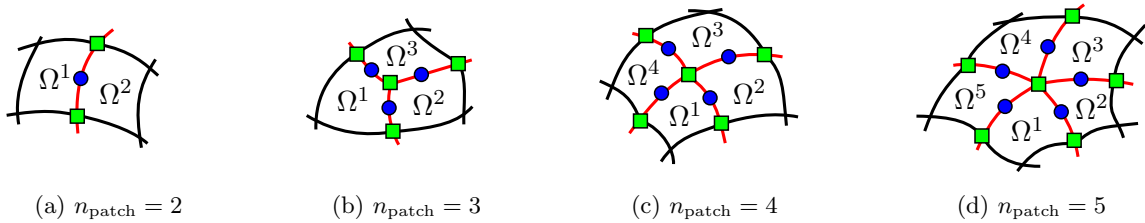


Figure 2: Illustration of different element-level patch constellations. From left to right, the number of patch elements that share at least one common control point increases from two to five. The red lines mark the patch interfaces and the elements are denoted Ω^e , $e = 1, \dots, n_{\text{patch}}$. The circular blue and square green symbols mark the position of constant and linear Lagrange multipliers, respectively, along the patch interfaces.

The patch interfaces Γ are discretized into line elements denoted Γ^e that conform to surface elements. Fig. 3 illustrates the local coordinate systems for a given element-level patch interface Γ^e that is parameterized by the coordinate s . Note that the boundary quantities on two adjacent patches are distinguished by a tilde. Both the interface tangent and normal vector are orthogonal to the surface normal. They follow from

$$\boldsymbol{\tau} = \frac{\partial \boldsymbol{x}}{\partial s}, \quad \boldsymbol{\nu} = \boldsymbol{\tau} \times \boldsymbol{n}, \quad \tilde{\boldsymbol{\tau}} = \frac{\partial \tilde{\boldsymbol{x}}}{\partial \tilde{s}}, \quad \tilde{\boldsymbol{\nu}} = \tilde{\boldsymbol{\tau}} \times \tilde{\boldsymbol{n}}, \quad (48)$$

¹⁰Unless other methods, like mixed (e.g. displacement and rotation) methods, are used.

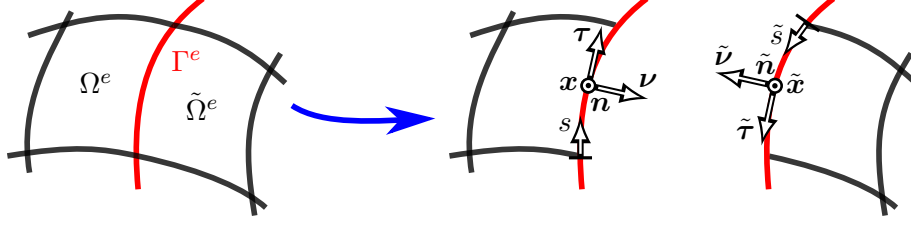


Figure 3: Local coordinate systems $\{\boldsymbol{\nu}, \boldsymbol{\tau}, \boldsymbol{n}\}$ and $\{\tilde{\boldsymbol{\nu}}, \tilde{\boldsymbol{\tau}}, \tilde{\boldsymbol{n}}\}$ at the patch interface Γ^e . Note that the surface normals \boldsymbol{n} and $\tilde{\boldsymbol{n}}$ point out of the paper plane.

with the relations $\tilde{\boldsymbol{x}} = \boldsymbol{x}$ and $\tilde{s} = -s$ for the special case of conforming meshes that is studied in the present work. Hence, $\tilde{\boldsymbol{\tau}} = -\boldsymbol{\tau}$. For the reference configuration, these vectors are defined in analogy to Eq. (48).

The elements Ω^e and $\tilde{\Omega}^e$ share \hat{n}_{CP} control points along the interface Γ^e . These control points are denoted $\hat{\boldsymbol{x}}_e$ and are used to compute the discretized tangent vector along Γ^e ,

$$\hat{\boldsymbol{a}}_\xi \approx \hat{\mathbf{N}}_{,\xi} \hat{\boldsymbol{x}}_e, \quad (49)$$

with the shape function array

$$\hat{\mathbf{N}} = [\hat{N}_{i_1} \mathbf{1}, \hat{N}_{i_2} \mathbf{1}, \dots, \hat{N}_{i_{\hat{n}_{\text{CP}}}} \mathbf{1}]. \quad (50)$$

Given $\hat{\boldsymbol{a}}_\xi$, the tangent vector $\boldsymbol{\tau}$ is obtained from $\boldsymbol{\tau} = \hat{\boldsymbol{a}}_\xi / \|\hat{\boldsymbol{a}}_\xi\|$. Its variation is given in Eq. (113.3). Note that other surface quantities on element Ω^e , like the surface normal \boldsymbol{n} , are obtained from the shape function array \mathbf{N} and the nodal values \boldsymbol{x}_e , see Sec. 2.2. Likewise, these quantities on $\tilde{\Omega}^e$ are obtained from $\tilde{\mathbf{N}}$ and $\tilde{\boldsymbol{x}}_e$.

5.1 G^1 -continuity constraint for the surface deformation

The geometric continuity constraint of Duong et al. (2017) is summarized and simplified in this section. It can be used to enforce the four¹¹ different inter-patch conditions shown in Table 2. The table distinguishes between the general case of a kink ($\theta \neq \pi$) and the special case of a planar interface ($\theta = \pi$). In both cases either the continuity at patch interfaces or the symmetry at patch boundaries can be enforced. The vectors $\tilde{\mathbf{N}}$ and $\tilde{\boldsymbol{n}}$ denote the normal of either the neighboring patch or the symmetry plane.

In the following three subsections, the constraint enforcement for the various cases using the penalty and Lagrange multiplier method are summarized. Their linearizations are reported in Appendix B.2.

5.1.1 Constraint formulation

As shown in Table 2, the general case requires to maintain a fixed angle θ between two adjacent patches. This implies that the angle between the surface normals, which is denoted α , has to be constant for all load or time steps, i.e.

$$\alpha - \alpha_0 = 0, \quad \forall \boldsymbol{x} \in \Gamma. \quad (51)$$

¹¹A fifth possibility is to prescribe boundary rotations, see Duong et al. (2017).

Table 2: Overview of different inter-patch conditions.

	Kink	Planar
Patch interface		
Symmetry condition at a patch boundary		

To avoid the computation and differentiation of the arccos-function, the constraint is reformulated as

$$\cos \alpha - \cos \alpha_0 = 0, \quad \forall \mathbf{x} \in \Gamma, \quad (52)$$

with

$$\cos \alpha := \mathbf{n} \cdot \tilde{\mathbf{n}}, \quad \cos \alpha_0 := \mathbf{N} \cdot \tilde{\mathbf{N}}. \quad (53)$$

Note that Eq. (53) makes use of the fact that the surface normals have unit length. The constraint in Eq. (52) can uniquely handle angles within the range $[0, \pi]$. For the range $[0, 2\pi)$, however, there is an ambiguity in the solution as illustrated in Fig. 4. To avoid this ambiguity,

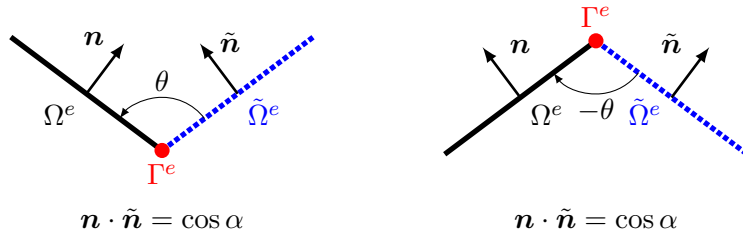


Figure 4: Ambiguity of constraint (52). Both configurations equally fulfill the constraint, which leads to an ambiguity in the numerical solution. If the constraint in Eq. (54) is considered in addition, the desired configuration will be uniquely defined.

a second constraint is incorporated, i.e.

$$\sin \alpha - \sin \alpha_0 = 0, \quad \forall \mathbf{x} \in \Gamma, \quad (54)$$

where

$$\sin \alpha := (\mathbf{n} \times \tilde{\mathbf{n}}) \cdot \boldsymbol{\tau}, \quad \sin \alpha_0 := (\mathbf{N} \times \tilde{\mathbf{N}}) \cdot \boldsymbol{\tau}_0. \quad (55)$$

Thus, the following set of constraints needs to be enforced

$$\begin{aligned} g_c &:= \cos \alpha_0 - \cos \alpha = 0, \quad \forall \mathbf{x} \in \Gamma, \\ g_s &:= \sin \alpha_0 - \sin \alpha = 0, \quad \forall \mathbf{x} \in \Gamma. \end{aligned} \quad (56)$$

The constraints in Eq. (56) can then uniquely enforce any angle $\alpha_0, \alpha \in [0, 2\pi]$.

Remark: For the planar setting that is illustrated in the third column of Table 2, the simplification $\alpha_0 = \alpha = 0$ holds true. Thus, $\cos \alpha_0 = 1$ and $\sin \alpha_0 = 0$, and Eq. (56) turns into

$$\begin{aligned} g_c^{\text{planar}} &:= 1 - \cos \alpha = 0, \quad \forall \mathbf{x} \in \Gamma, \\ g_s^{\text{planar}} &:= -\sin \alpha = 0, \quad \forall \mathbf{x} \in \Gamma. \end{aligned} \quad (57)$$

Note that the constraint $g_s^{\text{planar}} = 0$ in Eq. (57) is automatically fulfilled if $g_c^{\text{planar}} = 0$ holds. The two constraints thus simplify to

$$1 - \cos \alpha = 0, \quad \forall \mathbf{x} \in \Gamma, \quad (58)$$

which can also be expressed as

$$\mathbf{g}_n^{\text{planar}} := \mathbf{n} - \tilde{\mathbf{n}} = \mathbf{0}, \quad \forall \mathbf{x} \in \Gamma. \quad (59)$$

5.1.2 Penalty method

For the penalty method, the constraints in Eq. (56) are enforced by adding the potential

$$\Pi_n = \int_{\Gamma_0} \frac{\varepsilon_n}{2} g_n \, dS = \int_{\Gamma_0} \varepsilon_n (1 - c_0 \cos \alpha - s_0 \sin \alpha) \, dS, \quad (60)$$

to the total potential of the system. Here, $g_n := g_c^2 + g_s^2$, $c_0 := \cos \alpha_0$ and $s_0 := \sin \alpha_0$. The penalty parameter $\varepsilon_n \in (0, \infty)$ controls how well the constraint will be fulfilled. It has units of moment per length [Nm/m = N]. The expression $\varepsilon_n g_n$ remains finite as $\varepsilon_n \rightarrow \infty$ and $g_c, g_s \rightarrow 0$. The derivative of g_n with respect to α is $g'_n = 2 \sin(\alpha - \alpha_0)$. The positions of the maxima of g_n , where $g'_n = 0$, fulfill $\alpha - \alpha_0 = \pm\pi$. The minimum is found at $\alpha - \alpha_0 = 0$. A unique solution with the Newton-Raphson method can thus be obtained provided that the initial guess α_i fulfills $|\alpha_i - \alpha_0| < \pi$.

Now, the variation of the penalty potential from Eq. (60) is given by (see Appendix B.1)

$$\delta \Pi_n = - \int_{\Gamma_0} \varepsilon_n (\delta \boldsymbol{\tau} \cdot \boldsymbol{\theta} + \delta \mathbf{n} \cdot \tilde{\mathbf{d}} + \delta \tilde{\mathbf{n}} \cdot \mathbf{d}) \, dS, \quad (61)$$

with

$$\boldsymbol{\theta} := s_0 \mathbf{n} \times \tilde{\mathbf{n}} = s_0 \sin(\alpha) \boldsymbol{\tau}, \quad \tilde{\mathbf{d}} := c_0 \tilde{\mathbf{n}} + s_0 \tilde{\boldsymbol{\nu}}, \quad \mathbf{d} := c_0 \mathbf{n} + s_0 \boldsymbol{\nu}. \quad (62)$$

Using the variation of $\boldsymbol{\tau}$ given in Eq. (113.3), the first term in the expression for $\delta \Pi_n$ vanishes as $\boldsymbol{\tau} \cdot \delta \boldsymbol{\tau} = 0$. Eq. (61) then simplifies to¹²

$$\delta \Pi_n = - \int_{\Gamma_0} \varepsilon_n (\delta \mathbf{n} \cdot \tilde{\mathbf{d}} + \delta \tilde{\mathbf{n}} \cdot \mathbf{d}) \, dS. \quad (63)$$

Eq. (63) implies that the bending moments are transmitted exactly across the interface. They are given by $m_\tau = m_{\tilde{\tau}} = \varepsilon_n \sin(\alpha - \alpha_0)$, see Appendix A.1.¹³ The missing variations $\delta \mathbf{n}$ and $\delta \tilde{\mathbf{n}}$ in Eq. (63) are given in Appendix B.1. Inserting the FE approximations yields the element-level approximation of Eq. (63)

$$\delta \Pi_n^e := \delta \mathbf{x}_e^T \mathbf{f}_n^e + \delta \tilde{\mathbf{x}}_e^T \mathbf{f}_{\tilde{n}}^e. \quad (64)$$

¹²This is a simplification compared to the formulation of Duong et al. (2017).

¹³Note that the bending moments have been changed compared to the journal version.

The element-level force vectors in Eq. (64) are given by

$$\begin{aligned}\mathbf{f}_n^e &:= \int_{\Gamma_0^e} \varepsilon_n \mathbf{N}_{,\alpha}^T(\tilde{\mathbf{d}} \cdot \mathbf{a}^\alpha) \mathbf{n} \, dS, \\ \mathbf{f}_n^{\tilde{e}} &:= \int_{\Gamma_0^e} \varepsilon_n \tilde{\mathbf{N}}_{,\alpha}^T(\mathbf{d} \cdot \tilde{\mathbf{a}}^\alpha) \tilde{\mathbf{n}} \, dS,\end{aligned}\tag{65}$$

with shape function array \mathbf{N} from Eq. (9) and Γ_0^e denoting a finite line element along the patch interface. The force vectors \mathbf{f}_n^e and $\mathbf{f}_n^{\tilde{e}}$ have dimension $3n_e \times 1$ and $3n_{\tilde{e}} \times 1$, respectively. Here, n_e and $n_{\tilde{e}}$ refer to the number of control points associated with the elements Ω^e and $\tilde{\Omega}^e$, respectively.

Remark: Plugging $\alpha_0 = 0$ into the force vectors in Eq. (65), leads to the simplified force vectors

$$\begin{aligned}\mathbf{f}_n^{e,\text{planar}} &:= \int_{\Gamma_0^e} \varepsilon_n \mathbf{N}_{,\alpha}^T(\tilde{\mathbf{n}} \cdot \mathbf{a}^\alpha) \mathbf{n} \, dS = \int_{\Gamma_0^e} \varepsilon_n \mathbf{N}_{,\alpha}^T(\mathbf{n} \otimes \tilde{\mathbf{n}}) \mathbf{a}^\alpha \, dS, \\ \mathbf{f}_n^{\tilde{e},\text{planar}} &:= \int_{\Gamma_0^e} \varepsilon_n \tilde{\mathbf{N}}_{,\alpha}^T(\mathbf{n} \cdot \tilde{\mathbf{a}}^\alpha) \tilde{\mathbf{n}} \, dS = \int_{\Gamma_0^e} \varepsilon_n \tilde{\mathbf{N}}_{,\alpha}^T(\tilde{\mathbf{n}} \otimes \mathbf{n}) \tilde{\mathbf{a}}^\alpha \, dS,\end{aligned}\tag{66}$$

for the penalty method.

5.1.3 Lagrange multiplier method

For the Lagrange multiplier approach, the constraints in Eq. (56) are reformulated as follows

$$\begin{aligned}\bar{g}_c &:= 1 - \cos(\alpha - \alpha_0) = 0, \\ \bar{g}_s &:= \sin(\alpha - \alpha_0) = 0,\end{aligned}\tag{67}$$

to guarantee unique solutions with the Newton-Raphson method as long as $|\alpha_i - \alpha_0| < \pi/4$, with initial guess α_i (Duong et al., 2017). The new potential then is

$$\Pi_n = \int_{\Gamma_0} q (\bar{g}_c + \bar{g}_s) \, dS = \int_{\Gamma_0} q (1 - \cos(\alpha - \alpha_0) + \sin(\alpha - \alpha_0)) \, dS,\tag{68}$$

with Lagrange multiplier $q \in L^2(\Gamma_0)$. Using Eqs. (111)–(112), the variation of the Lagrange multiplier potential in Eq. (68) is given by

$$\delta\Pi_n = \int_{\Gamma_0} \delta q (\bar{g}_c + \bar{g}_s) \, dS - \int_{\Gamma_0} q (\delta\boldsymbol{\tau} \cdot \boldsymbol{\theta} + \delta\mathbf{n} \cdot \tilde{\mathbf{d}} + \delta\tilde{\mathbf{n}} \cdot \mathbf{d}) \, dS,\tag{69}$$

with the redefinitions

$$\boldsymbol{\theta} := (s_0 - c_0) \mathbf{n} \times \tilde{\mathbf{n}}, \quad \mathbf{d} := (s_0 + c_0) \mathbf{n} + (s_0 - c_0) \boldsymbol{\nu}, \quad \tilde{\mathbf{d}} := (s_0 + c_0) \tilde{\mathbf{n}} + (s_0 - c_0) \tilde{\boldsymbol{\nu}},\tag{70}$$

and the variation of the Lagrange multiplier $\delta q \in L^2(\Gamma_0)$. Eq. (69) simplifies to¹²

$$\delta\Pi_n = \int_{\Gamma_0} \delta q (\bar{g}_c + \bar{g}_s) \, dS - \int_{\Gamma_0} q (\delta\mathbf{n} \cdot \tilde{\mathbf{d}} + \delta\tilde{\mathbf{n}} \cdot \mathbf{d}) \, dS,\tag{71}$$

since $\boldsymbol{\tau} \cdot \delta\boldsymbol{\tau} = 0$, see previous section. Eq. (71) implies that the bending moment $m_\tau = m_{\tilde{\tau}} = q$ is transmitted exactly across the patch interface, see Appendix A.2.¹⁴ The FE approximation of the Lagrange multiplier along Γ^e can be written as

$$q \approx \hat{\mathbf{N}}_q \hat{\mathbf{q}}_e,\tag{72}$$

¹⁴Note that the bending moments have been changed compared to the journal version.

where $\hat{\mathbf{N}}_q$ and $\hat{\mathbf{q}}_e$ are the corresponding shape function array and nodal values of line element Γ^e , respectively, similar to Eqs. (49)–(50). The discretized form of the system with Lagrange multipliers is a saddle-point problem that has a zero-tangent block in the stiffness matrix, see Eq. (129.3). The chosen finite-dimensional subspace for the Lagrange multiplier thus must satisfy the LBB-condition in order to obtain a stable solution. In the present work, the displacement field \mathbf{x} and its variation $\delta\mathbf{x}$ are interpolated by C^1 -continuous, bi-quadratic NURBS and the Lagrange multiplier q with either C^{-1} - or C^0 -continuous functions. The latter are obtained by either a constant interpolation on each line element along the patch interfaces, or linear interpolation, see Fig. 2. Brivadis et al. (2015) investigate suitable Lagrange multiplier spaces depending on the approximation order of the primal variable for a displacement constraint used for non-conforming meshes. For this, the element-wise constant interpolation of q is shown to be LBB-stable for the used bi-quadratic approximation of \mathbf{x} . The authors note that there is no proof on LBB-stability for the normal constraints used for conforming meshes, but the results in Duong et al. (2017) and Sec. 6.1 indicate a stable method for the considered examples. Note that for the element-wise linear interpolation, the Lagrange multipliers need to be repeated at patch junctions with valence greater than or equal to three in order to avoid over-constraining. A more detailed mathematical investigation on this is left open for future work, also see Sec. 6.4. The discretized element-level variation of the Lagrange multiplier potential is given by

$$\delta\Pi_n^e = \delta\mathbf{x}_e^T \bar{\mathbf{f}}_n^e + \delta\tilde{\mathbf{x}}_e^T \bar{\mathbf{f}}_{\tilde{n}}^e + \delta\mathbf{q}_e^T \bar{\mathbf{f}}_q^e, \quad (73)$$

with the force vectors

$$\begin{aligned} \bar{\mathbf{f}}_n^e &:= \int_{\Gamma_0^e} q \mathbf{N}_{,\alpha}^T (\tilde{\mathbf{d}} \cdot \mathbf{a}^\alpha) \mathbf{n} \, dS, \\ \bar{\mathbf{f}}_{\tilde{n}}^e &:= \int_{\Gamma_0^e} q \tilde{\mathbf{N}}_{,\alpha}^T (\mathbf{d} \cdot \tilde{\mathbf{a}}^\alpha) \tilde{\mathbf{n}} \, dS, \\ \bar{\mathbf{f}}_q^e &:= \int_{\Gamma_0^e} \hat{\mathbf{N}}_q^T (\bar{g}_c + \bar{g}_s) \, dS. \end{aligned} \quad (74)$$

Here, the variables \mathbf{d} and $\tilde{\mathbf{d}}$ are defined in Eq. (70). The force vectors $\bar{\mathbf{f}}_n^e$ and $\bar{\mathbf{f}}_{\tilde{n}}^e$ have dimension $3n_e \times 1$ and $3n_{\tilde{e}} \times 1$, respectively. Here, n_e and $n_{\tilde{e}}$ refer to the number of control points associated with the elements Ω^e and $\tilde{\Omega}^e$, respectively. Further, $\bar{\mathbf{f}}_q^e$ has dimension $n_q \times 1$ with n_q denoting the number of Lagrange multipliers on the line element Γ^e , see Fig. 2.

Remark: Note that the Lagrange multiplier method only converges correctly if it is integrated consistently. So for constant interpolation of the Lagrange multiplier, one should not use the trapezoidal rule, while for linear interpolation, the midpoint rule should not be used.

Remark: For the simplified constraint in Eq. (59), the first two force vectors in Eq. (74) are simplified by substituting $\mathbf{d} \leftarrow \mathbf{d}^{\text{planar}}$ and $\tilde{\mathbf{d}} \leftarrow \tilde{\mathbf{d}}^{\text{planar}}$, where

$$\mathbf{d}^{\text{planar}} := \mathbf{n} - \boldsymbol{\nu}, \quad \tilde{\mathbf{d}}^{\text{planar}} := \tilde{\mathbf{n}} - \tilde{\boldsymbol{\nu}}. \quad (75)$$

The force vector $\bar{\mathbf{f}}_q^e$ in Eq. (74) stays the same.

5.2 C^1 -continuity constraint for the phase field

This section discusses formulations to enforce C^1 -continuity for the phase field ϕ within the weak forms (23) and (31). Their linearization is outlined in Appendix B.3.

5.2.1 Constraint formulation

As Fig. 5 illustrates, the surface gradients of the phase field, $\nabla_s \phi$ and $\nabla_s \tilde{\phi}$, need to be equal to ensure C^1 -continuity of ϕ . The constraint can thus be written as

$$\nabla_s \phi - \nabla_s \tilde{\phi} = \mathbf{0}, \quad \forall \mathbf{x} \in \Gamma. \quad (76)$$

The parametrization of the elements $\tilde{\Omega}^e$ and Ω^e is the same along the interface because here, conforming meshes are considered, see Fig. 3. Thus, by construction, the tangential component

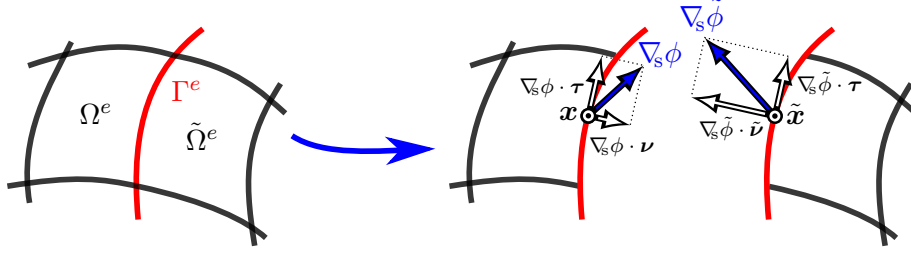


Figure 5: Surface gradients $\nabla_s \phi$ and $\nabla_s \tilde{\phi}$ at points \mathbf{x} and $\tilde{\mathbf{x}}$, respectively. Due to conforming meshes at the interface Γ^e , the parametrization along the interface is the same for both patches.¹⁵ Thus, the tangential component of the surface gradients is equal by construction, i.e. $\nabla_s \phi \cdot \boldsymbol{\tau} = \nabla_s \tilde{\phi} \cdot \boldsymbol{\tau}$. Only their normal components need to be enforced to be equal, see Eq. (77).

of $\nabla_s \phi$ is already C^1 -continuous across the patch interface. Hence, only its normal component needs to be enforced to be equal. The constraint in Eq. (76) then simplifies to

$$g_{\nabla} := \nabla_s \phi \cdot \boldsymbol{\nu} + \nabla_s \tilde{\phi} \cdot \tilde{\boldsymbol{\nu}} = 0, \quad \forall \mathbf{x} \in \Gamma. \quad (77)$$

It has the unit $[\text{m}^{-1}]$. In the case of fracture, the gradients are evaluated in the reference configuration and hence, constraint (77) is rewritten as

$$g_{\nabla}^{\text{frac}} := \nabla_S \phi \cdot \boldsymbol{\nu}_0 + \nabla_S \tilde{\phi} \cdot \tilde{\boldsymbol{\nu}}_0 = 0, \quad \forall \mathbf{x} \in \Gamma. \quad (78)$$

Based on Eq. (6.1), Eq. (77) can be rewritten as

$$g_{\nabla} = \phi_{,\alpha} \mathbf{a}^\alpha \cdot \boldsymbol{\nu} + \tilde{\phi}_{,\alpha} \tilde{\mathbf{a}}^\alpha \cdot \tilde{\boldsymbol{\nu}} = 0, \quad \forall \mathbf{x} \in \Gamma. \quad (79)$$

Keeping \mathbf{x} fixed, the variation of Eq. (79) is given by

$$\delta g_{\nabla} = \delta \phi_{,\alpha} \mathbf{a}^\alpha \cdot \boldsymbol{\nu} + \delta \tilde{\phi}_{,\alpha} \tilde{\mathbf{a}}^\alpha \cdot \tilde{\boldsymbol{\nu}}. \quad (80)$$

Keeping \mathbf{x} fixed is sufficient for building a numerical method, even though it introduces a variational inconsistency as is noted below. The reason is that constraint (79) is used for the phase field, and not for the displacement field. Thus, the latter can be fixed in the variation and hence, Eq. (80) does not include the variations of the tangent vectors \mathbf{a}^α , $\tilde{\mathbf{a}}^\alpha$ or the interface normals $\boldsymbol{\nu}$, $\tilde{\boldsymbol{\nu}}$, which simplifies the numerical formulations greatly. The linearization of g_{∇} and δg_{∇} , however, needs to include the linearizations with respect to \mathbf{x} , see Appendix B.1, in order to ensure quadratic convergence of the Newton-Raphson method. Based on the FE approximations in Eq. (10) and the analogous quantities for $\tilde{\phi}$, the variation of the constraint in Eq. (80) is discretized as

$$\delta g_{\nabla} \approx \delta \boldsymbol{\phi}_e^T \bar{\mathbf{N}}_{,\alpha}^T (\mathbf{a}^\alpha \cdot \boldsymbol{\nu}) + \delta \tilde{\boldsymbol{\phi}}_e^T \tilde{\bar{\mathbf{N}}}_{,\alpha}^T (\tilde{\mathbf{a}}^\alpha \cdot \tilde{\boldsymbol{\nu}}), \quad (81)$$

¹⁵Note that the parametrizations of elements Ω^e and $\tilde{\Omega}^e$ might be different. But for the line integrals, only the parametrization of the patch interface Γ^e is of importance.

where the tangent vectors and interface normals are also understood to be discrete.

Remark: In the case of planar connections of patches, the relation $\mathbf{n} = \tilde{\mathbf{n}}$ can be used, see Eq. (59). From Eq. (48) then follows that $\boldsymbol{\nu} = -\tilde{\boldsymbol{\nu}}$. The general constraint in Eq. (79) now simplifies to

$$g_{\nabla}^{\text{planar}} = \left(\phi_{,\alpha} \mathbf{a}^\alpha - \tilde{\phi}_{,\alpha} \tilde{\mathbf{a}}^\alpha \right) \cdot \boldsymbol{\nu} = 0, \quad \forall \mathbf{x} \in \Gamma. \quad (82)$$

Its variation is then given by

$$\delta g_{\nabla}^{\text{planar}} = \left(\delta \phi_{,\alpha} \mathbf{a}^\alpha - \delta \tilde{\phi}_{,\alpha} \tilde{\mathbf{a}}^\alpha \right) \cdot \boldsymbol{\nu}. \quad (83)$$

The following sections discuss a penalty and a Lagrange multiplier approach to enforce these constraints. Both methods are based on a potential Π_{∇} that is added to the system's total potential. Its variation and discretization will be outlined. Their linearization is derived in Appendix B.3.

Remark: In the present work, only planar connections are considered for the phase separation examples in Sec. 6.2. In contrast, the fracture examples in Sec. 6.3 include the more general case of non-smooth connections between patches, but the phase field gradient is based on the reference configuration. To cover all cases, the following derivations only contain the general case.

5.2.2 Penalty method

In analogy to the penalty potential for the G^1 -constraint, see Eq. (60), the penalty potential for the phase field constraint in Eq. (79) is given by

$$\Pi_{\nabla} = \int_{\Gamma_0} \frac{\varepsilon_\phi}{2} g_{\nabla}^2 \, dS, \quad (84)$$

where the penalty parameter $\varepsilon_\phi \in (0, \infty)$ with units $[\text{kg m}^3/\text{s}^2]$ controls how well the constraint will be fulfilled. The variation of Π_{∇} is

$$\delta \Pi_{\nabla} = \int_{\Gamma_0} \varepsilon_\phi g_{\nabla} \delta g_{\nabla} \, dS, \quad (85)$$

where δg_{∇} is given in Eq. (80).¹⁶ Based on Eq. (81), the discretized variation of the penalty potential becomes

$$\delta \Pi_{\nabla}^e = \delta \boldsymbol{\phi}_e^T \mathbf{f}_\phi^e + \delta \tilde{\boldsymbol{\phi}}_e^T \mathbf{f}_{\tilde{\phi}}^e. \quad (86)$$

The general force vectors in Eq. (86) are given by¹⁷

$$\begin{aligned} \mathbf{f}_\phi^e &:= \int_{\Gamma_0^e} \varepsilon_\phi \bar{\mathbf{N}}_{,\alpha}^T g_{\nabla} (\mathbf{a}^\alpha \cdot \boldsymbol{\nu}) \, dS, \\ \mathbf{f}_{\tilde{\phi}}^e &:= \int_{\Gamma_0^e} \varepsilon_\phi \tilde{\mathbf{N}}_{,\alpha}^T g_{\nabla} (\tilde{\mathbf{a}}^\alpha \cdot \tilde{\boldsymbol{\nu}}) \, dS, \end{aligned} \quad (87)$$

with g_{∇} from Eq. (79).

¹⁶Since \mathbf{x} is kept fixed in δg_{∇} , Eq. (85) is not the full variation of Π_{∇} .

¹⁷Note that the strong form is multiplied with the factor $2 \ell_0 / \mathcal{G}_c$ in the phase field model for fracture (Paul et al., 2020). The force vectors are thus, implicitly scaled with this factor.

Choice of the penalty parameter

Based on numerical investigations, the following penalty parameter for phase separations is proposed

$$\varepsilon_\phi = \varepsilon_\phi^0 2^{d(p-1)}, \quad (88)$$

with $\varepsilon_\phi^0 = 1000 N\omega L_0^3$. Here, L_0 refers to a reference length stemming from the non-dimensionalization of Zimmermann et al. (2019), see Sec. 6.2. The polynomial order of the discretization is p and the refinement depth is denoted d . According to Eq. (88), finer meshes will lead to a larger penalty parameter.

For brittle fracture, the following problem-independent penalty parameter is proposed

$$\varepsilon_\phi = \varepsilon_\phi^0 \frac{\Delta t_{\max}}{\Delta t} \frac{1}{\Delta x_{\min}^\Gamma} \frac{\Delta x_{\max}^\Gamma}{\Delta x^\Gamma}, \quad (89)$$

with $\varepsilon_\phi^0 = 0.1 E_0 L_0^4$.¹⁸ The reference stiffness E_0 ([N/m] = [kg/s²]) and length L_0 ([m]) stem from the non-dimensionalization described in Paul et al. (2020). Further, Δx_{\min}^Γ and Δx_{\max}^Γ refer to the minimum and maximum length of the line elements along the patch interfaces, respectively, whereas Δx^Γ refers to the one from the currently considered line element. The current and maximum time steps are Δt and Δt_{\max} , respectively. The proposed penalty parameter in Eq. (89) leads to the following behavior:

- In case of crack evolution, the adaptive time stepping scheme from Paul et al. (2020) can lead to small time steps. The scaling with $1/\Delta t$ then ensures a high penalty parameter in case of crack evolution, whereas the penalty parameter is kept smaller in case of no crack propagation (when the phase field does not change significantly).
- In cases of uniform meshes, the scaling factor $1/\Delta x_{\min}^\Gamma$ will ensure that the penalty parameter increases with mesh refinement. A similar behavior is obtained with the penalty parameter for the phase transition model, see Eq. (88).
- In cases of locally refined meshes, which are often used in phase field fracture models, the scaling factor $\Delta x_{\max}^\Gamma/\Delta x^\Gamma$ increases the penalty parameter in regions of highly resolved meshes. Thus, the constraint will be fulfilled more accurately in regions of fracture since these are the areas of primary interest, also see Sec. 6.3.1.

The value $\varepsilon_\phi^0 = 0.1 E_0 L_0^4$ seems small, but it yields sufficiently accurate results while preventing ill-conditioning, see Sec. 6.3.1.

5.2.3 Lagrange multiplier method

In the following, a Lagrange multiplier approach to enforce constraint (79) is described. Since the constraint is scalar, the additional potential reads

$$\Pi_\nabla = \int_{\Gamma_0} \lambda g_\nabla \, dS, \quad (90)$$

with Lagrange multiplier $\lambda \in L^2(\Gamma_0)$. The variation of potential (90) is

$$\delta \Pi_\nabla = \int_{\Gamma_0} \delta \lambda g_\nabla \, dS + \int_{\Gamma_0} \lambda \delta g_\nabla \, dS, \quad (91)$$

¹⁸Note that for fracture, ε_ϕ and ε_ϕ^0 have different units since the first one is scaled by $1/\Delta x_{\min}^\Gamma$, which introduces the units of [m⁻¹].

where δg_∇ is given in Eq. (80) and $\delta\lambda \in L^2(\Gamma_0)$ is the variation of the Lagrange multiplier. LBB-stability applies analogously to Sec. 5.1.3. The FE approximations of the Lagrange multiplier and its variation are

$$\lambda \approx \hat{\mathbf{N}}_\lambda \hat{\boldsymbol{\lambda}}_e, \quad \text{and} \quad \delta\lambda \approx \hat{\mathbf{N}}_\lambda \delta\hat{\boldsymbol{\lambda}}_e, \quad (92)$$

with shape function array

$$\hat{\mathbf{N}}_\lambda := [N_{i_1}], \quad \text{or} \quad \hat{\mathbf{N}}_\lambda := [N_{i_1}, N_{i_2}], \quad (93)$$

depending on the order of interpolation (constant or linear, respectively). The nodal values of the Lagrange multipliers and their variation are denoted $\hat{\boldsymbol{\lambda}}_e$ and $\delta\hat{\boldsymbol{\lambda}}_e$, respectively. These and the shape function array in Eq. (93) are defined on the patch interfaces, in analogy to Eqs. (49)–(50). Using the FE approximations of $\delta\lambda$ from Eq. (92) and of δg_∇ from Eq. (81), the discretized variation of the Lagrange multiplier potential becomes

$$\delta\Pi_\nabla^e = \delta\phi_e^T \bar{\mathbf{f}}_\phi^e + \delta\tilde{\phi}_e^T \bar{\mathbf{f}}_\tilde{\phi}^e + \delta\hat{\boldsymbol{\lambda}}_e^T \bar{\mathbf{f}}_\lambda^e. \quad (94)$$

The general force vectors in Eq. (94) are given by

$$\begin{aligned} \bar{\mathbf{f}}_\phi^e &:= \int_{\Gamma_0^e} \bar{\mathbf{N}}_{,\alpha}^T \lambda (\mathbf{a}^\alpha \cdot \boldsymbol{\nu}) \, dS, \\ \bar{\mathbf{f}}_{\tilde{\phi}}^e &:= \int_{\Gamma_0^e} \tilde{\mathbf{N}}_{,\alpha}^T \lambda (\tilde{\mathbf{a}}^\alpha \cdot \tilde{\boldsymbol{\nu}}) \, dS, \\ \bar{\mathbf{f}}_\lambda^e &:= \int_{\Gamma_0^e} \hat{\mathbf{N}}_\lambda^T g_\nabla \, dS, \end{aligned} \quad (95)$$

with g_∇ from Eq. (79).

6 Numerical examples

This section shows several numerical examples that illustrate the influence of the patch constraints from Sec. 5 on the numerical solution. At first, Sec. 6.1 focuses on the pure shell framework and the influence of the G^1 -continuity constraint from Sec. 5.1. Secondly, phase transitions on thin shells, which are based on a multi-patch description, are investigated in Sec. 6.2. Similar investigations are made for brittle fracture in Sec. 6.3.

In the subsequent sections, the following notation is used: The surface consists of n_{patch} patches, which are discretized by n_{sel} surface elements and n_{CP} control points. The penalty method is abbreviated by PM and the Lagrange multiplier method with constant/linear interpolation by constant/linear LMM. For all examples, bi-quadratic NURBS are used for the interpolation of \mathbf{x} , $\delta\mathbf{x}$, ϕ and $\delta\phi$.

Remark: Numerical integration of surface integrals $\int_{\Omega_0^e} \dots dS$ is performed using $(p+1) \times (q+1)$ Gaussian quadrature points. Here, p and q refer to the polynomial orders in the two parametric directions ξ^α , $\alpha = 1, 2$. In contrast, the integration of n_{el} line integrals $\int_{\Gamma_0^e} \dots dS$ is performed using a different number of quadrature points n_{qp} . If not stated otherwise, Gaussian quadrature with $n_{\text{qp}} = 3$ is used. For $n_{\text{qp}} = 1$ this corresponds to the midpoint rule, whereas for $n_{\text{qp}} = 2$, the trapezoidal rule ($n_{\text{qp}} = 2$, Trapezoidal) is used instead of Gaussian quadrature.

6.1 Deforming shells

This section investigates the G^1 -continuity constraint from Sec. 5.1 within the pure mechanical shell framework (where ϕ is not unknown). The discussion includes comparisons to given solutions and convergence rates. The examples in this section are based on quasi-static conditions. In contrast to the work of Duong et al. (2017), here, a simpler formulation is derived and used, see Secs. 5.1.2–5.1.3. Further, patch junctions with valence three and five are investigated since these kinds of junctions are of special interest for spline parametrizations.

6.1.1 Pure bending

First, the pure bending of an initially flat shell is considered. Here, the Canham material model is used, see Duong et al. (2017). The same material parameters as in their work are used. The problem is normalized by the unit length L_0 and the unit stiffness c . The setup is depicted in Figs. 6a and 7a for different number of patches. As shown, a distributed bending moment

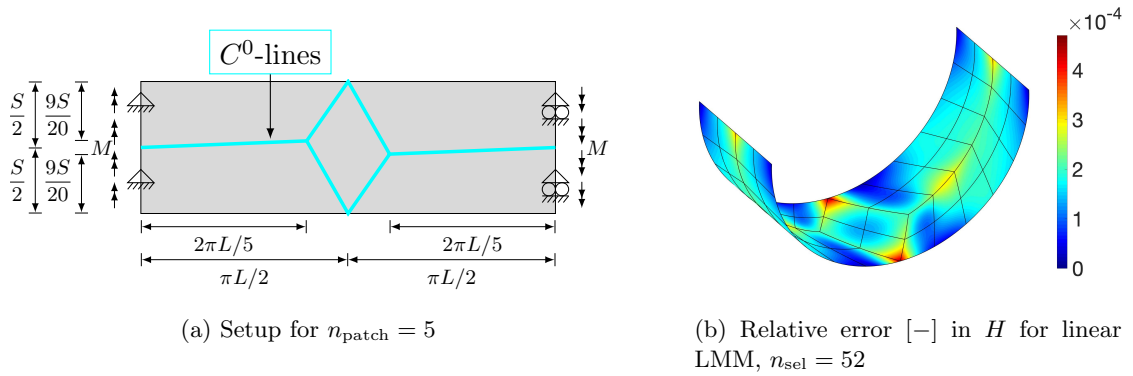


Figure 6: Pure bending: (a) Five-patch geometry (the out-of-plane movement is constrained at the left and right edge) and (b) relative error in the mean curvature H plotted over the deformed configuration.

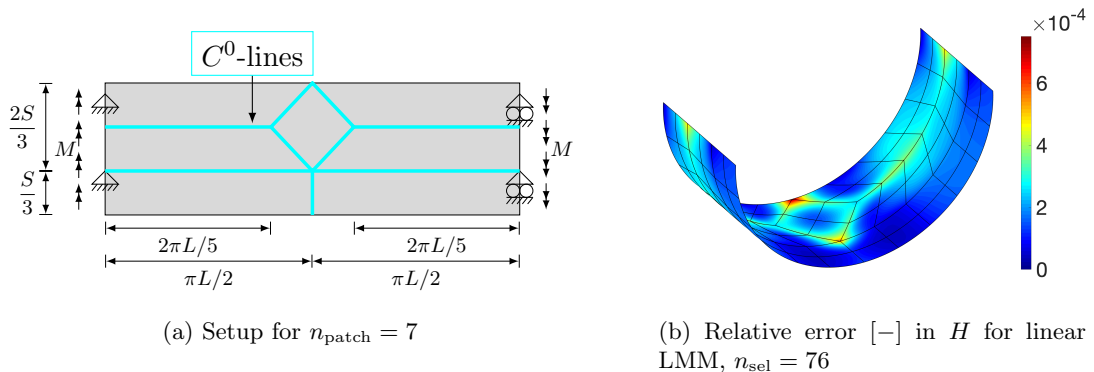


Figure 7: Pure bending: (a) Seven-patch geometry (the out-of-plane movement is constrained at the left and right edge) and (b) relative error in the mean curvature H plotted over the deformed configuration.

$M = 1 c_0 L_0^{-1}$ is applied at the two opposite edges to obtain pure bending. Figs. 6b and 7b show the relative error of the mean curvature H in comparison to the analytical solution given in Sauer

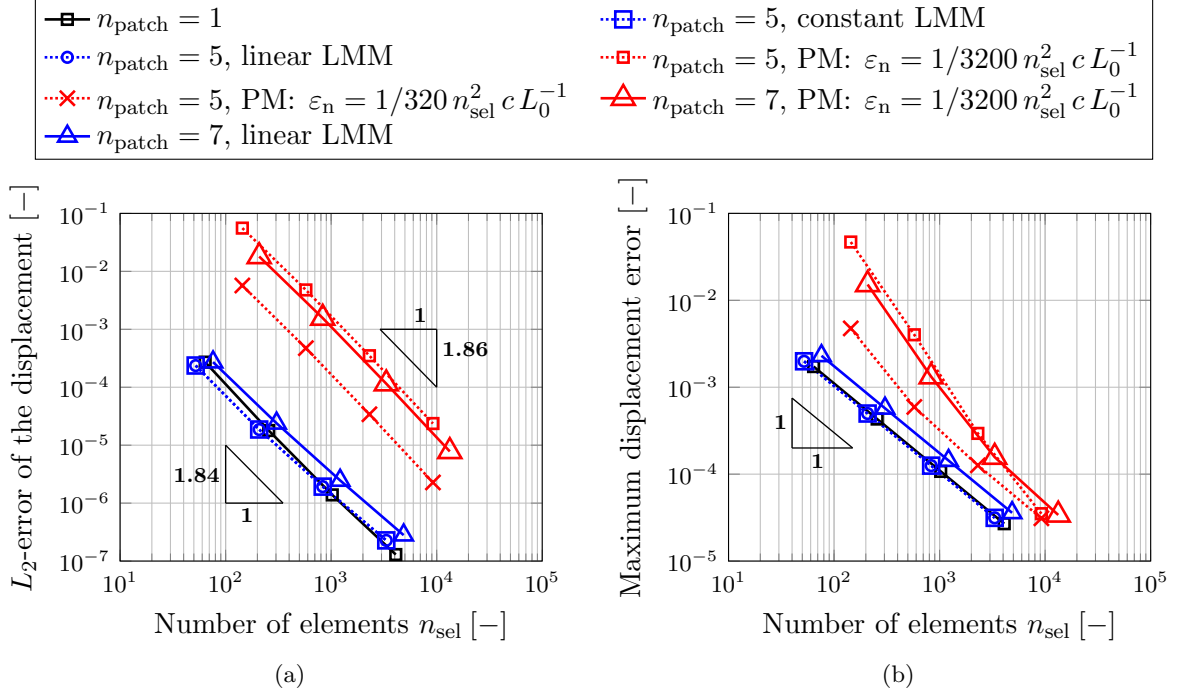


Figure 8: Pure bending: Convergence of the proposed method with respect to (a) the L_2 -error of the displacement and (b) the maximum displacement error.

and Duong (2017). Fig. 8 shows the L_2 - and maximum displacement error for an increasing number of elements. For reference, the error decay for an increasing number of elements using a single patch is shown. The convergence rates for the penalty and Lagrange multiplier method are nearly the same.¹⁹ No difference between constant and linear interpolation of the Lagrange multipliers can be observed. This is due to the fact that the bending moment is constant everywhere. Hence, a constant Lagrange multiplier interpolation is sufficient.

6.1.2 Pinching of a hemisphere

This section investigates the pinching of a hemisphere. Here, a three-dimensional Saint Venant-Kirchhoff material model is used, see Duong et al. (2017), using the same material parameters as Belytschko et al. (1985). The problem is normalized by the unit length L_0 and the 3D unit modulus \tilde{E}_0 (measured as force/area). The setup consists either of a single degenerated patch or three patches, see Fig. 9. Along the vertical edges, the symmetry constraint for smooth patch connections (see Table 2) is enforced by the Lagrange multiplier method using constant interpolation. External forces of magnitude $F = 2 \tilde{E}_0 L_0^2$ act on the lower corners, see Fig. 9.

Fig. 10 shows the normalized displacement over the number of elements. It is measured under the points loads and the reference displacement is $0.0924129 L_0$ (Dedoncker et al., 2018). The black line marks the reference solution using a single-patch discretization. Good convergence is obtained, except for the case, when the constraint is not enforced. In that case, the solution converges to a slightly larger displacement.

¹⁹The convergence behavior of the penalty method strongly depends on the penalty parameter. Here, uniform refinement is considered such that n_{sel} is inversely proportional to the area of the surface elements adjacent to the patch interfaces. This area is the relevant quantity affecting the constraint behavior and convergence rate.

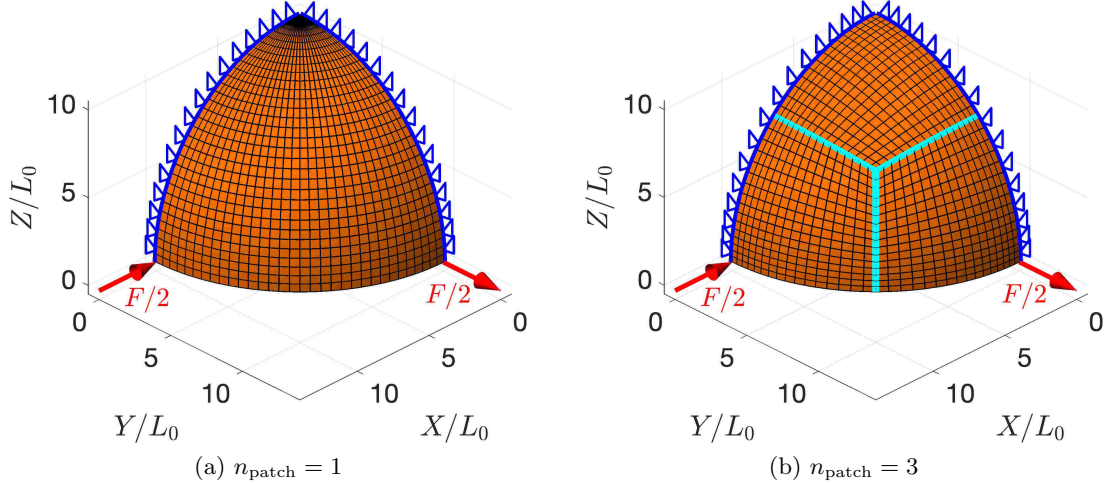


Figure 9: Pinching of a hemisphere: Discretizations of a quarter model using (a) a single-patch or (b) three patches. The bold cyan-colored lines mark the patch interfaces. The dark blue lines mark the patch boundaries where symmetry is enforced.

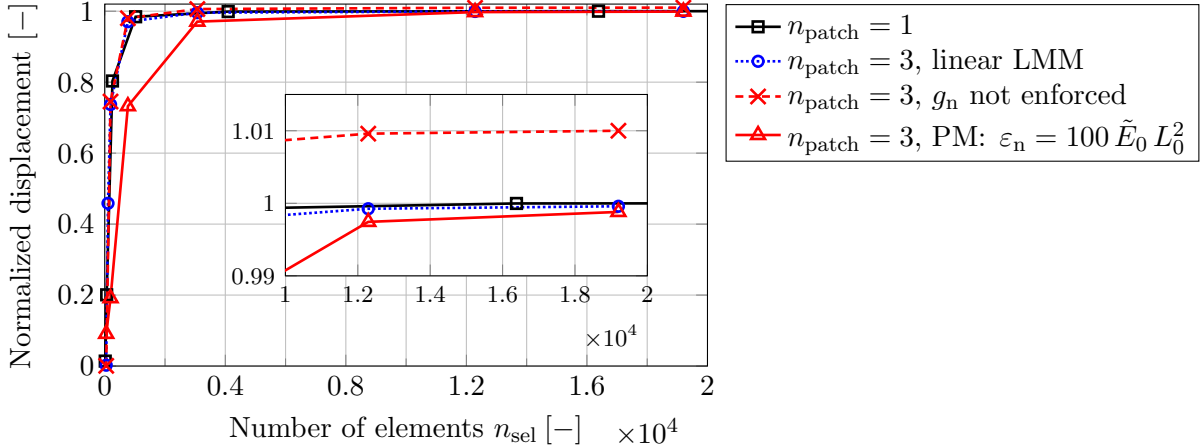


Figure 10: Pinching of a hemisphere: Normalized displacement over the mesh refinement.

6.2 Phase separation on deforming shells

This section investigates phase separation according to the theory from Sec. 3. The color coding of the phase field follows a blue ($\phi = 0$) to red ($\phi = 1$) transition, see Fig. 1a. For the examples in this section, the simplified phase field constraint for the special case of planar patch connections is used, see Eq. (82). The lines of reduced continuity are referred to as C^0 -lines. In all examples, the initial concentration field is set to

$$\phi(\xi^\alpha, 0) = \bar{\phi} + \phi_r(\xi^\alpha), \quad (96)$$

with $\bar{\phi} = 1/3$ and random distribution $\phi_r \in [-0.05, 0.05]$, if not stated otherwise. The mechanical material model of Eqs. (16)–(17) is used together with the parameters given in Table 3 with 2D Young’s modulus $E = N\omega$ and Poisson’s ratio $\nu = 0.3$. All quantities are dimensionless by the introduction of a reference length L_0 , time T_0 and energy density Ψ_0 . From this, a reference modulus $E_0 = E$ and density $\rho_0 = T_0^2 \Psi_0 / L_0^2$ follow (Zimmermann et al., 2019). Further, $N\omega = \Psi_0$ and $Nk_B T = \Psi_0/3$ are chosen.

Table 3: Material parameters for the phase separation examples.

	Pure phase state $\phi = 0$ (blue color)	Pure phase state $\phi = 1$ (red color)
K_i	$K_0 = 1.25 \frac{E_0 \nu}{(1 + \nu)(1 - 2\nu)}$	$K_1 = 0.0375 \frac{E_0 \nu}{(1 + \nu)(1 - 2\nu)}$
G_i	$G_0 = 6.25 \frac{E_0}{2(1 + \nu)}$	$G_1 = 0.375 \frac{E_0}{2(1 + \nu)}$
c_i	$c_0 = 0.01 E_0 L_0^2$	$c_1 = 0.0001875 E_0 L_0^2$
η_i	$\eta_0 = 1.5 K_0 T_0$	$\eta_1 = 1.5 K_0 T_0$

6.2.1 Pressurized torus

This section investigates phase separation on a torus, which is subjected to the constant internal pressure $p = 0.09 E_0 L_0^{-1}$. The geometry is shown in Fig. 11a. The major and minor radii are $1.3 L_0$ and $0.2 L_0$, respectively. The length scale parameter is $\ell = \sqrt{0.075} L_0$. The cyan-colored line shows a patch interface, where the surface discretization is only C^0 -continuous. Given a continuous parametrization of the torus, the C^0 -line is obtained by knot insertion at the respective position in the global knot vector. Figs. 11b–11c illustrate the evolution of the phase

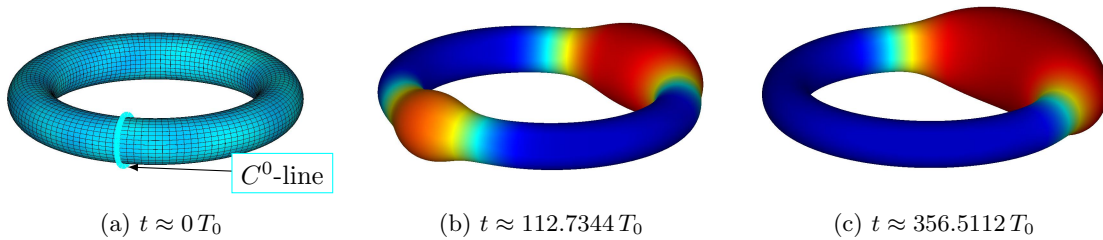


Figure 11: Pressurized torus: (a) Geometry with a C^0 -line (marked by the bold cyan-colored line), and (b)–(c) evolution of the phase field and mechanical deformation for the case that the constraints are fulfilled with the Lagrange multiplier method using constant interpolation.

field and the mechanical deformation using a mesh consisting of $n_{\text{CP}} = 4128$ control points and the Lagrange multiplier method with constant interpolation to enforce the two constraints of Eqs. (59) and (82). The results show good agreement with the results from an overall C^1 -continuous discretization with $n_{\text{CP}} = 4096$ control points. This is illustrated in Fig. 12, where the relative error of the Cahn-Hilliard energy is plotted over time.²⁰ The enforcement of the continuity constraints using the penalty method shows similarly good results. The black dash-dotted line shows the relative error when the continuity constraints are not enforced. As a result of this insufficient discretization, the error is several orders of magnitude larger compared to the results without constraint enforcement. Fig. 13 visualizes the deformed configuration for the case that the constraints are not enforced. Already at early times, the insufficient discretization leads to kinks in the geometry that attract phase separation, see Fig. 13a and its enlargement in Fig. 13b. Also, the stresses show non-physical peaks at the C^0 -line, see Fig. 13c. Here, the elastic surface tension

$$\gamma_{\text{el}} = \frac{1}{2} N_{\text{el}}^{\alpha\beta} a_{\alpha\beta} \quad (97)$$

²⁰The time steps of the two simulations are not coinciding. Therefore, the energy is linearly interpolated between the time steps to compute the relative energy difference.

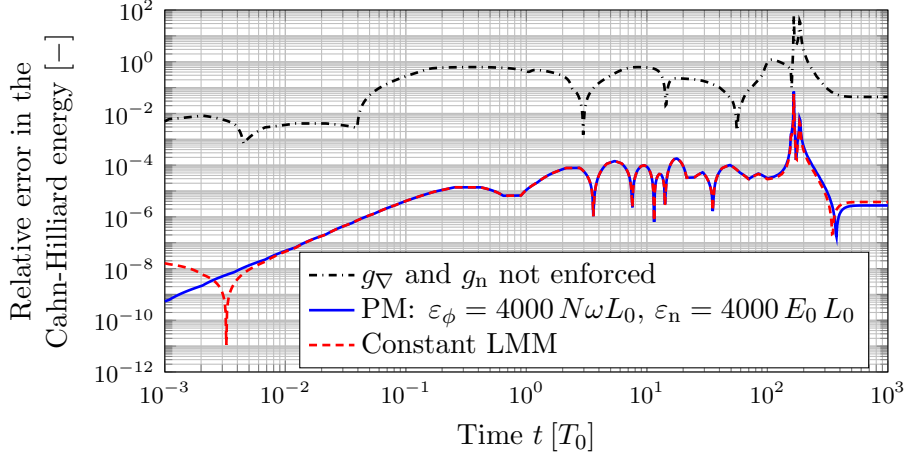


Figure 12: Pressurized torus: Relative error of the Cahn-Hilliard energy over time. The results from an overall C^1 -continuous discretization with $n_{\text{CP}} = 4096$ control points are used as a reference solution.²⁰ The used penalty parameter ε_ϕ is equal to the one proposed in Eq. (88).

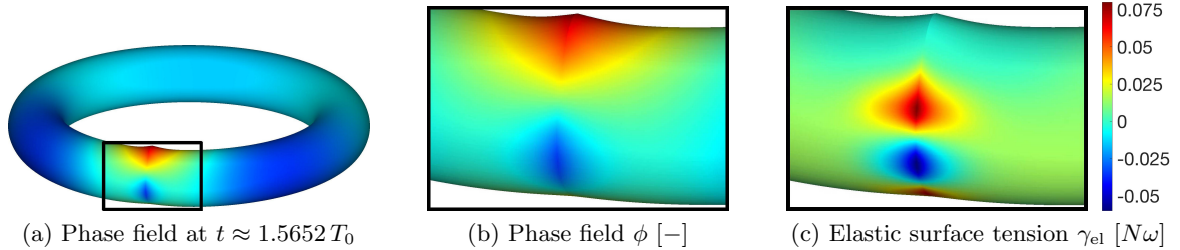


Figure 13: Pressurized torus: (a) Phase field at early times when no constraints are enforced; Enlargement of (b) phase field and (c) elastic surface tension. The insufficient discretization leads to the formation of kinks, non-physical phase separation and stress peaks.

is shown, where $N_{\text{el}}^{\alpha\beta}$ denotes the elastic Cauchy stress components (Sauer and Duong, 2017). The wrong result at early times leads to a different final state. Thus, the relative error of the Cahn-Hilliard energy is much higher for the unconstrained problem, see Fig. 12.

6.2.2 Phase separation on a deforming sphere

This section investigates phase separation on a spherical shell. It is either discretized by six patches, see Fig. 14a, or by unstructured cubic splines, see Fig. 14b. The latter serves as reference as it provides C^2 -continuity everywhere except for eight so-called extraordinary points, where only C^1 -continuity is maintained (Toshniwal et al., 2017). A comparison between the two discretizations is provided in Appendix C. Further constructions of multi-patch sphere discretizations with conforming or non-conforming meshes can be found in Dedoncker et al. (2018).

First, this section investigates the phase field evolution on a sphere for the interface parameter $\ell = \sqrt{0.001} L_0$. The initial radius of the sphere is L_0 and the constant pressure $p = 0.04 E_0 L_0^{-1}$ is applied to its interior surface. The mobility constant is $D = 2.5 T_0$. Fig. 15 shows several snapshots for the phase separation for the six-patch discretization with $m = 64$ in the first row, and the unstructured spline discretization with $r = 3$ in the second row. Both show excellent agreement in space and time. Due to the small interface parameter, multiple red phase nuclei

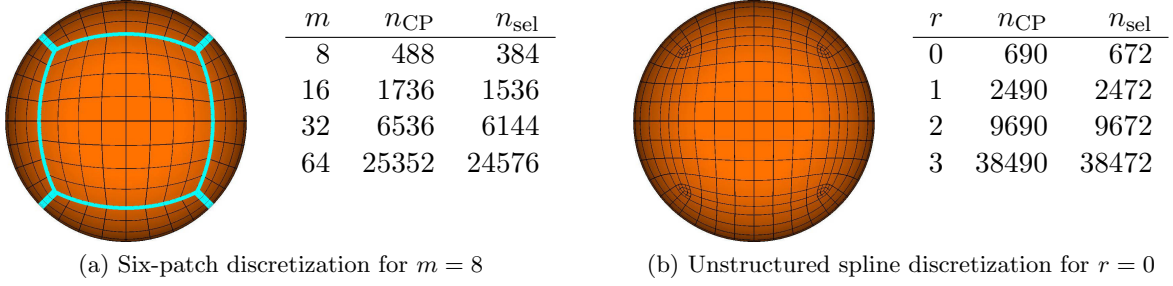


Figure 14: Spline discretizations of a sphere and corresponding mesh properties for different refinement levels for (a) the six-patch discretization (the bold cyan-colored lines mark the patch interfaces) and (b) an unstructured spline discretization. A comparison between the two discretizations can be found in Appendix C.

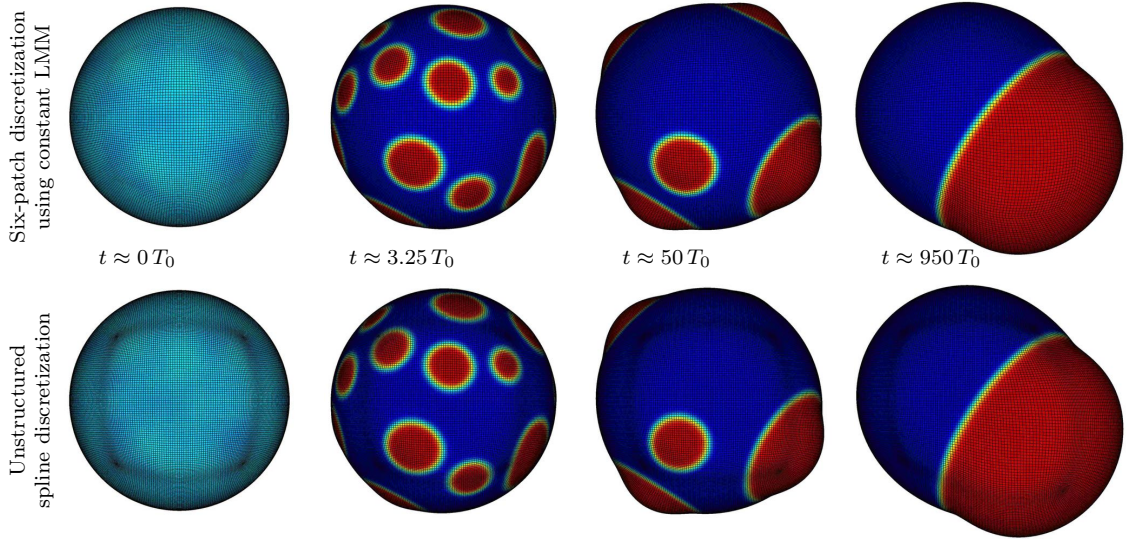


Figure 15: Phase separation on a deforming sphere: The top row shows the phase evolution for the six-patch discretization, the bottom row for the unstructured spline discretization. The constraints for the first one are enforced by the Lagrange multiplier method with constant interpolation. Both cases show excellent agreement.

appear. As the time progresses, these bulge, merge and evolve. The deformation is larger at locations where the nuclei grow. In Fig. 16, the elastic and viscous surface tensions are shown for the two different discretization techniques. The viscous surface tension γ_{visc} follows in analogy to Eq. (97) from the viscous Cauchy stress. The largest values of the elastic surface tension are obtained around the evolving bulges, while the smallest are in their center. Viscous effects are comparatively large at disappearing and around growing bulges. Again, both discretization techniques show excellent agreement.

Second, the results from the two discretization approaches are compared for the same pressure loading but the initial concentration field

$$\phi(\xi^\alpha, 0) = \begin{cases} 1/2, & z \geq 0 \\ 1/6, & z < 0 \end{cases}. \quad (98)$$

The interface parameter is now set to $\ell = \sqrt{0.05} L_0$. The final deformation and phase distribution is visualized on the inset of Fig. 17. Next to it, the black dotted line shows the phase

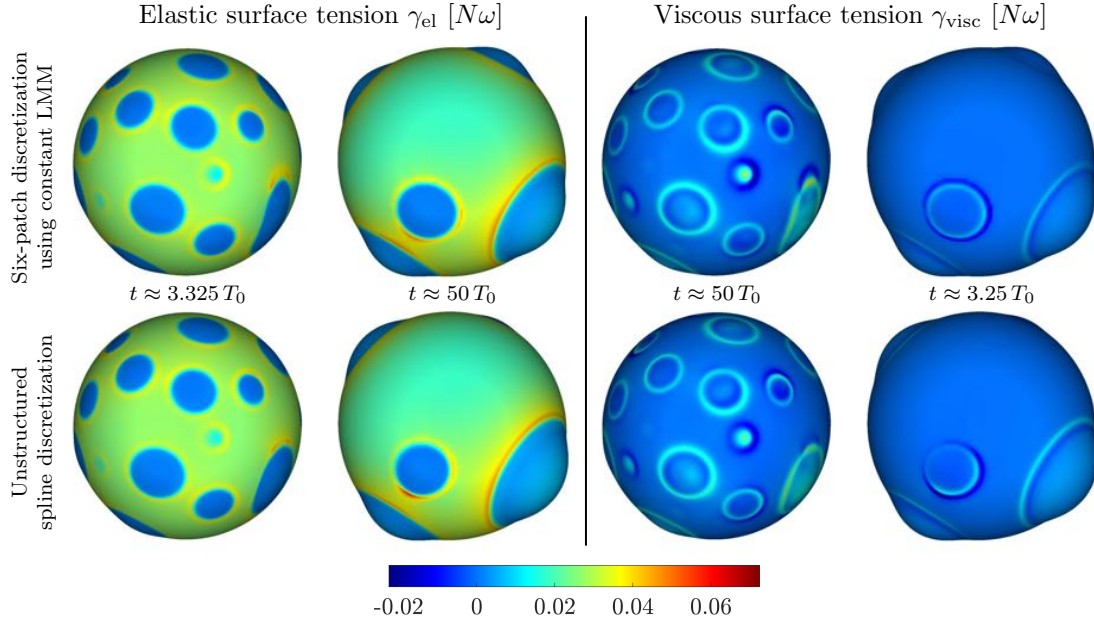


Figure 16: Phase separation on a deforming sphere: The top row shows the elastic and viscous surface tensions for the six-patch discretization, the bottom row for the unstructured spline discretization. The constraints for the first one are enforced by the Lagrange multiplier method with constant interpolation. Both cases show excellent agreement.

field value over the height-coordinate of the illustrated cutting plane for the unstructured spline discretization with $r = 0$ (see Fig. 14b). Further, the elastic surface tension for different refinement levels m and r (see Fig. 14) is illustrated in Fig. 17. For an increasing number of control

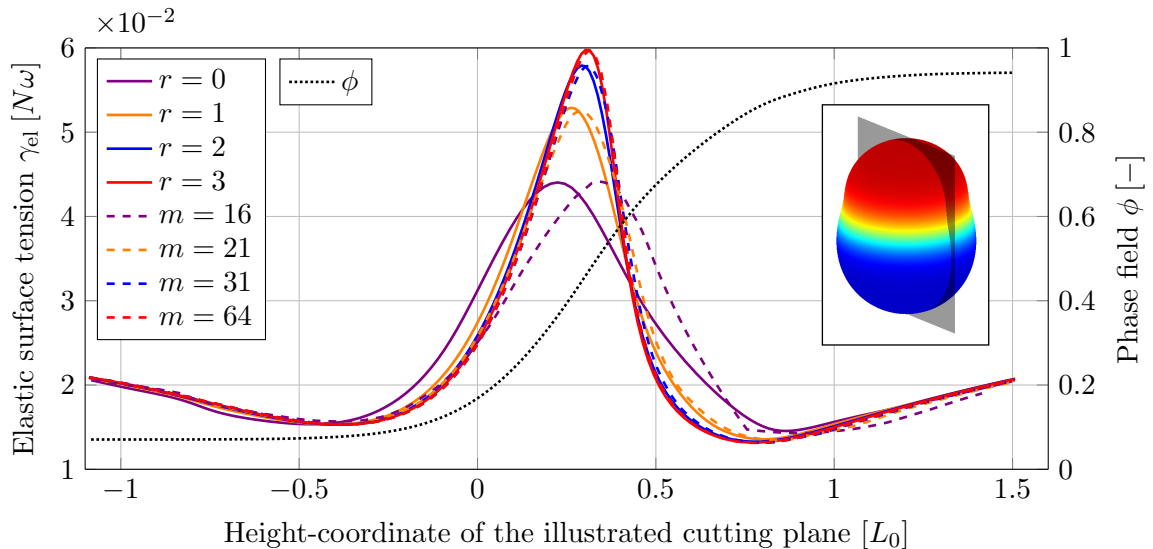


Figure 17: Phase separation on a deforming sphere: Final deformation and phase distribution for the initial state in Eq. (98). Surface tension (left axis) and phase field (right axis) over the height-coordinate. The former is shown for the different discretizations (dashed line: six-patch discretization; solid line: unstructured spline discretization). The results of the two discretization techniques converge for an increasing number of control

points, the results from the six-patch discretization and the unstructured spline discretization converge. This shows that the proposed patch constraints successfully enforce continuity for

the coupled problem.

6.3 Fracture of deforming shells

This section illustrates the modeling of crack evolution on multi-patch shells with the constraints from Sec. 5. Note that the gradients of ϕ are now defined in the reference configuration and the constraint from Eq. (78) is considered. The following material parameters are used throughout this section (see Eqs. (16)–(17))

$$K = \frac{E\nu}{(1+\nu)(1-2\nu)}, \quad G = \frac{E}{2(1+\nu)}, \quad c = 0.1 E_0 L_0^2, \quad (99)$$

with 2D Young’s modulus E and Poisson’s ratio ν . All quantities in this section are non-dimensionalized by the introduction of a reference length L_0 , time T_0 and density ρ_0 . From this, the reference modulus $E_0 := \rho_0 L_0^2 T_0^{-2}$ with units [N/m] follows (Paul et al., 2020). The color coding for the fracture field ranges from the fully fractured state ($\phi = 0$, red color) to the undamaged state ($\phi = 1$, blue color), see Fig. 1b. The lines of reduced continuity are again referred to as C^0 -lines. The present brittle fracture model does not incorporate viscosity, such that $\eta = 0$ in Eq. (19.1).

6.3.1 Verification of the continuity constraint on the fracture field

This section verifies the constraint from Eq. (78) in a two-dimensional setup without mechanical loading. The flat sheet shown in Fig. 18a is considered. The length scale parameter is $\ell_0 = 0.008 L_0$ and the fracture toughness is $\mathcal{G}_c = 0.0005 E_0 L_0$. The used LR mesh (Dokken et al., 2013; Zimmermann and Sauer, 2017) is shown in Fig. 18b. The three C^0 -lines are inserted by knot insertion. The crack in Fig. 18a is computed by manually imposing values for the history field, see Eq. (35), and solving the phase field equation.

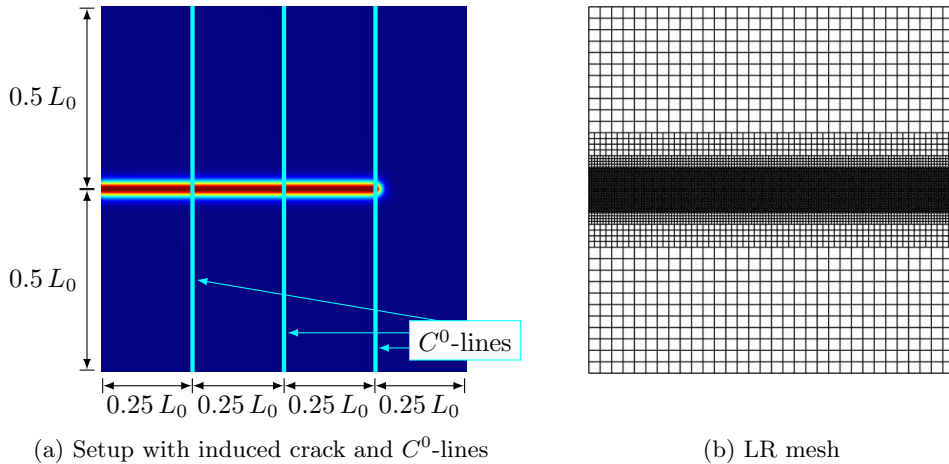


Figure 18: Verification of the continuity constraint on the fracture field. (a) Setup showing the induced initial crack and three C^0 -lines treated with the Lagrange multiplier method using linear interpolation. (b) LR mesh used for all computations.

Fig. 19a illustrates the absolute value of the constraint g_{∇} along the third C^0 -line (at $x = 0.75 L_0$) over the y -position using the penalty method. It shows the two cases when the scaling

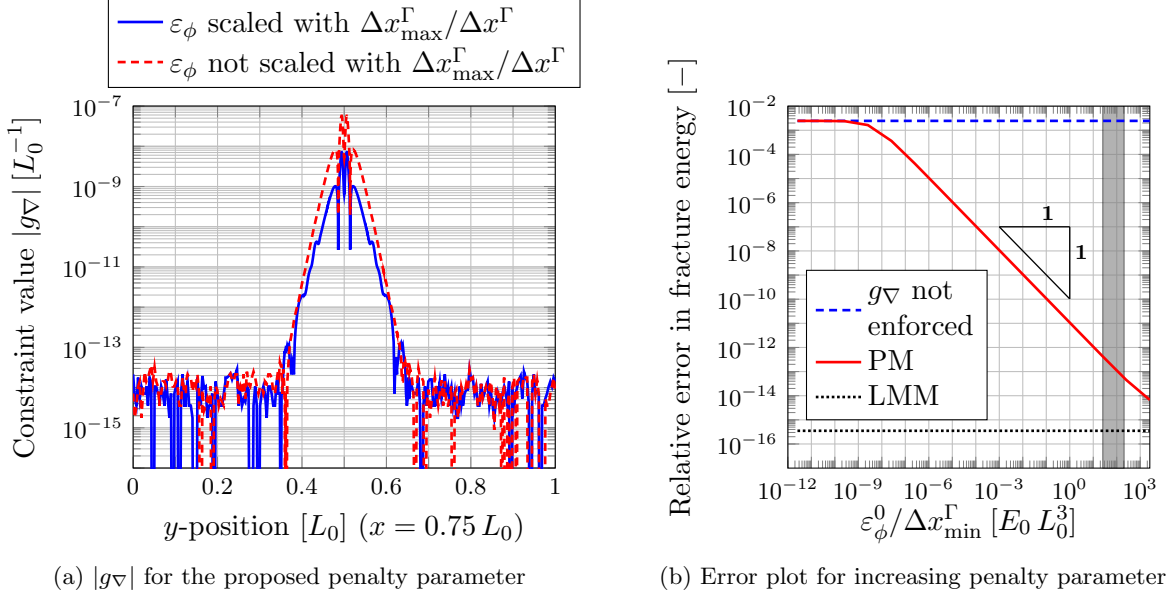


Figure 19: Verification of the continuity constraint on the fracture field. (a) The absolute value of the phase field constraint along the third C^0 -line (at $x = 0.75 L_0$) for the penalty parameter ϵ_ϕ according to Eq. (89). (b) Relative error in the fracture energy for different enforcement techniques and increasing penalty parameter. The gray marked area shows the range of the proposed penalty parameter according to Eq. (89).

of the penalty parameter with $\Delta x_{\max}^\Gamma / \Delta x^\Gamma$ is used or not, see Eq. (89). For both cases, the maximum values are obtained at the center where the crack is located, but the scaling factor reduces the constraint value by one order of magnitude. Thus, the constraint is fulfilled more accurately in regions of fracture, which are the regions of primary interest. The Lagrange multiplier method with constant or linear interpolation leads to values of order 10^{-12} for $|g_\nabla|$. Fig. 19b shows the relative error in the fracture energy for an increasing penalty parameter. The fracture energy of the sheet without manually inserted C^0 -lines is taken as a reference solution. As the penalty parameter increases, the relative error decreases approximately linear until it is close to machine precision. Non-convergence is encountered for $\epsilon_\phi^0 / \Delta x_{\min}^\Gamma \geq 10^4 E_0 L_0^3$ due to ill-conditioning. The gray marked area reflects the range of the proposed penalty parameter from Eq. (89) when the scaling factor $\Delta x_{\max}^\Gamma / \Delta x^\Gamma$ is used. Its largest values are obtained at regions of the highest resolved mesh. It ensures sufficiently accurate results while providing good convergence of the Newton-Raphson scheme. Machine precision is directly reached when the Lagrange multiplier method is used. The blue dashed line marks the error when no constraints are enforced. In this case, the insufficient discretization yields comparatively high errors that can have a huge influence on the solution as loads are applied. Note that also computations with two and four refinement levels and length scale parameters of $\ell_0 = 0.02 L_0$ and $\ell_0 = 0.004 L_0$, respectively, were performed. The results are similar to the ones shown in Fig. 19b.

6.3.2 Fracturing sphere

This section investigates crack evolution on a spherical shell with radius L_0 . Two initial cracks with perpendicular orientation are placed on two opposite sides of the sphere, as shown in Fig. 20. The sphere is subjected to the internal pressure p .²¹ Fig. 20 also shows the positions of the patch interfaces. The parameters $m \in \{32, 64\}$ are used for the six-patch discretization (see

²¹Note that here, the pressure is not depending on the phase field as in Paul et al. (2020).

Fig. 14a), and the parameters $r \in \{2, 3\}$ are used for the unstructured spline discretization (see Fig. 14b). In this section, a constant penalty parameter ε_ϕ , which does not depend on mesh or time step sizes, is used. The material parameters are listed in Table 4. The parameter ℓ_0 is chosen in a way, such that the interface is properly resolved for both kind of discretizations. For the coarse mesh ($m = 32$, $r = 2$), it is set to $0.05 L_0$, whereas it is set to $0.03 L_0$ for the fine mesh ($m = 64$, $r = 3$).

Table 4: Fracturing sphere: Material parameters and imposed internal pressure.

$E [E_0]$	$\nu [-]$	$\mathcal{G}_c [E_0 L_0]$	$T [L_0]$	$p [E_0 L_0^{-1}]$
10	0.3	0.0005	0.0125	0.1

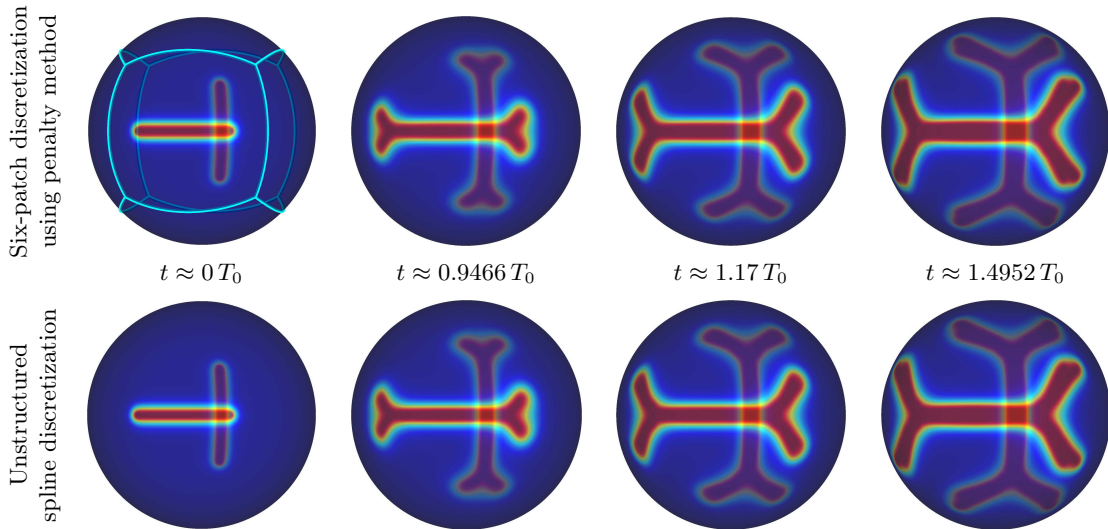


Figure 20: Fracturing sphere: Crack evolution for $\ell_0 = 0.03 L_0$ using the six-patch discretization ($m = 64$) and the penalty method with penalty parameters $\varepsilon_\phi = 1000 E_0 L_0^3$ and $\varepsilon_n = 1000 E_0 L_0$ in the top row, and the unstructured spline discretization ($r = 3$) in the bottom row. Both cases show excellent agreement. The spheres are visualized transparently.

The evolution of the crack is illustrated in Fig. 20. At first, the cracks propagate along their initial direction, but then start branching. In the process, they cross several patch interfaces. For the remainder of this section, the coarse meshes ($m = 32$, $r = 2$) and the larger length scale parameter $\ell_0 = 0.05 L_0$ are used.

Fig. 21 shows the phase field value and surface tension (see Eq. (97)) over the height-coordinate of the illustrated cutting planes. The curves for the Lagrange multiplier method with linear interpolation and the reference solution based on the unstructured spline discretization show good agreement. The solid line in both figures shows the profile in case one of the constraints is neglected. If the phase field constraint is neglected, a kink will appear in ϕ at position $\approx -0.65 L_0$, as the figure shows. This is further illustrated in Fig. 23b. These kinks are avoided if the constraint is fulfilled. Further inaccuracies for γ can be observed at $\approx \{-0.93, -0.65, 0.2, 0.65, 0.94\} L_0$.

Fig. 22 illustrates the phase field and surface tension over the height-coordinate of the same cutting plane, but now, the constraints are enforced by the penalty method. As the penalty

²²Note that the time steps for the shown profiles and snapshots slightly differ due to the adaptive time stepping scheme.

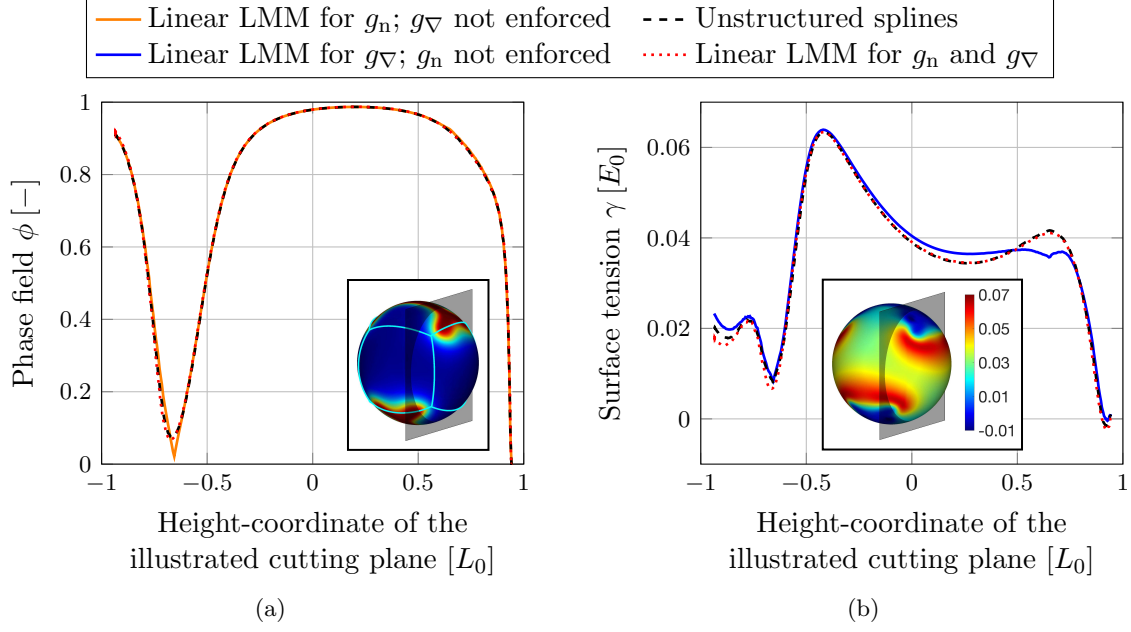


Figure 21: Fracturing sphere: (a) Phase field value and (b) surface tension along the height-coordinate of the illustrated cutting plane at $t \approx 1.13 T_0$ using the Lagrange multiplier method.²² Neglecting one constraint leads to significant offsets in the corresponding curves.

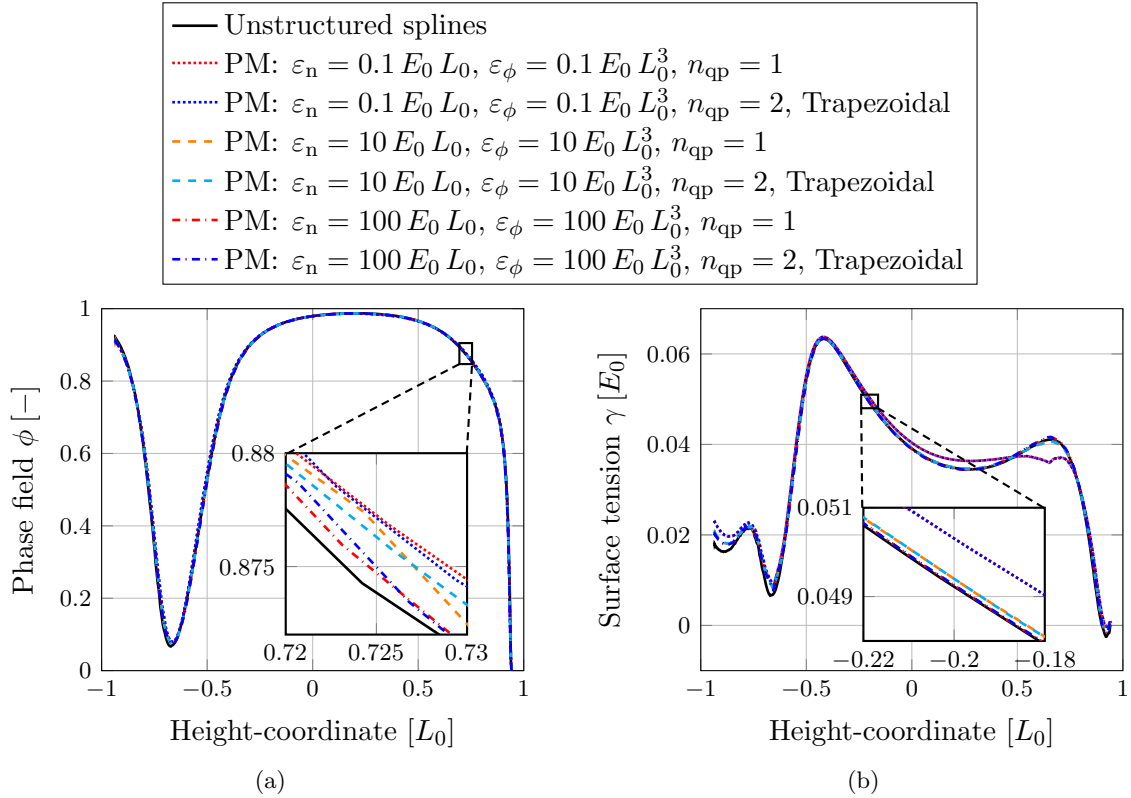


Figure 22: Fracturing sphere: (a) Phase field value and (b) surface tension along the height-coordinate of the cutting plane from Fig. 21 at $t \approx 1.13 T_0$ using the penalty method.²² The penalty parameters and the quadrature rule are varied. As the penalty parameters are increased, good agreement with the reference solution is obtained.

parameters increases, good agreement with the reference solution is obtained. There are no significant differences between the results from the midpoint or trapezoidal rule (note that the quadrature points for these quadrature rules coincide with the locations of the constant or linear Lagrange multipliers, respectively, see Fig. 2). Note that Gaussian quadrature with two or more quadrature points leads to overconstraining of the solution. The constraints cannot be appropriately satisfied at too many locations and thus, the fracture field shows unphysical behavior, see Fig. 23c.

The effect on the phase field and surface tension, when either g_∇ or g_n are ignored, are illustrated in Figs. 23–24. If the phase field is underconstrained, it will be discontinuous at the interface,

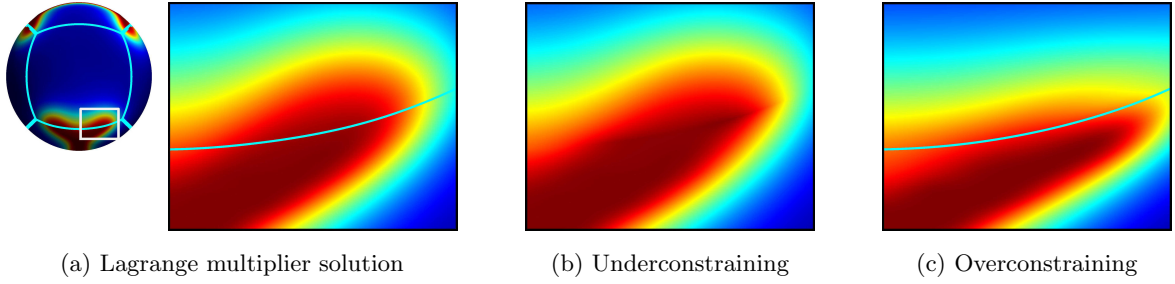


Figure 23: Fracturing sphere: (a) Phase field at $t \approx 1.13 T_0$ for the Lagrange multiplier method with linear interpolation ($n_{\text{qp}} = 2$, Gaussian quadrature). The enlargement is shown next to it. (b) The effect of a too small penalty parameter ($\varepsilon_\phi = 0$, $\varepsilon_n = 100 E_0 L_0$, $n_{\text{qp}} = 2$, Trapezoidal) on the phase field (the patch line is omitted for better visualization). (c) The effect of overconstraining the penalty method ($\varepsilon_\phi = 100 E_0 L_0^3$, $\varepsilon_n = 100 E_0 L_0$) using $n_{\text{qp}} = 3$ Gaussian quadrature points.

see Fig. 23b. The choice of an inappropriate quadrature rule for the penalty method leads to overconstraining of the solution and an unphysical deflection of the phase field at the patch interfaces will occur, see Fig. 23c. Finally, the effect of an insufficient enforcement of the G^1 -

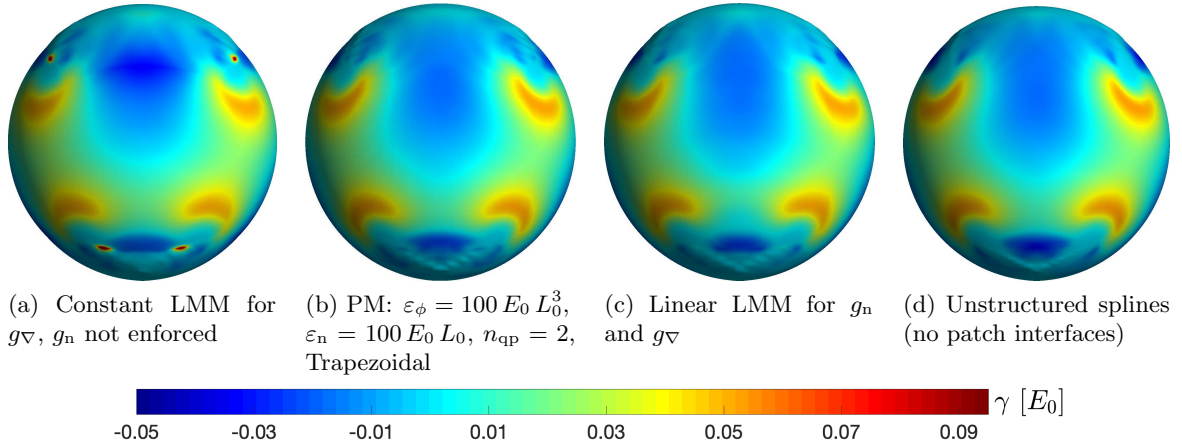


Figure 24: Fracturing sphere: Surface tension at $t \approx 1.3263 T_0$ for different patch constraint enforcement techniques.²²

continuity constraint is shown in Fig. 24. If this constraint is not appropriately fulfilled, stress peaks will appear at the patch interfaces, see Fig. 24a. Figs. 24b–24c show the surface tension for different enforcement techniques in comparison to the fully C^1 -continuous discretization in

Fig. 24d at $t \approx 1.3263 T_0$. Again, the results from the different discretization techniques show excellent agreement.

6.3.3 Crack propagation across kinks

This section focuses on the general constraints for non-smooth patch connections. The initial setup with an existing initial crack is shown in Fig. 25–26a. The mesh is locally refined a priori based on the expected crack path, see Fig. 26b. The refinement depth is $d = 3$ (Paul et al., 2020). The material parameters are listed in Table 5. A displacement is applied as shown

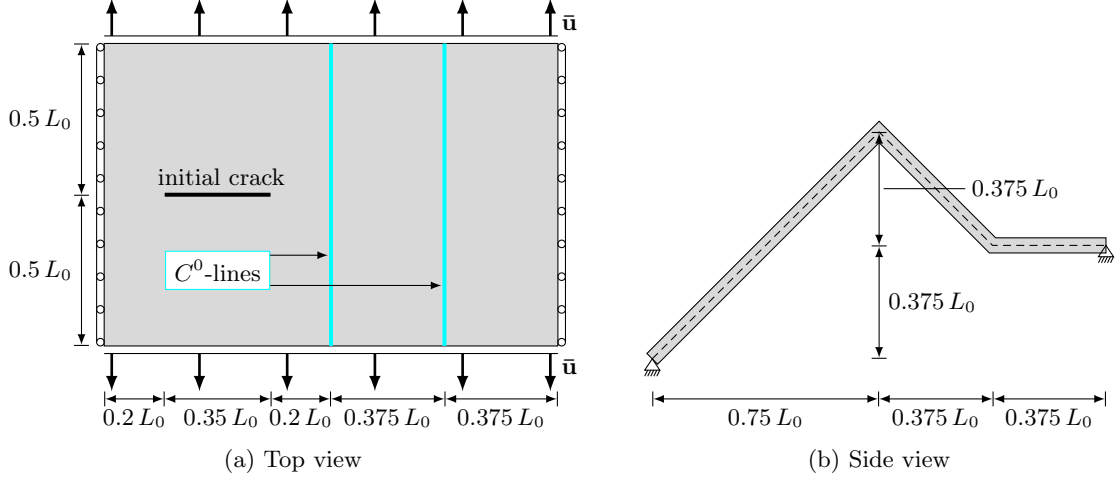


Figure 25: Crack propagation across kinks: Geometry with initial crack. The two C^0 -lines are marked by bold cyan-colored lines.

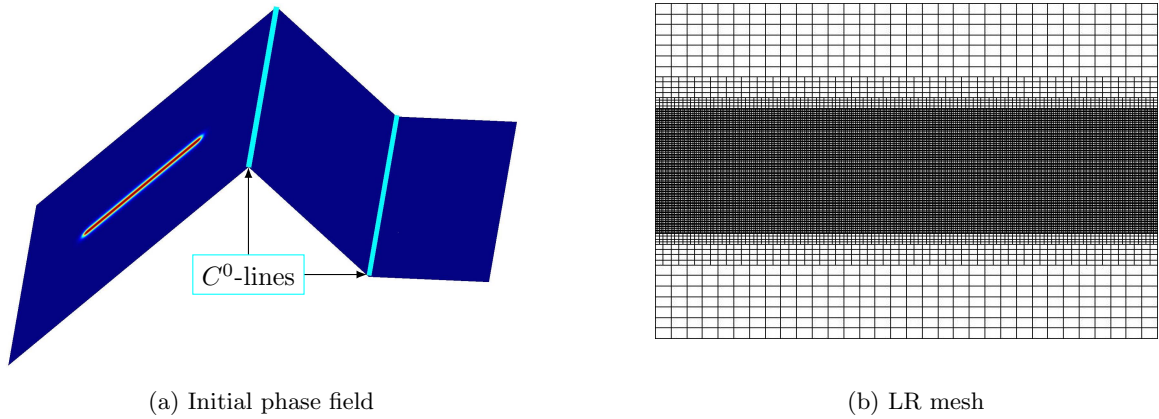


Figure 26: Crack propagation across kinks: (a) Initial phase field and (b) LR mesh that is locally refined a priori based on the expected crack path.

in Fig. 25a. At each time step, the displacement increment $\Delta \bar{u} = \bar{v} \Delta t$ is imposed to obtain a constant loading velocity \bar{v} . The crack evolution is illustrated in Fig. 27 for four different time steps. The crack starts propagating in both directions. While one end reaches the end of the sheet on the left, the right end of the crack propagates across the kinks. Crack branching occurs shortly before the crack reaches the second kink. A very similar fracture pattern is observed when the two surface kinks are smoothed and a fully C^1 -continuous parametrization is used.

Table 5: Crack propagation across kinks: Material parameters and loading velocity \bar{v} .

$E [E_0]$	$\nu [-]$	$\mathcal{G}_c [E_0 L_0]$	$\ell_0 [L_0]$	$T [L_0]$	$\bar{v} [L_0 T_0^{-1}]$
100	0.3	0.0005	0.008	0.0125	0.004

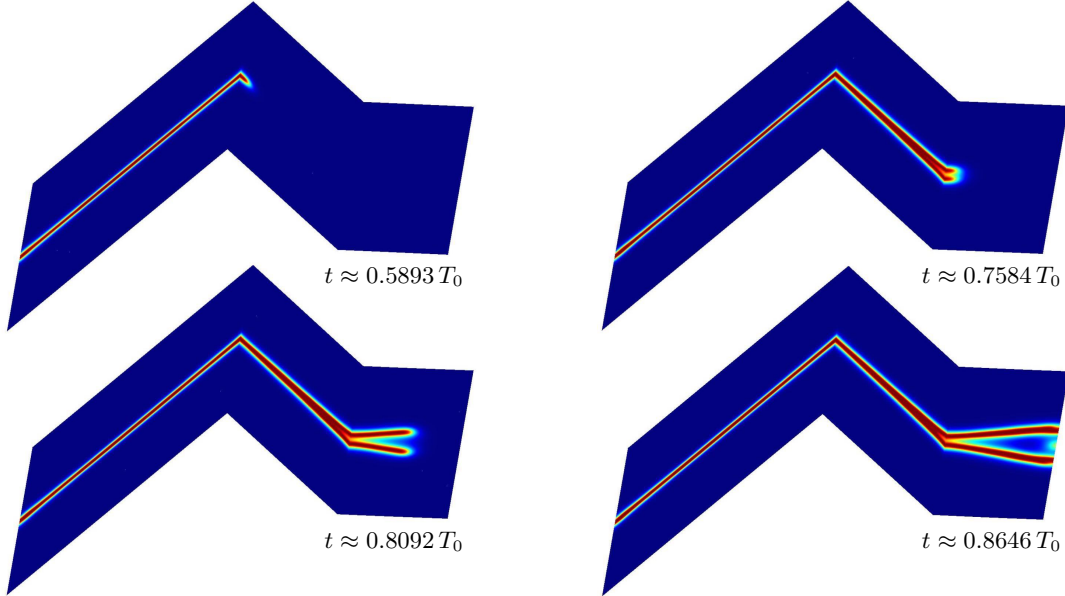


Figure 27: Crack propagation across kinks: Crack evolution where both constraints are fulfilled via the Lagrange multiplier method with constant interpolation.

If the phase field constraint is neglected, the phase field will smear at the two kinks and will slightly evolve along them, similar as in Fig. 23b. It can be concluded that crack evolution including branching works well in the proposed framework.

6.4 Evaluation of the constraint enforcement techniques

This section briefly discusses and compares the proposed enforcement techniques. For pure shells, no significant differences between constant and linear interpolation of the Lagrange multiplier were found (using bi-quadratic NURBS for the surface representation). While requiring more implementation effort than the penalty method, the Lagrange multiplier method with element-wise constant interpolation is the safest choice, as it guarantees a stable and well conditioned system. The penalty method on the other hand is easier to implement but requires a careful choice of the penalty parameter.

Fig. 28 shows the average condition number of the stiffness matrix and the average number of required Newton-Raphson iterations for the fracturing sphere example, see Figs. 21–24, over the penalty parameter ε_ϕ . The black dotted line marks the size of the proposed penalty parameter from Eq. (89) ($\varepsilon_\phi^0 / \Delta x_{\min}^\Gamma$). Fig. 28a shows that the average condition number is smaller when only one quadrature point is used for the integration along the element-wise patch interfaces. The proposed penalty parameter ensures that the condition number does not increase too much. Fig. 28b shows that the Lagrange multiplier method performs better with respect to the required number of Newton-Raphson iterations. However, the difference is minor for *moderate* values of the penalty parameter, especially for the proposed penalty parameter from Eq. (89). As

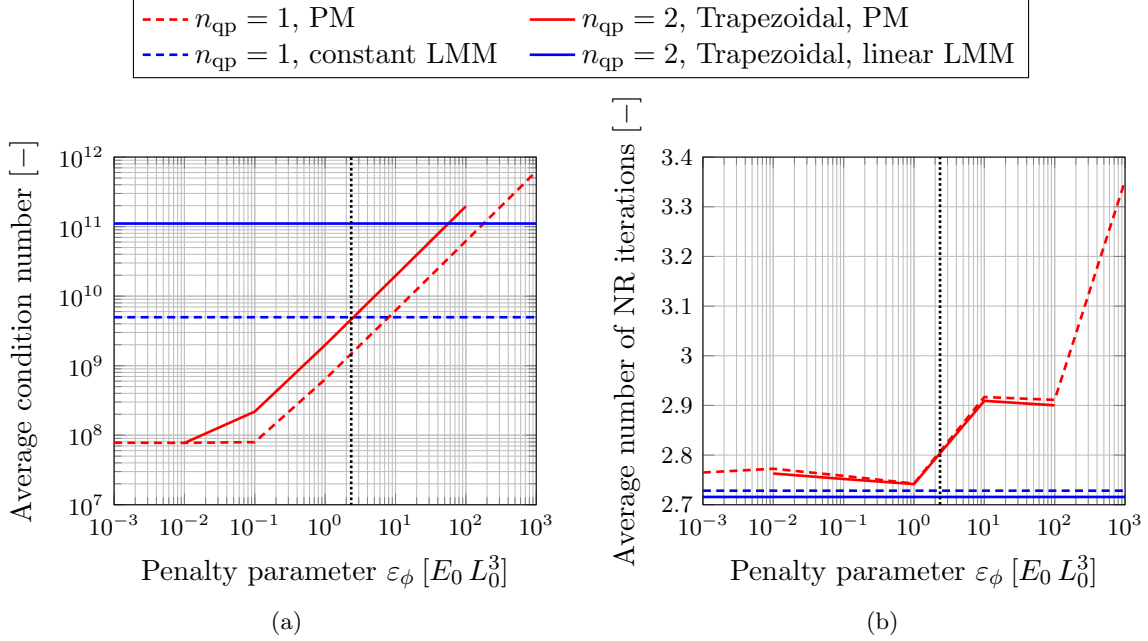


Figure 28: Comparison of the constraint enforcement techniques: (a) Average condition number and (b) average number of Newton-Raphson iterations for the fracturing sphere example, see Figs. 21–24. The black dotted line indicates the proposed penalty parameter from Eq. (89).

there is no noticeable difference between the results for constant and linear interpolation of the Lagrange multiplier, the authors conclude to use a constant interpolation for the coupled framework of fracture of thin shells. Further, for this case, there are no significant differences between the penalty and the Lagrange multiplier method with respect to performance (based on the data in Fig. 28).

7 Conclusion

This work proposes continuity constraints for coupled fourth-order deformation and phase field models defined on isogeometric multi-patch shells. The higher continuity that stems from IGA is not automatically preserved at the patch interfaces and thus, the G^1 - and C^1 -continuity is recovered by enforcing patch constraints with a penalty or Lagrange multiplier approach. The interfaces between the patches are assumed to be conforming with respect to the discretization, but allow for non-smooth connections, for example to model kinks in the geometry. The constraints are fully formulated in the convective coordinate system that arises from the surface description and are thus, applicable to the majority of shell formulations.

In Sec. 6, the purely mechanical shell framework and the coupled one of phase fields on deforming surfaces are investigated. The first is used within a quasi-static framework to study the accuracy of the G^1 -continuity constraint on multi-patch discretizations. The proposed enforcement techniques perform well in terms of convergence rates and absolute errors. The coupled framework includes phase transitions, which are based on the Cahn-Hilliard equation, on deforming surfaces, and brittle fracture of thin shells, which is based on a higher-order phase field approach. The results for both phase field models highlight the importance of the C^1 -continuity constraint. Comparison with fully C^1 -continuous discretizations demonstrate the correct functioning of the proposed constraints and enforcement techniques. The examples include crack propagation across kinks showing the capability of the proposed formulation to handle non-

smooth patch connections. An insufficient enforcement of the inter-patch continuity can lead to spurious stress peaks at patch interfaces. On the other hand, overconstraining can occur for the penalty method if the wrong quadrature rule is used. In this case, the phase field will deflect at patch interfaces instead of crossing it. This problem can be circumvented by using midpoint or trapezoidal quadrature. The investigations on the penalty parameter demonstrate that the proposed problem-independent penalty parameter of Eq. (89) is a suitable choice.

Possible extensions to this work include the coupling of the G^1 - and C^1 -continuity constraints with each other. For example in fracture, the G^1 -continuity may be lost in fully fractured regions. The enforcement techniques may also be extended to handle non-conforming meshes, e.g. by a modified penalty or mortar method (see Sec. 1). An extension to the coupling of trimmed or unstructured splines may be of interest, especially for geometries that are created by CAD software. The present work focuses on solid materials. Liquid shells, such as lipid bilayers, that can also be described by the present shell formulation (Sauer et al., 2017), are another extension. Further, the linearization of the constraint terms can in principle be used in the framework of linear Kirchhoff-Love shells to maintain a fully linear FE formulation.

Acknowledgments

The authors acknowledge funding by the Deutsche Forschungsgemeinschaft (DFG, German Research Foundation) – projects GSC 111 (Graduate School AICES) and 33849990/GRK2379 (IRTG Modern Inverse Problems). Simulations in Sec. 6.3 were performed with computing resources granted by RWTH Aachen University under project rwth0433. The authors also thank Deepesh Toshniwal for providing the unstructured spline discretization used in Sec. 6.

Appendix

A Bending moments at patch interfaces

This section derives the bending moments that are transmitted across patch interfaces for the penalty and Lagrange multiplier method. The external virtual work associated with moments is given by (Sauer and Duong, 2017)

$$\delta\Pi_{\text{ext}} = \int_{\partial\mathcal{S}} \delta\mathbf{n} \cdot \mathbf{M} \, ds, \quad (100)$$

with distributed moment vector \mathbf{M} on a cut normal to $\boldsymbol{\nu}$. The moment vector that physically acts on the element is then given by

$$\mathbf{m} := \mathbf{n} \times \mathbf{M}, \quad (101)$$

which can be decomposed into $\mathbf{m} = m_\nu \boldsymbol{\nu} + m_\tau \boldsymbol{\tau}$. In the following, the bending moments m_τ and $m_{\bar{\tau}}$ at the patch interfaces are derived by comparing the negative virtual work $-\delta\Pi_n$ with $\delta\Pi_{\text{ext}}$. Note that in the weak form, $\delta\Pi_{\text{ext}}$ enters with a negative sign, but $\delta\Pi_n$ enters with a positive sign. Thus, $\delta\Pi_{\text{ext}}$ needs to be compared with $-\delta\Pi_n$ and not with $+\delta\Pi_n$.²³

²³Note that the subsequent derivations of the bending moments have been changed compared to the journal version.

Based on Eqs. (48), (53) and (55) the following relations can be obtained

$$(\mathbf{n} \times \tilde{\mathbf{n}}) \cdot \boldsymbol{\tau} = \sin \alpha, \quad \text{and} \quad (\mathbf{n} \times \tilde{\boldsymbol{\nu}}) \cdot \boldsymbol{\tau} = -\cos \alpha, \quad \text{and} \quad (\tilde{\mathbf{n}} \times \boldsymbol{\nu}) \cdot \boldsymbol{\tau} = \cos \alpha, \quad (102)$$

which are used in the subsequent sections.

A.1 Penalty method

Based on Eq. (63), the distributed moment vectors are given by

$$\mathbf{M} = \varepsilon_n \tilde{\mathbf{d}} = \varepsilon_n (c_0 \tilde{\mathbf{n}} + s_0 \tilde{\boldsymbol{\nu}}), \quad \text{and} \quad \tilde{\mathbf{M}} = \varepsilon_n \mathbf{d} = \varepsilon_n (c_0 \mathbf{n} + s_0 \boldsymbol{\nu}). \quad (103)$$

The bending moment m_τ at element Ω^e , which is transmitted across the patch interface, is then given by

$$\begin{aligned} m_\tau &= \mathbf{m} \cdot \boldsymbol{\tau} = (\mathbf{n} \times \mathbf{M}) \cdot \boldsymbol{\tau} = \varepsilon_n \left[c_0 (\mathbf{n} \times \tilde{\mathbf{n}}) \cdot \boldsymbol{\tau} + s_0 (\mathbf{n} \times \tilde{\boldsymbol{\nu}}) \cdot \boldsymbol{\tau} \right] \\ &= \varepsilon_n (c_0 \sin \alpha - s_0 \cos \alpha) = \varepsilon_n \sin(\alpha - \alpha_0). \end{aligned} \quad (104)$$

In analogy, the bending moment $m_{\tilde{\tau}}$ at element $\tilde{\Omega}^e$ is given by

$$m_{\tilde{\tau}} = \tilde{\mathbf{m}} \cdot \tilde{\boldsymbol{\tau}} = -(\tilde{\mathbf{n}} \times \tilde{\mathbf{M}}) \cdot \boldsymbol{\tau} = -\varepsilon_n \left[c_0 (\tilde{\mathbf{n}} \times \mathbf{n}) \cdot \boldsymbol{\tau} + s_0 (\tilde{\mathbf{n}} \times \boldsymbol{\nu}) \cdot \boldsymbol{\tau} \right] = \varepsilon_n \sin(\alpha - \alpha_0). \quad (105)$$

A.2 Lagrange multiplier method

Based on Eq. (71), the distributed moment vectors are given by

$$\begin{aligned} \mathbf{M} &= q \tilde{\mathbf{d}} = q ((s_0 + c_0) \tilde{\mathbf{n}} + (s_0 - c_0) \tilde{\boldsymbol{\nu}}), \\ \tilde{\mathbf{M}} &= q \mathbf{d} = q ((s_0 + c_0) \mathbf{n} + (s_0 - c_0) \boldsymbol{\nu}). \end{aligned} \quad (106)$$

The bending moment m_τ at element Ω^e , which is transmitted across the patch interface, is then given by

$$\begin{aligned} m_\tau &= \mathbf{m} \cdot \boldsymbol{\tau} = (\mathbf{n} \times \mathbf{M}) \cdot \boldsymbol{\tau} = q \left[(s_0 + c_0) (\mathbf{n} \times \tilde{\mathbf{n}}) \cdot \boldsymbol{\tau} + (s_0 - c_0) (\mathbf{n} \times \tilde{\boldsymbol{\nu}}) \cdot \boldsymbol{\tau} \right] \\ &= q ((s_0 + c_0) \sin \alpha - (s_0 - c_0) \cos \alpha) = q (\sin(\alpha - \alpha_0) + \cos(\alpha - \alpha_0)), \end{aligned} \quad (107)$$

which simplifies to $m_\tau = q$ since the constraint $\alpha = \alpha_0$ is fulfilled exactly for the Lagrange multiplier method. Likewise, the bending moment $m_{\tilde{\tau}}$ at element $\tilde{\Omega}^e$ is given by

$$\begin{aligned} m_{\tilde{\tau}} &= \tilde{\mathbf{m}} \cdot \tilde{\boldsymbol{\tau}} = -(\tilde{\mathbf{n}} \times \tilde{\mathbf{M}}) \cdot \boldsymbol{\tau} = q \left[-(s_0 + c_0) (\tilde{\mathbf{n}} \times \mathbf{n}) \cdot \boldsymbol{\tau} - (s_0 - c_0) (\tilde{\mathbf{n}} \times \boldsymbol{\nu}) \cdot \boldsymbol{\tau} \right] \\ &= q ((s_0 + c_0) \sin \alpha - (s_0 - c_0) \cos \alpha) = q (\sin(\alpha - \alpha_0) + \cos(\alpha - \alpha_0)), \end{aligned} \quad (108)$$

which also simplifies to $m_{\tilde{\tau}} = q$.

B Variation and linearization

This section reports and derives several variations, which are required in Sec. 5, and the linearization of the force vectors stemming from the continuity constraints in Sec. 5. Some auxiliary variations and linearized quantities are derived in Appendix B.1. The linearization of the force vectors for the G^1 -continuity constraints is reported in Sec. B.2, and for the C^1 -continuity constraints in Sec. B.3. In both cases, the penalty and Lagrange multiplier methods are considered. The linearization is reported for the most general expression of the force vectors. The linearization for the fracture model will significantly simplify, since the corresponding force vectors do not depend on \mathbf{x} or $\tilde{\mathbf{x}}$, but only on \mathbf{X} and $\tilde{\mathbf{X}}$. Thus, the linearization with respect to \mathbf{x} and $\tilde{\mathbf{x}}$ vanishes for the brittle fracture model. Additionally, the simplification $\tilde{\boldsymbol{\nu}} = -\boldsymbol{\nu}$ and $\alpha = \alpha_0$ can be inserted for smooth patch connections. Here, the G^1 -continuity constraint is not depending on any of the phase fields, so that the corresponding force vectors do not require any linearization with respect to ϕ or $\tilde{\phi}$.

B.1 Variation and linearization of auxiliary quantities

The variation of Eq. (60) requires the variations of the terms $\cos \alpha$ and $\sin \alpha$. They follow from Eqs. (53) and (55) as

$$\delta(\cos \alpha) = \delta(\mathbf{n} \cdot \tilde{\mathbf{n}}) = \delta \mathbf{n} \cdot \tilde{\mathbf{n}} + \mathbf{n} \cdot \delta \tilde{\mathbf{n}}, \quad (109)$$

and

$$\begin{aligned} \delta(\sin \alpha) &= \delta\left((\mathbf{n} \times \tilde{\mathbf{n}}) \cdot \boldsymbol{\tau}\right) = (\delta \mathbf{n} \times \tilde{\mathbf{n}}) \cdot \boldsymbol{\tau} + (\mathbf{n} \times \delta \tilde{\mathbf{n}}) \cdot \boldsymbol{\tau} + (\mathbf{n} \times \tilde{\mathbf{n}}) \cdot \delta \boldsymbol{\tau} \\ &= -(\delta \mathbf{n} \times \tilde{\mathbf{n}}) \cdot \tilde{\boldsymbol{\tau}} - (\delta \tilde{\mathbf{n}} \times \mathbf{n}) \cdot \boldsymbol{\tau} + (\mathbf{n} \times \tilde{\mathbf{n}}) \cdot \delta \boldsymbol{\tau} \\ &= -(\tilde{\mathbf{n}} \times \tilde{\boldsymbol{\tau}}) \cdot \delta \mathbf{n} - (\mathbf{n} \times \boldsymbol{\tau}) \cdot \delta \tilde{\mathbf{n}} + (\mathbf{n} \times \tilde{\mathbf{n}}) \cdot \delta \boldsymbol{\tau} \\ &= \tilde{\boldsymbol{\nu}} \cdot \delta \mathbf{n} + \boldsymbol{\nu} \cdot \delta \tilde{\mathbf{n}} + (\mathbf{n} \times \tilde{\mathbf{n}}) \cdot \delta \boldsymbol{\tau}. \end{aligned} \quad (110)$$

Using Eqs. (109) and (110), the following relations can be derived

$$\begin{aligned} \delta(\cos(\alpha - \alpha_0)) &= \delta(c_0 \cos \alpha + s_0 \sin \alpha) \\ &= c_0(\delta \mathbf{n} \cdot \tilde{\mathbf{n}} + \mathbf{n} \cdot \delta \tilde{\mathbf{n}}) + s_0(\delta \boldsymbol{\tau} \cdot (\mathbf{n} \times \tilde{\mathbf{n}}) + \delta \mathbf{n} \cdot \tilde{\boldsymbol{\nu}} + \delta \tilde{\mathbf{n}} \cdot \boldsymbol{\nu}), \end{aligned} \quad (111)$$

and

$$\begin{aligned} \delta(\sin(\alpha - \alpha_0)) &= \delta(c_0 \sin \alpha - s_0 \cos \alpha) \\ &= c_0(\delta \boldsymbol{\tau} \cdot (\mathbf{n} \times \tilde{\mathbf{n}}) + \delta \mathbf{n} \cdot \tilde{\boldsymbol{\nu}} + \delta \tilde{\mathbf{n}} \cdot \boldsymbol{\nu}) - s_0(\delta \mathbf{n} \cdot \tilde{\mathbf{n}} + \mathbf{n} \cdot \delta \tilde{\mathbf{n}}), \end{aligned} \quad (112)$$

which are required in Sec. 5.1.3. Note that Eqs. (111)–(112) can be simplified using $\mathbf{n} \times \tilde{\mathbf{n}} = \sin(\alpha) \boldsymbol{\tau}$ and $\boldsymbol{\tau} \cdot \delta \boldsymbol{\tau} = 0$, see Eq. (113).

Further variations that are required in Sec. 5.1 are (Sauer, 2014; Duong et al., 2017)

$$\delta \mathbf{n} = -(\mathbf{a}^\alpha \otimes \mathbf{n}) \delta \mathbf{a}_\alpha, \quad \delta \tilde{\mathbf{n}} = -(\tilde{\mathbf{a}}^\alpha \otimes \tilde{\mathbf{n}}) \delta \tilde{\mathbf{a}}_\alpha, \quad \delta \boldsymbol{\tau} = \mathbf{M}^\xi \delta \hat{\mathbf{a}}_\xi, \quad (113)$$

with the variation of $\hat{\mathbf{a}}_\xi$ from Eq. (49) and

$$\mathbf{M}^\xi := \frac{1}{\|\hat{\mathbf{a}}_\xi\|} (\mathbf{1} - \boldsymbol{\tau} \otimes \boldsymbol{\tau}). \quad (114)$$

For the linearization of the force vectors in Sec. 5, further linearizations of surface measures are required, for example (Sauer and Duong, 2017)

$$\begin{aligned}\Delta_x \mathbf{a}^\alpha &= (a^{\alpha\beta} \mathbf{n} \otimes \mathbf{n} - \mathbf{a}^\beta \otimes \mathbf{a}^\alpha) \mathbf{N}_{,\beta} \Delta \mathbf{x}_e, \\ \Delta_x \boldsymbol{\nu} &= -(\boldsymbol{\tau} \otimes \boldsymbol{\nu}) \Delta_x \boldsymbol{\tau} - (\mathbf{n} \otimes \boldsymbol{\nu}) \Delta_x \mathbf{n},\end{aligned}\quad (115)$$

with

$$\begin{aligned}\Delta_x \mathbf{n} &= -\mathbf{a}^\alpha (\mathbf{n} \cdot \Delta_x \mathbf{a}_\alpha) = -(\mathbf{a}^\alpha \otimes \mathbf{n}) \Delta_x \mathbf{a}_\alpha, \\ \Delta_x \boldsymbol{\tau} &= M^\xi \Delta_x \hat{\mathbf{a}}_\xi,\end{aligned}\quad (116)$$

see Eqs. (113)–(114). For simplicity, the following notation is introduced for the quantities above

$$\Delta_x \mathbf{n} := \mathbf{R} \Delta \mathbf{x}_e, \quad \Delta_x \mathbf{a}^\alpha := \mathcal{A}^\alpha \Delta \mathbf{x}_e, \quad \text{and} \quad \Delta_x \boldsymbol{\nu} := \mathbf{V}_1 \Delta \mathbf{x}_e + \mathbf{V}_2 \Delta \hat{\mathbf{x}}_e, \quad (117)$$

with the definitions

$$\begin{aligned}\mathbf{R} &:= -(\mathbf{a}^\alpha \otimes \mathbf{n}) \mathbf{N}_{,\alpha}, \\ \mathcal{A}^\alpha &:= (a^{\alpha\beta} \mathbf{n} \otimes \mathbf{n} - \mathbf{a}^\beta \otimes \mathbf{a}^\alpha) \mathbf{N}_{,\beta}, \\ \mathbf{V}_1 &:= \nu^\alpha (\mathbf{n} \otimes \mathbf{n}) \mathbf{N}_{,\alpha}, \\ \mathbf{V}_2 &:= -(\boldsymbol{\tau} \otimes \boldsymbol{\nu}) M^\xi \hat{\mathbf{N}}_{,\xi}.\end{aligned}\quad (118)$$

Note that the first three quantities in Eq. (118) have dimension $3 \times 3 n_e$, while \mathbf{V}_2 has dimension $3 \times \hat{n}_{\text{CP}}$. Here, n_e denotes the number of control points associated with the surface element Ω^e , and \hat{n}_{CP} denotes the number of control points along the line element Γ^e . The quantity $\Delta \mathbf{x}_e$ has dimension $3 n_e \times 1$, and $\Delta \hat{\mathbf{x}}_e$ has dimension $3 \hat{n}_{\text{CP}} \times 1$ (see Eqs. (49)–(50)). The corresponding auxiliary variables $\tilde{\mathbf{R}}$, $\tilde{\mathcal{A}}^\alpha$, $\tilde{\mathbf{V}}_1$ and $\tilde{\mathbf{V}}_2$ follow in analogy to Eq. (118), i.e.

$$\begin{aligned}\tilde{\mathbf{R}} &:= -(\tilde{\mathbf{a}}^\alpha \otimes \tilde{\mathbf{n}}) \tilde{\mathbf{N}}_{,\alpha}, \\ \tilde{\mathcal{A}}^\alpha &:= (\tilde{a}^{\alpha\beta} \tilde{\mathbf{n}} \otimes \tilde{\mathbf{n}} - \tilde{\mathbf{a}}^\beta \otimes \tilde{\mathbf{a}}^\alpha) \tilde{\mathbf{N}}_{,\beta}, \\ \tilde{\mathbf{V}}_1 &:= \tilde{\nu}^\alpha (\tilde{\mathbf{n}} \otimes \tilde{\mathbf{n}}) \tilde{\mathbf{N}}_{,\alpha}, \\ \tilde{\mathbf{V}}_2 &:= -(\tilde{\boldsymbol{\tau}} \otimes \tilde{\boldsymbol{\nu}}) M^\xi \hat{\tilde{\mathbf{N}}}_{,\xi},\end{aligned}\quad (119)$$

so that $\Delta_{\tilde{\mathbf{x}}} \tilde{\mathbf{n}} := \tilde{\mathbf{R}} \Delta \tilde{\mathbf{x}}_e$, $\Delta_{\tilde{\mathbf{x}}} \tilde{\mathbf{a}}^\alpha := \tilde{\mathcal{A}}^\alpha \Delta \tilde{\mathbf{x}}_e$ and $\Delta_{\tilde{\mathbf{x}}} \tilde{\boldsymbol{\nu}} := \tilde{\mathbf{V}}_1 \Delta \tilde{\mathbf{x}}_e + \tilde{\mathbf{V}}_2 \Delta \hat{\tilde{\mathbf{x}}}_e$. Note that the simplifications $\tilde{\boldsymbol{\tau}} = -\boldsymbol{\tau}$ and $\tilde{s} = -s$ can be inserted, see Fig. 3.

The individual linearizations of the Lagrange multiplier λ (see Sec. 5.2.3) are

$$\Delta_\phi \lambda = 0, \quad \Delta_{\tilde{\phi}} \lambda = 0, \quad \Delta_x \lambda = 0, \quad \Delta_{\tilde{\mathbf{x}}} \lambda = 0, \quad \Delta_\lambda \lambda = \hat{\mathbf{N}}_\lambda \Delta \hat{\boldsymbol{\lambda}}_e, \quad (120)$$

with shape function array $\hat{\mathbf{N}}_\lambda$ of dimension $1 \times n_\lambda$ and corresponding linearized nodal values $\Delta \hat{\boldsymbol{\lambda}}_e$ of size $n_\lambda \times 1$, see Eq. (93). The variable n_λ depends on the order of approximation of the Lagrange multiplier, see Fig. 2. The linearizations of the Lagrange multiplier q (see Sec. 5.1.3) follow in analogy.

Based on Eqs. (117)–(120), the individual linearizations of the C^1 -continuity constraint in Eq. (79) are given by

$$\begin{aligned}\Delta_\phi g_\nabla &= (\mathbf{a}^\alpha \cdot \boldsymbol{\nu}) \bar{\mathbf{N}}_{,\alpha} \Delta \phi_e, \\ \Delta_{\tilde{\phi}} g_\nabla &= (\tilde{\mathbf{a}}^\alpha \cdot \tilde{\boldsymbol{\nu}}) \tilde{\bar{\mathbf{N}}}_{,\alpha} \Delta \tilde{\phi}_e, \\ \Delta_x g_\nabla &= \phi_{,\alpha} \boldsymbol{\nu} \cdot \mathcal{A}^\alpha \Delta \mathbf{x}_e, \\ \Delta_{\tilde{\mathbf{x}}} g_\nabla &= \tilde{\phi}_{,\alpha} \tilde{\boldsymbol{\nu}} \cdot \tilde{\mathcal{A}}^\alpha \Delta \tilde{\mathbf{x}}_e, \\ \Delta_\lambda g_\nabla &= 0, \\ \Delta_{\tilde{\mathbf{x}}} g_\nabla &= \left[\phi_{,\alpha} \mathbf{a}^\alpha \cdot \mathbf{V}_2 + \tilde{\phi}_{,\alpha} \tilde{\mathbf{a}}^\alpha \cdot \tilde{\mathbf{V}}_2 \right] \Delta \hat{\mathbf{x}}_e.\end{aligned}\quad (121)$$

Additionally, the linearization of the terms $(\mathbf{a}^\alpha \cdot \boldsymbol{\nu})$ and $(\tilde{\mathbf{a}}^\alpha \cdot \tilde{\boldsymbol{\nu}})$ will be required, since both appear in the force vectors in Eqs. (87) and (95). The linearizations are given by

$$\begin{aligned}\Delta_\phi(\mathbf{a}^\alpha \cdot \boldsymbol{\nu}) &= 0, & \Delta_{\tilde{\phi}}(\mathbf{a}^\alpha \cdot \boldsymbol{\nu}) &= 0, & \Delta_{\mathbf{x}}(\mathbf{a}^\alpha \cdot \boldsymbol{\nu}) &= \boldsymbol{\nu} \cdot \mathcal{A}^\alpha \Delta \mathbf{x}_e, \\ \Delta_{\tilde{\mathbf{x}}}(\mathbf{a}^\alpha \cdot \boldsymbol{\nu}) &= 0, & \Delta_\lambda(\mathbf{a}^\alpha \cdot \boldsymbol{\nu}) &= 0, & \Delta_{\hat{\mathbf{x}}}(\mathbf{a}^\alpha \cdot \boldsymbol{\nu}) &= \mathbf{a}^\alpha \cdot \mathbf{V}_2 \Delta \hat{\mathbf{x}}_e,\end{aligned}\quad (122)$$

and

$$\begin{aligned}\Delta_\phi(\tilde{\mathbf{a}}^\alpha \cdot \tilde{\boldsymbol{\nu}}) &= 0, & \Delta_{\tilde{\phi}}(\tilde{\mathbf{a}}^\alpha \cdot \tilde{\boldsymbol{\nu}}) &= 0, & \Delta_{\mathbf{x}}(\tilde{\mathbf{a}}^\alpha \cdot \tilde{\boldsymbol{\nu}}) &= 0, & \Delta_\lambda(\tilde{\mathbf{a}}^\alpha \cdot \tilde{\boldsymbol{\nu}}) &= 0, \\ \Delta_{\tilde{\mathbf{x}}}(\tilde{\mathbf{a}}^\alpha \cdot \tilde{\boldsymbol{\nu}}) &= \tilde{\boldsymbol{\nu}} \cdot \tilde{\mathcal{A}}^\alpha \Delta \tilde{\mathbf{x}}_e, & \Delta_{\hat{\mathbf{x}}}(\tilde{\mathbf{a}}^\alpha \cdot \tilde{\boldsymbol{\nu}}) &= \tilde{\mathbf{a}}^\alpha \cdot \tilde{\mathbf{V}}_2 \Delta \hat{\mathbf{x}}_e,\end{aligned}\quad (123)$$

Further, the definitions

$$\mathbf{W}^\alpha := \boldsymbol{\nu} \cdot \mathcal{A}^\alpha = -\nu^\alpha \mathbf{a}^\beta \cdot \mathbf{N}_{,\beta}, \quad \tilde{\mathbf{W}}^\alpha := \tilde{\boldsymbol{\nu}} \cdot \tilde{\mathcal{A}}^\alpha = -\tilde{\nu}^\alpha \tilde{\mathbf{a}}^\beta \cdot \tilde{\mathbf{N}}_{,\beta}, \quad (124)$$

are used to simplify the notation, such that $\Delta_{\mathbf{x}}(\mathbf{a}^\alpha \cdot \boldsymbol{\nu}) = \mathbf{W}^\alpha \Delta \mathbf{x}_e$ and $\Delta_{\tilde{\mathbf{x}}}(\tilde{\mathbf{a}}^\alpha \cdot \tilde{\boldsymbol{\nu}}) = \tilde{\mathbf{W}}^\alpha \Delta \tilde{\mathbf{x}}_e$.

B.2 Linearization for the G^1 -continuity constraint

This section reports the linearization of the force vectors that are used to enforce the G^1 -continuity constraint, see Sec. 5.1.

B.2.1 Penalty method

The force vectors in Eq. (65) do not depend on the phase field. Thus, only their linearization with respect to \mathbf{x} , $\tilde{\mathbf{x}}$ and $\hat{\mathbf{x}}$ is required. They are given by

$$\begin{aligned}\Delta_{\mathbf{x}} \mathbf{f}_n^e &= \int_{\Gamma_0^e} \varepsilon_n \mathbf{N}_{,\alpha}^T \left[\mathbf{n} (\tilde{\mathbf{d}}^T \mathcal{A}^\alpha) + (\tilde{\mathbf{d}} \cdot \mathbf{a}^\alpha) \mathbf{R} \right] dS \Delta \mathbf{x}_e, \\ \Delta_{\tilde{\mathbf{x}}} \mathbf{f}_n^e &= \int_{\Gamma_0^e} \varepsilon_n \mathbf{N}_{,\alpha}^T \mathbf{n} \left[(\mathbf{a}^\alpha)^T (c_0 \tilde{\mathbf{R}} + s_0 \tilde{\mathbf{V}}_1) \right] dS \Delta \tilde{\mathbf{x}}_e, \\ \Delta_{\hat{\mathbf{x}}} \mathbf{f}_n^e &= \int_{\Gamma_0^e} \varepsilon_n \mathbf{N}_{,\alpha}^T s_0 \mathbf{n} (\mathbf{a}^\alpha)^T \tilde{\mathbf{V}}_2 dS \Delta \hat{\mathbf{x}}_e,\end{aligned}\quad (125)$$

and

$$\begin{aligned}\Delta_{\mathbf{x}} \mathbf{f}_n^e &= \int_{\Gamma_0^e} \varepsilon_n \tilde{\mathbf{N}}_{,\alpha}^T \tilde{\mathbf{n}} \left[(\tilde{\mathbf{a}}^\alpha)^T (c_0 \mathbf{R} + s_0 \mathbf{V}_1) \right] dS \Delta \mathbf{x}_e, \\ \Delta_{\tilde{\mathbf{x}}} \mathbf{f}_n^e &= \int_{\Gamma_0^e} \varepsilon_n \tilde{\mathbf{N}}_{,\alpha}^T \left[\tilde{\mathbf{n}} (\mathbf{d}^T \tilde{\mathcal{A}}^\alpha) + (\mathbf{d} \cdot \tilde{\mathbf{a}}^\alpha) \tilde{\mathbf{R}} \right] dS \Delta \tilde{\mathbf{x}}_e, \\ \Delta_{\hat{\mathbf{x}}} \mathbf{f}_n^e &= \int_{\Gamma_0^e} \varepsilon_n \tilde{\mathbf{N}}_{,\alpha}^T s_0 \tilde{\mathbf{n}} (\tilde{\mathbf{a}}^\alpha)^T \mathbf{V}_2 dS \Delta \hat{\mathbf{x}}_e,\end{aligned}\quad (126)$$

with \mathbf{d} and $\tilde{\mathbf{d}}$ given in Eqs. (62.2)–(62.3).

B.2.2 Lagrange multiplier method

The force vectors in Eq. (74) only depend on \mathbf{x} , $\tilde{\mathbf{x}}$ and q . The corresponding linearizations are given by

$$\begin{aligned}\Delta_{\mathbf{x}} \bar{\mathbf{f}}_{\mathbf{n}}^e &= \int_{\Gamma_0^e} q \mathbf{N}_{,\alpha}^T \left[\mathbf{n} (\tilde{\mathbf{d}}^T \mathcal{A}^\alpha) + (\tilde{\mathbf{d}} \cdot \mathbf{a}^\alpha) \mathbf{R} \right] dS \Delta \mathbf{x}_e, \\ \Delta_{\tilde{\mathbf{x}}} \bar{\mathbf{f}}_{\mathbf{n}}^e &= \int_{\Gamma_0^e} q \mathbf{N}_{,\alpha}^T \mathbf{n} \left[(\mathbf{a}^\alpha)^T ((s_0 + c_0) \tilde{\mathbf{R}} + (s_0 - c_0) \tilde{\mathbf{V}}_1) \right] dS \Delta \tilde{\mathbf{x}}_e, \\ \Delta_{\tilde{\mathbf{x}}} \bar{\mathbf{f}}_{\mathbf{n}}^e &= \int_{\Gamma_0^e} q \mathbf{N}_{,\alpha}^T (s_0 - c_0) \mathbf{n} (\mathbf{a}^\alpha)^T \tilde{\mathbf{V}}_2 dS \Delta \tilde{\mathbf{x}}_e, \\ \Delta_q \bar{\mathbf{f}}_{\mathbf{n}}^e &= \int_{\Gamma_0^e} \mathbf{N}_{,\alpha}^T (\tilde{\mathbf{d}} \cdot \mathbf{a}^\alpha) \mathbf{n} \hat{\mathbf{N}}_q dS \Delta \hat{q}_e,\end{aligned}\tag{127}$$

and

$$\begin{aligned}\Delta_{\mathbf{x}} \bar{\mathbf{f}}_{\tilde{\mathbf{n}}}^e &= \int_{\Gamma_0^e} q \tilde{\mathbf{N}}_{,\alpha}^T \tilde{\mathbf{n}} \left[(\tilde{\mathbf{a}}^\alpha)^T ((s_0 + c_0) \mathbf{R} + (s_0 - c_0) \mathbf{V}_1) \right] dS \Delta \mathbf{x}_e, \\ \Delta_{\tilde{\mathbf{x}}} \bar{\mathbf{f}}_{\tilde{\mathbf{n}}}^e &= \int_{\Gamma_0^e} q \tilde{\mathbf{N}}_{,\alpha}^T \tilde{\mathbf{n}} \left[\mathbf{d}^T \tilde{\mathcal{A}}^\alpha + (\mathbf{d} \cdot \tilde{\mathbf{a}}^\alpha) \tilde{\mathbf{R}} \right] dS \Delta \tilde{\mathbf{x}}_e, \\ \Delta_{\tilde{\mathbf{x}}} \bar{\mathbf{f}}_{\tilde{\mathbf{n}}}^e &= \int_{\Gamma_0^e} q \tilde{\mathbf{N}}_{,\alpha}^T (s_0 - c_0) \tilde{\mathbf{n}} (\tilde{\mathbf{a}}^\alpha)^T \mathbf{V}_2 dS \Delta \tilde{\mathbf{x}}_e, \\ \Delta_q \bar{\mathbf{f}}_{\tilde{\mathbf{n}}}^e &= \int_{\Gamma_0^e} \tilde{\mathbf{N}}_{,\alpha}^T (\mathbf{d} \cdot \tilde{\mathbf{a}}^\alpha) \tilde{\mathbf{n}} \hat{\mathbf{N}}_q dS \Delta \hat{q}_e,\end{aligned}\tag{128}$$

and based on Eqs. (111)–(112),

$$\begin{aligned}\Delta_{\mathbf{x}} \bar{\mathbf{f}}_q^e &= \int_{\Gamma_0^e} \hat{\mathbf{N}}_q^T \left[-c_0 (\tilde{\mathbf{n}} + \tilde{\boldsymbol{\nu}}) + s_0 (\tilde{\mathbf{n}} - \tilde{\boldsymbol{\nu}}) \right]^T \mathbf{R} dS \Delta \mathbf{x}_e, \\ \Delta_{\tilde{\mathbf{x}}} \bar{\mathbf{f}}_q^e &= \int_{\Gamma_0^e} \hat{\mathbf{N}}_q^T \left[-c_0 (\mathbf{n} + \boldsymbol{\nu}) + s_0 (\mathbf{n} - \boldsymbol{\nu}) \right]^T \tilde{\mathbf{R}} dS \Delta \tilde{\mathbf{x}}_e, \\ \Delta_q \bar{\mathbf{f}}_q^e &= \mathbf{0},\end{aligned}\tag{129}$$

with \mathbf{d} and $\tilde{\mathbf{d}}$ given in Eqs. (70.2)–(70.3).

B.3 Linearization for the C^1 -continuity constraint

This section reports the linearization of the force vectors that are used to enforce the C^1 -continuity constraint, see Sec. 5.2.

B.3.1 Penalty method

This section shows the linearization of the force vectors \mathbf{f}_ϕ^e and $\mathbf{f}_\tilde{\phi}^e$ given in Eq. (87). Their contributions follow from

$$\Delta_\bullet \mathbf{f}_\phi^e = \int_{\Gamma_0^e} \varepsilon_\phi \bar{\mathbf{N}}_{,\alpha}^T \Delta_\bullet \left(g_\nabla (\mathbf{a}^\alpha \cdot \boldsymbol{\nu}) \right) dS, \quad \text{and} \quad \Delta_\bullet \mathbf{f}_\tilde{\phi}^e = \int_{\Gamma_0^e} \varepsilon_\phi \tilde{\mathbf{N}}_{,\alpha}^T \Delta_\bullet \left(g_\nabla (\tilde{\mathbf{a}}^\alpha \cdot \tilde{\boldsymbol{\nu}}) \right) dS.\tag{130}$$

These are given by

$$\begin{aligned}
\Delta_\phi \mathbf{f}_\phi^e &= \int_{\Gamma_0^e} \varepsilon_\phi \bar{\mathbf{N}}_{,\alpha}^T (\mathbf{a}^\alpha \cdot \boldsymbol{\nu}) (\mathbf{a}^\beta \cdot \boldsymbol{\nu}) \bar{\mathbf{N}}_{,\beta} dS \Delta\phi_e, \\
\Delta_{\tilde{\phi}} \mathbf{f}_\phi^e &= \int_{\Gamma_0^e} \varepsilon_\phi \bar{\mathbf{N}}_{,\alpha}^T (\mathbf{a}^\alpha \cdot \boldsymbol{\nu}) (\tilde{\mathbf{a}}^\beta \cdot \tilde{\boldsymbol{\nu}}) \tilde{\mathbf{N}}_{,\beta} dS \Delta\tilde{\phi}_e, \\
\Delta_{\mathbf{x}} \mathbf{f}_\phi^e &= \int_{\Gamma_0^e} \varepsilon_\phi \bar{\mathbf{N}}_{,\alpha}^T \left[(\mathbf{a}^\alpha \cdot \boldsymbol{\nu}) \phi_{,\beta} \mathbf{W}^\beta + g_\nabla \mathbf{W}^\alpha \right] dS \Delta\mathbf{x}_e, \\
\Delta_{\tilde{\mathbf{x}}} \mathbf{f}_\phi^e &= \int_{\Gamma_0^e} \varepsilon_\phi \bar{\mathbf{N}}_{,\alpha}^T (\mathbf{a}^\alpha \cdot \boldsymbol{\nu}) \tilde{\phi}_{,\beta} \tilde{\mathbf{W}}^\beta dS \Delta\tilde{\mathbf{x}}_e, \\
\Delta_{\hat{\mathbf{x}}} \mathbf{f}_\phi^e &= \int_{\Gamma_0^e} \varepsilon_\phi \bar{\mathbf{N}}_{,\alpha}^T \left[(\mathbf{a}^\alpha \cdot \boldsymbol{\nu}) \left(\phi_{,\beta} (\mathbf{a}^\beta)^T \mathbf{V}_2 + \tilde{\phi}_{,\beta} (\tilde{\mathbf{a}}^\beta)^T \tilde{\mathbf{V}}_2 \right) + g_\nabla (\mathbf{a}^\alpha)^T \mathbf{V}_2 \right] dS \Delta\hat{\mathbf{x}}_e,
\end{aligned} \tag{131}$$

and

$$\begin{aligned}
\Delta_\phi \mathbf{f}_\phi^e &= \int_{\Gamma_0^e} \varepsilon_\phi \tilde{\mathbf{N}}_{,\alpha}^T (\tilde{\mathbf{a}}^\alpha \cdot \tilde{\boldsymbol{\nu}}) (\mathbf{a}^\beta \cdot \boldsymbol{\nu}) \bar{\mathbf{N}}_{,\beta} dS \Delta\phi_e, \\
\Delta_{\tilde{\phi}} \mathbf{f}_\phi^e &= \int_{\Gamma_0^e} \varepsilon_\phi \tilde{\mathbf{N}}_{,\alpha}^T (\tilde{\mathbf{a}}^\alpha \cdot \tilde{\boldsymbol{\nu}}) (\tilde{\mathbf{a}}^\beta \cdot \tilde{\boldsymbol{\nu}}) \tilde{\mathbf{N}}_{,\beta} dS \Delta\tilde{\phi}_e, \\
\Delta_{\mathbf{x}} \mathbf{f}_\phi^e &= \int_{\Gamma_0^e} \varepsilon_\phi \tilde{\mathbf{N}}_{,\alpha}^T (\tilde{\mathbf{a}}^\alpha \cdot \tilde{\boldsymbol{\nu}}) \phi_{,\beta} \mathbf{W}^\beta dS \Delta\mathbf{x}_e, \\
\Delta_{\tilde{\mathbf{x}}} \mathbf{f}_\phi^e &= \int_{\Gamma_0^e} \varepsilon_\phi \tilde{\mathbf{N}}_{,\alpha}^T \left[(\tilde{\mathbf{a}}^\alpha \cdot \tilde{\boldsymbol{\nu}}) \tilde{\phi}_{,\beta} \tilde{\mathbf{W}}^\beta + g_\nabla \tilde{\mathbf{W}}^\alpha \right] dS \Delta\tilde{\mathbf{x}}_e, \\
\Delta_{\hat{\mathbf{x}}} \mathbf{f}_\phi^e &= \int_{\Gamma_0^e} \varepsilon_\phi \tilde{\mathbf{N}}_{,\alpha}^T \left[(\tilde{\mathbf{a}}^\alpha \cdot \tilde{\boldsymbol{\nu}}) \left(\phi_{,\beta} (\mathbf{a}^\beta)^T \mathbf{V}_2 + \tilde{\phi}_{,\beta} (\tilde{\mathbf{a}}^\beta)^T \tilde{\mathbf{V}}_2 \right) + g_\nabla (\tilde{\mathbf{a}}^\alpha)^T \tilde{\mathbf{V}}_2 \right] dS \Delta\hat{\mathbf{x}}_e.
\end{aligned} \tag{132}$$

Note that the linearizations in Eqs. (131.3)–(131.5) and Eqs. (132.3)–(132.5) vanish for the brittle fracture model. The element tangent matrix will have the following form

$$\begin{bmatrix}
\boxed{\frac{\partial \mathbf{f}_\phi^e}{\partial \mathbf{x}_e}} & \frac{\partial \mathbf{f}_\phi^e}{\partial \tilde{\mathbf{x}}_e} & \frac{\partial \mathbf{f}_\phi^e}{\partial \hat{\mathbf{x}}_e} & \frac{\partial \mathbf{f}_\phi^e}{\partial \phi_e} & \frac{\partial \mathbf{f}_\phi^e}{\partial \tilde{\phi}_e} \\
\frac{\partial \mathbf{f}_\phi^e}{\partial \mathbf{x}_e} & \frac{\partial \mathbf{f}_\phi^e}{\partial \tilde{\mathbf{x}}_e} & \frac{\partial \mathbf{f}_\phi^e}{\partial \hat{\mathbf{x}}_e} & \frac{\partial \mathbf{f}_\phi^e}{\partial \phi_e} & \frac{\partial \mathbf{f}_\phi^e}{\partial \tilde{\phi}_e}
\end{bmatrix}. \tag{133}$$

The dot-dashed framed entries vanish for the brittle fracture model. The entries $\partial \mathbf{f}_\phi^e / \partial \tilde{\phi}_e$ and $\partial \mathbf{f}_\phi^e / \partial \phi_e$ are the transpose of each other.

B.3.2 Lagrange multiplier method

The contributions to the linearizations of the force vectors in Eq. (95) for the Lagrange multiplier method are computed from

$$\begin{aligned}
\Delta_\bullet \bar{\mathbf{f}}_\phi^e &= \int_{\Gamma_0^e} \bar{\mathbf{N}}_{,\alpha}^T \Delta_\bullet (\lambda (\mathbf{a}^\alpha \cdot \boldsymbol{\nu})) dS, \\
\Delta_\bullet \bar{\mathbf{f}}_{\tilde{\phi}}^e &= \int_{\Gamma_0^e} \tilde{\mathbf{N}}_{,\alpha}^T \Delta_\bullet (\lambda (\tilde{\mathbf{a}}^\alpha \cdot \tilde{\boldsymbol{\nu}})) dS, \\
\Delta_\bullet \bar{\mathbf{f}}_\lambda^e &= \int_{\Gamma_0^e} \hat{\mathbf{N}}_\lambda^T \Delta_\bullet g_\nabla dS.
\end{aligned} \tag{134}$$

They are given by

$$\begin{aligned}
\Delta_\phi \bar{\mathbf{f}}_\phi^e &= \mathbf{0}, & \Delta_{\tilde{\phi}} \bar{\mathbf{f}}_\phi^e &= \mathbf{0}, & \Delta_{\mathbf{x}} \bar{\mathbf{f}}_\phi^e &= \int_{\Gamma_0^e} \bar{\mathbf{N}}_{,\alpha}^T \lambda \mathbf{W}^\alpha \, dS \, \Delta \mathbf{x}_e, \\
\Delta_{\tilde{\mathbf{x}}} \bar{\mathbf{f}}_\phi^e &= \mathbf{0}, & \Delta_{\hat{\mathbf{x}}} \bar{\mathbf{f}}_\phi^e &= \int_{\Gamma_0^e} \bar{\mathbf{N}}_{,\alpha}^T \lambda (\mathbf{a}^\alpha)^T \mathbf{V}_2 \, dS \, \Delta \hat{\mathbf{x}}_e, \\
\Delta_\lambda \bar{\mathbf{f}}_\phi^e &= \int_{\Gamma_0^e} \bar{\mathbf{N}}_{,\alpha}^T (\mathbf{a}^\alpha \cdot \boldsymbol{\nu}) \hat{\mathbf{N}}_\lambda \, dS \, \Delta \hat{\lambda}_e
\end{aligned} \tag{135}$$

and

$$\begin{aligned}
\Delta_\phi \bar{\mathbf{f}}_\phi^e &= \mathbf{0}, & \Delta_{\tilde{\phi}} \bar{\mathbf{f}}_\phi^e &= \mathbf{0}, & \Delta_{\mathbf{x}} \bar{\mathbf{f}}_\phi^e &= \mathbf{0}, \\
\Delta_{\tilde{\mathbf{x}}} \bar{\mathbf{f}}_\phi^e &= \int_{\Gamma_0^e} \tilde{\mathbf{N}}_{,\alpha}^T \lambda \tilde{\mathbf{W}}^\alpha \, dS \, \Delta \tilde{\mathbf{x}}_e, & \Delta_{\hat{\mathbf{x}}} \bar{\mathbf{f}}_\phi^e &= \int_{\Gamma_0^e} \tilde{\mathbf{N}}_{,\alpha}^T \lambda (\tilde{\mathbf{a}}^\alpha)^T \tilde{\mathbf{V}}_2 \, dS \, \Delta \hat{\mathbf{x}}_e, \\
\Delta_\lambda \bar{\mathbf{f}}_\phi^e &= \int_{\Gamma_0^e} \tilde{\mathbf{N}}_{,\alpha}^T (\tilde{\mathbf{a}}^\alpha \cdot \tilde{\boldsymbol{\nu}}) \hat{\mathbf{N}}_\lambda \, dS \, \Delta \hat{\lambda}_e,
\end{aligned} \tag{136}$$

and

$$\begin{aligned}
\Delta_\phi \bar{\mathbf{f}}_\lambda^e &= \int_{\Gamma_0^e} \hat{\mathbf{N}}_\lambda^T (\mathbf{a}^\alpha \cdot \boldsymbol{\nu}) \bar{\mathbf{N}}_{,\alpha} \, dS \, \Delta \phi_e, \\
\Delta_{\tilde{\phi}} \bar{\mathbf{f}}_\lambda^e &= \int_{\Gamma_0^e} \hat{\mathbf{N}}_\lambda^T (\tilde{\mathbf{a}}^\alpha \cdot \tilde{\boldsymbol{\nu}}) \tilde{\mathbf{N}}_{,\alpha} \, dS \, \Delta \tilde{\phi}_e, \\
\Delta_{\mathbf{x}} \bar{\mathbf{f}}_\lambda^e &= \int_{\Gamma_0^e} \hat{\mathbf{N}}_\lambda^T \phi_{,\alpha} \mathbf{W}^\alpha \, dS \, \Delta \mathbf{x}_e, \\
\Delta_{\tilde{\mathbf{x}}} \bar{\mathbf{f}}_\lambda^e &= \int_{\Gamma_0^e} \hat{\mathbf{N}}_\lambda^T \tilde{\phi}_{,\alpha} \tilde{\mathbf{W}}^\alpha \, dS \, \Delta \tilde{\mathbf{x}}_e, \\
\Delta_{\hat{\mathbf{x}}} \bar{\mathbf{f}}_\lambda^e &= \int_{\Gamma_0^e} \hat{\mathbf{N}}_\lambda^T \left[\phi_{,\alpha} (\mathbf{a}^\alpha)^T \mathbf{V}_2 + \tilde{\phi}_{,\alpha} (\tilde{\mathbf{a}}^\alpha)^T \tilde{\mathbf{V}}_2 \right] \, dS \, \Delta \hat{\mathbf{x}}_e, \\
\Delta_\lambda \bar{\mathbf{f}}_\lambda^e &= \mathbf{0}.
\end{aligned} \tag{137}$$

Note that the linearizations in Eqs. (135.3)–(135.5), Eqs. (136.3)–(136.5) and Eqs. (137.3)–(137.5) vanish for the brittle fracture model. The full element tangent matrix has the following form

$$\left[\begin{array}{ccc|cc|c}
\boxed{\frac{\partial \bar{\mathbf{f}}_\phi^e}{\partial \mathbf{x}_e}} & \mathbf{0} & \boxed{\frac{\partial \bar{\mathbf{f}}_\phi^e}{\partial \hat{\mathbf{x}}_e}} & \mathbf{0} & \mathbf{0} & \boxed{\frac{\partial \bar{\mathbf{f}}_\phi^e}{\partial \lambda_e}} \\
\mathbf{0} & \boxed{\frac{\partial \bar{\mathbf{f}}_\phi^e}{\partial \tilde{\mathbf{x}}_e}} & \boxed{\frac{\partial \bar{\mathbf{f}}_\phi^e}{\partial \hat{\mathbf{x}}_e}} & \mathbf{0} & \mathbf{0} & \boxed{\frac{\partial \bar{\mathbf{f}}_\phi^e}{\partial \lambda_e}} \\
\boxed{\frac{\partial \bar{\mathbf{f}}_\lambda^e}{\partial \mathbf{x}_e}} & \boxed{\frac{\partial \bar{\mathbf{f}}_\lambda^e}{\partial \tilde{\mathbf{x}}_e}} & \boxed{\frac{\partial \bar{\mathbf{f}}_\lambda^e}{\partial \hat{\mathbf{x}}_e}} & \boxed{\frac{\partial \bar{\mathbf{f}}_\lambda^e}{\partial \phi_e}} & \boxed{\frac{\partial \bar{\mathbf{f}}_\lambda^e}{\partial \tilde{\phi}_e}} & \mathbf{0}
\end{array} \right] \tag{138}$$

Note that one solid framed block is the transpose of the other solid framed block, while the dot-dashed framed entries vanish for the fracture model.

C Comparison of the six-patch and unstructured spline discretization of a sphere

The following error is defined in order to assess the accuracy of the six-patch and unstructured spline discretizations of a sphere,

$$\epsilon_{L^2} := \frac{1}{R^2} \sqrt{\int_{S_0} \left\| \|\mathbf{X} - \mathbf{X}_0\|_2 - R \right\|_2^2 dS}. \quad (139)$$

Here, R is the radius and \mathbf{X}_0 is the sphere's origin. Fig. 29 shows the L^2 -error, defined in Eq. (139), over the mesh refinement. The error decays for both approaches as the number of control points is increased. The absolute error of the six-patch discretization is more than one order of magnitude smaller compared to the unstructured spline discretization. However, the six-patch sphere is only C^0 -continuous at patch interfaces.

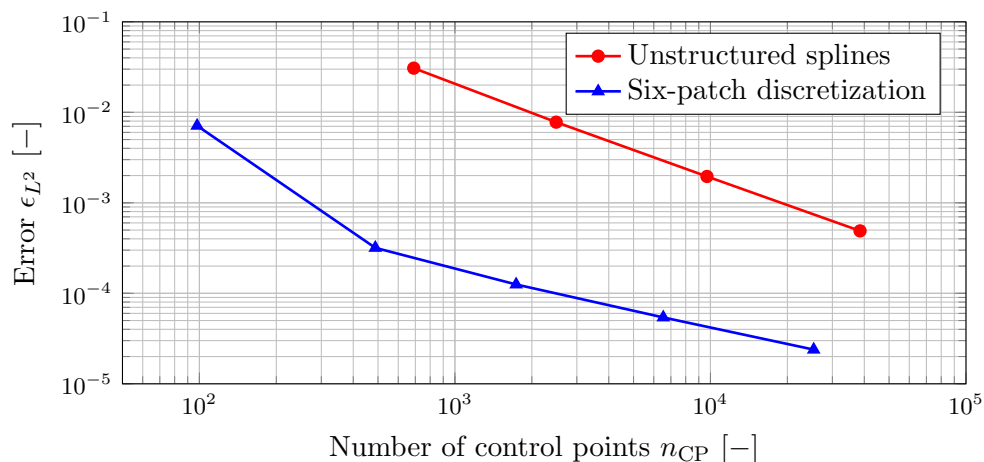


Figure 29: Construction of the spherical six-patch discretization: Comparison of the L^2 -error, defined in Eq. (139), between the six-patch and unstructured spline discretization over the mesh refinement.

References

- Amor, H., Marigo, J.-J., and Maurini, C. (2009). Regularized formulation of the variational brittle fracture with unilateral contact: Numerical experiments. *Journal of the Mechanics and Physics of Solids*, **57**(8):1209–1229.
- Apostolatos, A., Bletzinger, K.-U., and Wüchner, R. (2019). Weak imposition of constraints for structural membranes in transient geometrically nonlinear isogeometric analysis on multipatch surfaces. *Computer Methods in Applied Mechanics and Engineering*, **350**:938–994.
- Apostolatos, A., Schmidt, R., Wüchner, R., and Bletzinger, K.-U. (2014). A Nitsche-type formulation and comparison of the most common domain decomposition methods in isogeometric analysis. *International Journal for Numerical Methods in Engineering*, **97**(7):473–504.
- Bauer, A., Wüchner, R., and Bletzinger, K.-U. (2020). Weak coupling of nonlinear isogeometric spatial Bernoulli beams. *Computer Methods in Applied Mechanics and Engineering*, **361**:112747.

- Beirão da Veiga, L., Buffa, A., Cho, D., and Sangalli, G. (2011). IsoGeometric analysis using T-splines on two-patch geometries. *Computer Methods in Applied Mechanics and Engineering*, **200**(21):1787–1803.
- Belytschko, T., Stolarski, H., Liu, W. K., Carpenter, N., and Ong, J. S. (1985). Stress projection for membrane and shear locking in shell finite elements. *Computer Methods in Applied Mechanics and Engineering*, **51**(1):221–258.
- Borden, M. J., Hughes, T. J. R., Landis, C. M., Anvari, A., and Lee, I. J. (2016). A phase-field formulation for fracture in ductile materials: Finite deformation balance law derivation, plastic degradation, and stress triaxiality effects. *Computer Methods in Applied Mechanics and Engineering*, **312**:130–166.
- Borden, M. J., Hughes, T. J. R., Landis, C. M., and Verhoosel, C. V. (2014). A higher-order phase-field model for brittle fracture: Formulation and analysis within the isogeometric analysis framework. *Computer Methods in Applied Mechanics and Engineering*, **273**:100–118.
- Bouclier, R. and Passieux, J.-C. (2018). A Nitsche-based non-intrusive coupling strategy for global/local isogeometric structural analysis. *Computer Methods in Applied Mechanics and Engineering*, **340**:253–277.
- Bouclier, R., Passieux, J.-C., and Salaün, M. (2016). Local enrichment of NURBS patches using a non-intrusive coupling strategy: Geometric details, local refinement, inclusion, fracture. *Computer Methods in Applied Mechanics and Engineering*, **300**:1–26.
- Bouclier, R., Passieux, J.-C., and Salaün, M. (2017). Development of a new, more regular, mortar method for the coupling of NURBS subdomains within a NURBS patch: Application to a non-intrusive local enrichment of NURBS patches. *Computer Methods in Applied Mechanics and Engineering*, **316**:123–150.
- Bourdin, B., Francfort, G., and Marigo, J.-J. (2000). Numerical experiments in revisited brittle fracture. *Journal of the Mechanics and Physics of Solids*, **48**(4):797–826.
- Bracco, C., Giannelli, C., Kapl, M., and Vázquez, R. (2019). Isogeometric analysis with C1 hierarchical functions on planar two-patch geometries. arXiv:1901.09689.
- Brivadis, E., Buffa, A., Wohlmuth, B., and Wunderlich, L. (2015). Isogeometric mortar methods. *Computer Methods in Applied Mechanics and Engineering*, **284**:292–319.
- Cahn, J. W. (1961). On spinodal decomposition. *Acta Metallurgica*, **9**(9):795–801.
- Cahn, J. W. and Hilliard, J. E. (1958). Free Energy of a Nonuniform System. I. Interfacial Free Energy. *The Journal of Chemical Physics*, **28**(2):258–267.
- Chan, C. L., Anitescu, C., and Rabczuk, T. (2018). Isogeometric analysis with strong multipatch C1-coupling. *Computer Aided Geometric Design*, **62**:294–310.
- Chan, C. L., Anitescu, C., and Rabczuk, T. (2019). Strong multipatch C1-coupling for isogeometric analysis on 2d and 3d domains. *Computer Methods in Applied Mechanics and Engineering*, **357**:112599.
- Chung, J. and Hulbert, G. M. (1993). A time integration algorithm for structural dynamics with improved numerical dissipation: The generalized-alpha method. *Journal of Applied Mechanics*, **60**(2):371–375.
- Ciarlet, P. G. (1993). *Mathematical Elasticity: Three Dimensional Elasticity*. North-Holland.

- Collin, A., Sangalli, G., and Takacs, T. (2016). Analysis-suitable G1 multi-patch parametrizations for C1 isogeometric spaces. *Computer Aided Geometric Design*, **47**:93–113.
- Coox, L., Greco, F., Atak, O., Vandepitte, D., and Desmet, W. (2017a). A robust patch coupling method for NURBS-based isogeometric analysis of non-conforming multipatch surfaces. *Computer Methods in Applied Mechanics and Engineering*, **316**:235–260.
- Coox, L., Maurin, F., Greco, F., Deckers, E., Vandepitte, D., and Desmet, W. (2017b). A flexible approach for coupling NURBS patches in rotationless isogeometric analysis of Kirchhoff–Love shells. *Computer Methods in Applied Mechanics and Engineering*, **325**:505–531.
- Dedoncker, S., Coox, L., Maurin, F., Greco, F., and Desmet, W. (2018). Bézier tilings of the sphere and their applications in benchmarking multipatch isogeometric methods. *Computer Methods in Applied Mechanics and Engineering*, **332**:255–279.
- Dittmann, M., Schuß, S., Wohlmuth, B., and Hesch, C. (2019). Weak Cn coupling for multipatch isogeometric analysis in solid mechanics. *International Journal for Numerical Methods in Engineering*, **118**(11):678–699.
- Dittmann, M., Schuß, S., Wohlmuth, B., and Hesch, C. (2020). Crosspoint modification for multi-patch isogeometric analysis. *Computer Methods in Applied Mechanics and Engineering*, **360**:112768.
- Dokken, T., Lyche, T., and Pettersen, K. F. (2013). Polynomial splines over locally refined box-partitions. *Computer Aided Geometric Design*, **30**(3):331–356.
- Dornisch, W. and Klinkel, S. (2011). Boundary conditions and multi-patch connections in isogeometric analysis. *PAMM*, **11**(1):207–208.
- Dornisch, W., Stöckler, J., and Müller, R. (2017). Dual and approximate dual basis functions for B-splines and NURBS – Comparison and application for an efficient coupling of patches with the isogeometric mortar method. *Computer Methods in Applied Mechanics and Engineering*, **316**:449–496.
- Dornisch, W., Vitucci, G., and Klinkel, S. (2015). The weak substitution method – an application of the mortar method for patch coupling in NURBS-based isogeometric analysis. *International Journal for Numerical Methods in Engineering*, **103**(3):205–234.
- Du, X., Zhao, G., and Wang, W. (2015). Nitsche method for isogeometric analysis of Reissner–Mindlin plate with non-conforming multi-patches. *Computer Aided Geometric Design*, **35–36**:121–136.
- Du, X., Zhao, G., Wang, W., and Fang, H. (2019). Nitsche’s method for non-conforming multipatch coupling in hyperelastic isogeometric analysis. *Computational Mechanics*.
- Duong, T. X., Roohbakhshan, F., and Sauer, R. A. (2017). A new rotation-free isogeometric thin shell formulation and a corresponding continuity constraint for patch boundaries. *Computer Methods in Applied Mechanics and Engineering*, **316**:43–83.
- Ebner, M., Marone, F., Stampanoni, M., and Wood, V. (2013). Visualization and quantification of electrochemical and mechanical degradation in li ion batteries. *Science*, **342**(6159):716–720.
- Elson, E. L., Fried, E., Dolbow, J. E., and Genin, G. M. (2010). Phase separation in biological membranes: Integration of theory and experiment. *Annual Review of Biophysics*, **39**(1):207–226.

- Francfort, G. and Marigo, J.-J. (1998). Revisiting brittle fracture as an energy minimization problem. *Journal of the Mechanics and Physics of Solids*, **46**(8):1319–1342.
- Gerasimov, T. and Lorenzis, L. D. (2019). On penalization in variational phase-field models of brittle fracture. *Computer Methods in Applied Mechanics and Engineering*, **354**:990–1026.
- Goyal, A. and Simeon, B. (2017). On penalty-free formulations for multipatch isogeometric Kirchhoff–Love shells. *Mathematics and Computers in Simulation*, **136**:78–103.
- Griffith, A. A. (1921). VI. The Phenomena of Rupture and Flow in Solids. *Philosophical Transactions of the Royal Society of London Series A*, **221**:163–198.
- Gu, J., Yu, T., Lich, L. V., Nguyen, T.-T., and Bui, T. Q. (2018). Adaptive multi-patch isogeometric analysis based on locally refined B-splines. *Computer Methods in Applied Mechanics and Engineering*, **339**:704–738.
- Guo, Y. and Ruess, M. (2015). Nitsche’s method for a coupling of isogeometric thin shells and blended shell structures. *Computer Methods in Applied Mechanics and Engineering*, **284**:881–905.
- Herrema, A. J., Johnson, E. L., Proserpio, D., Wu, M. C., Kiendl, J., and Hsu, M.-C. (2019). Penalty coupling of non-matching isogeometric Kirchhoff–Love shell patches with application to composite wind turbine blades. *Computer Methods in Applied Mechanics and Engineering*, **346**:810–840.
- Hesch, C. and Betsch, P. (2012). Isogeometric analysis and domain decomposition methods. *Computer Methods in Applied Mechanics and Engineering*, **213–216**:104–112.
- Hirschler, T., Bouclier, R., Dureisseix, D., Duval, A., Elguedj, T., and Morlier, J. (2019a). A dual domain decomposition algorithm for the analysis of non-conforming isogeometric kirchhoff–love shells. *Computer Methods in Applied Mechanics and Engineering*, **357**:112578.
- Hirschler, T., Bouclier, R., Duval, A., Elguedj, T., and Morlier, J. (2019b). The embedded isogeometric Kirchhoff–Love shell: From design to shape optimization of non-conforming stiffened multipatch structures. *Computer Methods in Applied Mechanics and Engineering*, **349**:774–797.
- Horger, T., Reali, A., Wohlmuth, B., and Wunderlich, L. (2019). A hybrid isogeometric approach on multi-patches with applications to Kirchhoff plates and eigenvalue problems. *Computer Methods in Applied Mechanics and Engineering*, **348**:396–408.
- Hu, Q., Chouly, F., Hu, P., Cheng, G., and Bordas, S. P. (2018). Skew-symmetric Nitsche’s formulation in isogeometric analysis: Dirichlet and symmetry conditions, patch coupling and frictionless contact. *Computer Methods in Applied Mechanics and Engineering*, **341**:188–220.
- Hughes, T. J. R., Cottrell, J. A., and Bazilevs, Y. (2005). Isogeometric analysis: CAD, finite elements, NURBS, exact geometry and mesh refinement. *Computer Methods in Applied Mechanics and Engineering*, **194**(39–41):4135–4195.
- Kapl, M., Sangalli, G., and Takacs, T. (2017). Dimension and basis construction for analysis-suitable G1 two-patch parameterizations. *Computer Aided Geometric Design*, **52–53**:75–89. Geometric Modeling and Processing 2017.
- Kapl, M. and Vitrih, V. (2020). Isogeometric collocation on planar multi-patch domains. *Computer Methods in Applied Mechanics and Engineering*, **360**:112684.

- Kapl, M., Vitrih, V., Jüttler, B., and Birner, K. (2015). Isogeometric analysis with geometrically continuous functions on two-patch geometries. *Computers & Mathematics with Applications*, **70**(7):1518–1538.
- Kiendl, J., Bazilevs, Y., Hsu, M.-C., Wüchner, R., and Bletzinger, K.-U. (2010). The bending strip method for isogeometric analysis of Kirchhoff-Love shell structures comprised of multiple patches. *Computer Methods in Applied Mechanics and Engineering*, **199**:2403–2416.
- Kiendl, J., Bletzinger, K.-U., Linhard, J., and Wüchner, R. (2009). Isogeometric shell analysis with Kirchhoff-Love elements. *Computer Methods in Applied Mechanics and Engineering*, **198**:3902–3914.
- Lei, Z., Gillot, F., and Jezequel, L. (2015). A C0/G1 multiple patches connection method in isogeometric analysis. *Applied Mathematical Modelling*, **39**(15):4405–4420.
- Leidinger, L., Breitenberger, M., Bauer, A., Hartmann, S., Wüchner, R., Bletzinger, K.-U., Duddeck, F., and Song, L. (2019). Explicit dynamic isogeometric B-Rep analysis of penalty-coupled trimmed NURBS shells. *Computer Methods in Applied Mechanics and Engineering*, **351**:891–927.
- Liu, Z., Cheng, J., Yang, M., Yuan, P., Qiu, C., Gao, W., and Tan, J. (2019). Isogeometric analysis of large thin shell structures based on weak coupling of substructures with unstructured T-splines patches. *Advances in Engineering Software*, **135**:102692.
- Mi, Y. and Zheng, H. (2018). An interpolation method for coupling non-conforming patches in isogeometric analysis of vibro-acoustic systems. *Computer Methods in Applied Mechanics and Engineering*, **341**:551–570.
- Nguyen, V. P., Kerfriden, P., Brino, M., Bordas, S. P. A., and Bonisoli, E. (2014). Nitsche’s method for two and three dimensional NURBS patch coupling. *Computational Mechanics*, **53**(6):1163–1182.
- Nguyen-Thanh, N., Zhou, K., Zhuang, X., Areias, P., Nguyen-Xuan, H., Bazilevs, Y., and Rabczuk, T. (2017). Isogeometric analysis of large-deformation thin shells using RHT-splines for multiple-patch coupling. *Computer Methods in Applied Mechanics and Engineering*, **316**:1157–1178.
- Paul, K., Zimmermann, C., Mandadapu, K. K., Hughes, T. J. R., Landis, C. M., and Sauer, R. A. (2020). An adaptive space-time phase field formulation for dynamic fracture of brittle shells based on LR NURBS. *Computational Mechanics*, **65**:1039–1062.
- Ruess, M., Schillinger, D., Özcan, A. I., and Rank, E. (2014). Weak coupling for isogeometric analysis of non-matching and trimmed multi-patch geometries. *Computer Methods in Applied Mechanics and Engineering*, **269**:46–71.
- Sahu, A., Sauer, R. A., and Mandadapu, K. K. (2017). Irreversible thermodynamics of curved lipid membranes. *Physical Review E*, **96**:042409.
- Sauer, R. A. (2014). Stabilized finite element formulations for liquid membranes and their application to droplet contact. *International Journal for Numerical Methods in Fluids*, **75**(7):519–545.
- Sauer, R. A. (2018). On the computational modeling of lipid bilayers using thin-shell theory. In Steigmann, D. J., editor, *The Role of Mechanics in the Study of Lipid Bilayers*, pages 221–286. Springer International Publishing, Cham.

- Sauer, R. A. and Duong, T. X. (2017). On the theoretical foundations of thin solid and liquid shells. *Mathematics and Mechanics of Solids*, **22**(3):343–371.
- Sauer, R. A., Duong, T. X., Mandadapu, K. K., and Steigmann, D. J. (2017). A stabilized finite element formulation for liquid shells and its application to lipid bilayers. *Journal of Computational Physics*, **330**:436–466.
- Sauer, R. A., Ghaffari, R., and Gupta, A. (2019). The multiplicative deformation split for shells with application to growth, chemical swelling, thermoelasticity, viscoelasticity and elastoplasticity. *International Journal of Solids and Structures*, **174-175**:53–68.
- Schuß, S., Dittmann, M., Wohlmuth, B., Klinkel, S., and Hesch, C. (2019). Multi-patch isogeometric analysis for Kirchhoff-Love shell elements. *Computer Methods in Applied Mechanics and Engineering*, **349**.
- Seitz, A., Farah, P., Kremheller, J., Wohlmuth, B. I., Wall, W. A., and Popp, A. (2016). Isogeometric dual mortar methods for computational contact mechanics. *Computer Methods in Applied Mechanics and Engineering*, **301**:259–280.
- Simo, J. and Fox, D. (1989). On a stress resultant geometrically exact shell model. Part I: Formulation and optimal parametrization. *Computer Methods in Applied Mechanics and Engineering*, **72**(3):267–304.
- Simo, J., Fox, D., and Rifai, M. (1990). On a stress resultant geometrically exact shell model. Part III: Computational aspects of the nonlinear theory. *Computer Methods in Applied Mechanics and Engineering*, **79**(1):21–70.
- Sommerwerk, K., Woitdt, M., Haupt, M. C., and Horst, P. (2017). Reissner–Mindlin shell implementation and energy conserving isogeometric multi-patch coupling. *International Journal for Numerical Methods in Engineering*, **109**(7):982–1012.
- Tang, M., Carter, W. C., and Chiang, Y.-M. (2010). Electrochemically driven phase transitions in insertion electrodes for lithium-ion batteries: Examples in lithium metal phosphate olivines. *Annual Review of Materials Research*, **40**(1):501–529.
- Toshniwal, D., Speleers, H., and Hughes, T. J. (2017). Smooth cubic spline spaces on unstructured quadrilateral meshes with particular emphasis on extraordinary points: Geometric design and isogeometric analysis considerations. *Computer Methods in Applied Mechanics and Engineering*, **327**:411–458.
- Wohlmuth, B. I. (2000). A mortar finite element method using dual spaces for the Lagrange multiplier. *SIAM Journal on Numerical Analysis*, **38**(3):989–1012.
- Wunderlich, L., Seitz, A., Alaydin, M. D., Wohlmuth, B., and Popp, A. (2019). Biorthogonal splines for optimal weak patch-coupling in isogeometric analysis with applications to finite deformation elasticity. *Computer Methods in Applied Mechanics and Engineering*, **346**:197–215.
- Yin, S., Yu, T., Bui, T. Q., Zheng, X., and Gu, S. (2019). Static and dynamic fracture analysis in elastic solids using a multiscale extended isogeometric analysis. *Engineering Fracture Mechanics*, **207**:109–130.
- Zhao, G., Du, X., Wang, W., Liu, B., and Fang, H. (2017). Application of isogeometric method to free vibration of Reissner–Mindlin plates with non-conforming multi-patch. *Computer-Aided Design*, **82**:127–139.

- Zimmermann, C. and Sauer, R. A. (2017). Adaptive local surface refinement based on LR NURBS and its application to contact. *Computational Mechanics*, **60**:1011–1031.
- Zimmermann, C., Toshniwal, D., Landis, C. M., Hughes, T. J. R., Mandadapu, K. K., and Sauer, R. A. (2019). An isogeometric finite element formulation for phase transitions on deforming surfaces. *Computer Methods in Applied Mechanics and Engineering*, **351**:441–477.
- Zou, Z., Scott, M., Borden, M., Thomas, D., Dornisch, W., and Brivadis, E. (2018). Isogeometric Bézier dual mortaring: Refineable higher-order spline dual bases and weakly continuous geometry. *Computer Methods in Applied Mechanics and Engineering*, **333**:497–534.